

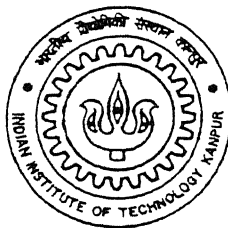
**FINITE ELEMENT ANALYSIS
OF
ELECTRO-DISCHARGE DIAMOND GRINDING (EDDG)**

*A Thesis Submitted
In Partial Fulfillment of the Requirement
For the Degree of*

DOCTOR OF PHILOSOPHY

by

VINOD YADAVA



to the

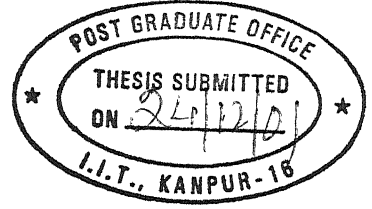
**DEPARTMENT OF MECHANICAL ENGINEERING
INDIAN INSTITUTE OF TECHNOLOGY- KANPUR**

December, 2001

23 SEP 2003 / ME
भारतीय
भारती
पत्रिका क्र० A.145041



A145041



CERTIFICATE

It is certified that the thesis work entitled *Finite Element Analysis of Electro-Discharge Diamond Grinding* by Vinod Yadava has been carried out under our supervision, and that it has not been submitted elsewhere for a degree.

(Prof. V.K.Jain)

(Prof. P.M.Dixit)

Department of Mechanical Engineering
Indian Institute of Technology
Kanpur-208 016 India

December, 2001

Acknowledgements

I take this opportunity to express my deepest gratitude and heartfelt thanks to my thesis supervisors Prof. V.K.Jain and Prof. P.M.Dixit for their expert guidance, constant encouragement, constructive criticism and inspiring advice throughout this course of research. My interactions with them academic or otherwise have always been fruitful and pleasant. I am particularly thankful to Prof. M.K.Muju who has taught me the subjects of my area of interest in depth and with research orientation. A word of thanks also to Prof. G.K.Lal, Prof. S.K.Choudhary, Prof. P.C.Pandey, and Dr N.V.Reddy for their encouragement during the various phases of my research work.

I am obliged to Motilal Nehru Regional Engineering College Allahabad for sponsoring me as QIP scholar. I also thank to Ministry of Human Resource Development, Government of India for its financial support in terms of hike in scholarship and contingency grant. I also acknowledge the financial support from Council of Scientific and Industrial Research (CSIR), New Delhi for the project “ Abrasive electro-discharge grinding of advanced engineering materials.”

I express my appreciation to Jilani Sahib, Neelesh, Bilgi, D.K.Singh, Jayswal, Gorana, Sunil, Ram Kumar, Rakesh Mote, and Shaifali for their valuable suggestions and fruitful discussions.

My sincere thanks are due to Sri R.M.Jha, Sri H.P.Sharma, Sri Phool Chand, Mr Anil, and Mr Rakesh of the manufacturing science laboratory for their friendly and practical suggestions during discussions. I thank Ms Anupma and Ms Lalita for their uncanny ability to make clear drawings and proper suggestions for attractive text styles.

The time I spent with all my friends residing in SBRA namely Pranveer, Mukul, Ramesh, Pramod, Manaklal, Vinay, Mangal, B.N.Singh, S.P.Singh, Sanjay Kumar, S.P Shukla, Gireesh, Patidar, Dharmendra, R.K.jain, Shiva, Tariq, and Sanat ji have been very exciting and friendly as well. They really made life at IIT Kanpur enjoyable, memorable and worthwhile.

I feel deeply for being remained excused by my wife Anuradha and my invaluable lovely daughter Vimbika and lovely sons Anurag and Vidipt, who have missed my attention during innumerable occasions due to my busy schedules. The research plan could not have been a dream without the loving support and encouragement and tolerance of my wife.

My deepest regards and greatest admiration remain to my father Sri Ram Awadh Yadav, Retd. Teacher, Govt. of UP, who has taught me how to walk on an untrodden path in the quest of knowledge to fight for the technological development for the benefit of mankind. He has had a significant role in molding my career and inspiration for higher studies.

Finally, I wish to acknowledge to all those who helped me directly or indirectly for successful completion of this research work.



Vinod Yadava

**Dedicated to
My father
Sri Ram Awadh Yadav**

A **THEORY** is something, which **NOBODY** believes except the person Proposing the theory

An **EXPERIMENT** is something, which **EVERYBODY** believes except the Person performing the experiment

Albert Einstein

After hundred years of research in machining, why does industry still rely on hundred years old models to make predictions of what will be seen on the shop floor?

*Rich Furness
Ford Motor Company*

SYNOPSIS

Name of the student: Vinod Yadava

Roll No. 9810576

Degree for which submitted: Ph.D.

Department: Mechanical Engineering

Thesis Title: Finite Element Analysis of Electro-Discharge Diamond Grinding

Name(s) of thesis supervisors:

(1) Prof. V.K.Jain

(2) Prof. P.M.Dixit

Month and Year of thesis submission: December 2001

Emergence of *advanced engineering materials*, having remarkable technological characteristics in terms of high strength temperature resistance (HSTR), high hardness, high wear resistance, high toughness etc., plays an important role in modern manufacturing industries, especially, in aircraft, automobile, tool and die, medical and electronic. Shaping of these materials with stringent design requirements such as high precision, complex shapes and high surface quality is inevitable to put them in use. To achieve these objectives through traditional machining techniques, cutting tools with super qualities are needed, which are yet to be developed. Therefore, to exploit these difficult-to-machine advanced engineering materials with new challenges, it was perceived to develop novel advanced machining processes (AMPs).

Advanced machining techniques have been classified into four basic category i.e. mechanical (abrasive/water jet machining (A/WJM), abrasive flow machining (AFM), magnetic abrasive finishing (MAF) etc.), thermal (Electrical discharge machining (EDM), laser beam machining (LBM), electron beam machining (EBM) etc.), chemical machining (CHM) and electro-chemical machining (ECM) processes. Amongst these, EDM is perhaps the most widely used AMP in the present day industries. EDM is a thermal process where material is removed by utilizing high-density thermal energy. This leaves a recast layer with micro-cracks on the machined surface. This continues to be the major concern if high surface integrity of the machined component is required.

Technological improvement of advanced machining processes can be achieved by combining two or more ~~than~~ two different physico-chemical actions on the material being processed. The machining ~~process~~ so developed is called *hybrid-machining process* (HMP). These processes are developed to exploit the potential advantages and to restrict the disadvantages associated with an individual constituent process. In particular a

mechanical action, which is used in conventional material removal processes, can be combined with unconventional machining action such as mechanical, thermal or electro-chemical. Electrical discharge diamond grinding (EDDG), which integrates diamond grinding and electro-discharge machining (EDM), is a new hybrid machining process for shaping electrically conductive very hard materials. In this process, the workpiece is simultaneously subjected to heating by electrical sparks and abrasion by diamond abrasive grains. The sparking takes place in the gap between the workpiece and metallic bonding material of the wheel. The improved grinding performance in EDDG is due to continuous in-process dressing and declogging of the wheel. In addition to this, spark discharges thermally soften the work material in the grinding zone and thus, diminish the grinding forces. Experimental results available in the published literature, concerning EDDG of electrically conducting cemented carbide, titanium alloy, and metal matrix composites, are technologically appealing.

Published literature available on EDDG hybrid machining process is scarce. However, the available literature reveals that the feasibility of EDDG has been experimentally tested in cut-off and cut-off grinding configurations. The EDDG process can also be used in surface grinding mode with suitable design of fixture and feed control device. Although the investigations carried out by various researchers are valuable, but they seem to be rather lacking in theoretical treatment of the EDDG process.

EDDG is a *complex machining process* where several disciplines of science and engineering are involved in its theory. It is not possible to present a simple and comprehensive theory, which explains the nature of the process with every detail. Analysis of EDDG process consists of analysis of each constituent process namely EDM and grinding. The work reported in this thesis makes an attempt in this direction. It comprises analysis of *temperature distribution* in the workpiece for each constituent process and also for combined process. Thermal residual stresses, which are induced due to steep temperature gradients in the workpiece, are the best indicators of thermal influence on the surface integrity. Keeping this in view, *thermal stresses* during cut-off grinding and EDM have been analyzed. The findings of this thesis will be helpful in developing a comprehensive surface integrity model for EDDG.

Though simple idealized problems have exact solution, the real engineering problems like the one presented in this thesis are, in general, too complex to permit an exact solution. In such real problems '*numerical approximation*' is the only recourse to make quantitative predictions. At present several numerical methods are available, namely, finite difference method (FDM), finite element method (FEM), finite volume method (FVM), spectral method, boundary element method (BEM) etc for solving different types of problems. Each of these techniques has its own potential and weaknesses. FEM is a versatile method that can solve a wide range of different engineering problems of complex geometry, materials, loading and boundary conditions. In view of these flexibilities, Galerkin finite element method has been employed for solving the present problem, and codes for temperature distribution and thermal stresses in the workpiece have been developed.

In the development of *thermal model for EDDG*, care has been taken to make sure that EDM is compatible with grinding. Adjustable parameters of EDDG process are wheel feed rates and spark discharge parameters such as pulse on-time, duty factor, mean current and working voltage. Currently available thermal models of conventional grinding process while using conventional wheels (usually, electrically non-conducting) cannot be extended to grinding with diamond wheels, since behaviour of these two types of wheels is entirely different. With this in view, a thermal model of diamond cut-off grinding is presented to calculate temperature distribution in the workpiece. The model has been validated by theoretical /experimental data available in the literature.

In grinding operation almost all *grinding energy* is converted into heat within a small grinding zone. A large part of this heat flows into the workpiece, which results in elevated temperature and thermal damage to the workpiece. Keeping this in view, a thermal model has been developed for cut-off grinding in terms of heat conduction equation with specified boundary conditions. Transient temperature (primary variable) distribution in the workpiece is obtained by using FEM and FDM for marching in time. The depthwise variation of temperature has been compared with the results available in the literature for cut-off operation. Effect of feed on temperature distribution has also been studied.

Thermal analysis of EDM process has also been done by using transient heat conduction equation. Axisymmetric domain with relevant boundary conditions has been considered for analysis. In thermal modeling of EDM, spark on-/off-time, spark radius, heat flux profile and energy partition of discharge power are considered as the main parameters. The latent heat required for phase change is accounted for by modifying the expression for the specific heat of workpiece. Gaussian heat distribution within a spark has been assumed.

Temperature distribution in the workpiece due to EDDG has been computed by *superposition* of the two temperature distributions due to grinding and EDM. In determining the combined total temperature, proper compatibility between EDM and grinding has been maintained. It has been assumed that only one spark takes place at a time and next spark at the same location is repeated after sparking at all other assumed spark locations is over. The grinding time required to move down the grinding wheel by exactly one element has been completely matched with total time required for all sparks to take place. Results showing the effect of grinding as well as EDM parameters on temperature distribution have also been reported.

Heat generated due to grinding and EDM both will introduce *thermal stresses* in the workpiece. If these stresses are lower than the material yield stress, no thermal residual stresses will be introduced. Hence, an attempt has been made to find thermal stresses due to cut-off grinding as well as EDM. The transient temperature distribution obtained by FEM is used to analyze thermal stresses in the workpiece. Plane strain condition is assumed for thermal stress analysis of cut-off grinding. Thermal stresses so obtained are below the yield strength of the workpiece material. Thermal stresses due to single spark have been modeled as axisymmetric problem. The zones, where thermal stresses are beyond yield strength are also investigated. The effects of EDM process parameters on thermal stresses have also been reported.

In EDDG, it is expedient to finish-grind flat components in surface grinding mode with the current switched off, since the spark discharges deteriorate the surface integrity of the ground surface. In this light, a thermal model for *Electro-discharge diamond surface grinding (EDDSG)* with zero current in which whole workpiece and a part of the grinding wheel are dipped in dielectric is presented by considering a moving heat source over the

top surface of the workpiece. The temperature field within the high speed steel workpiece has been numerically predicted for metal bonded diamond wheel by using FEM. Special attention has been paid to study the effects of heat flux magnitude and its distribution within contact length, table speed, and depth of cut on top surface temperature distribution.

On the basis of the analysis reported in this thesis, a deep understanding about EDDG process can be made. The models presented are able to capture the major trends of surface characteristics of the machined workpiece. The theoretical approach applied is somewhat preliminary. As a future work, improvement can be made for the comprehensive surface integrity model.

At the end it can be said that in this thesis, 3-D temperature distribution in the workpiece, during a new hybrid machining process called electro-discharge diamond grinding (EDDG), has been obtained by using 2-D temperature analysis of cut-off grinding and axisymmetric temperature analysis of electro-discharge machining (EDM). Thermal stress analysis has also been done for EDM and cut-off grinding separately. EDDSG with zero current has also been analyzed for temperature distribution in the workpiece.

Contents

List of Figures	xv
List of Tables	xxi
Nomenclature	xxii
1. Introduction and Literature Review	
1.1 Machining of Advanced Engineering Materials	1
1.2 Hybrid Machining Processes	4
1.3 Electro-Discharge Diamond Grinding (EDDG)	9
1.4 Modeling of Machining Processes	10
1.5 Literature Survey	12
1.5.1 Experimental Investigations of EDDG	12
1.5.2 Thermal Modeling of Grinding	16
1.5.3 Thermal Modeling of EDM	20
1.6 Scope and Objectives of the present work	23
1.7 Organization of the thesis	24
2 Thermal Analysis of EDDG	
2.1 Introduction	25
2.2 Thermal Analysis of Cut-off grinding	28
2.2.1 Mathematical Modeling	29
2.2.2 Finite Element Formulation	30
2.2.3 Results and Discussion	39
2.3 Thermal Analysis of EDM	45
2.3.1 Mathematical Modeling	45
2.3.2 Finite Element Formulation	48
2.3.3 Results and Discussion	54

2.4	Temperature Distribution in EDDG process	59
2.4.1	Theory of Superposition	59
2.4.2	Results and Discussion	60
2.5	Conclusions	79
3	Thermal Stress Analysis of EDDG	
3.1	Introduction	81
3.2	Thermal Stresses in Cut-off Grinding	82
3.2.1	Mathematical Modeling	83
3.2.2	Finite Element Formulation	86
3.2.3	Results and Discussion	88
3.3	Thermal Stresses in EDM	95
3.3.1	Mathematical Modeling	96
3.3.2	Finite Element Formulation	99
3.3.3	Results and Discussion	102
3.4	Conclusions	109
4	Thermal Analysis of Electro-Discharge Diamond Surface Grinding	
4.1	Introduction	111
4.2	Mathematical Modeling	112
4.3	Finite Element Formulation	120
4.4	Results and Discussion	126
4.5	Conclusions	131
5	Conclusions and Scope of Future Work	
5.1	Conclusions	133
5.2	Scope for Future Work	135
	References	137
	Appendix A	147

List of Figures

Fig. 1.1 Schematic diagram of EDM process	3
Fig. 1.2 Experimental set-up for EDDG 1. Metal bonded diamond grinding wheel 2. Workpiece 3. Variac. It also shows the arrangement for temperature measurement during EDDG	9
Figure 1.3 (a) Effect of applied voltage on specific grinding forces (b) Effect of pulse on-time on MRR for different wheel speed and (c) Effect of pulse on-time on MRR for different current, in EDDG [28]	14
Figure 1.4 (a) Effect of wheel speed on MRR for different current (b) Effect of current on the specific grinding energy for different wheel speed during EDDG [29]	15
Figure 1.5 (a) Effect of current on normal force for different pulse on-time (cemented carbide workpiece) [30] (b) Effect of current on tangential force for different duty cycle (HSS workpiece) [31]	15
Fig. 2.1 Schematic of EDDG process in cut-off grinding mode	26
Fig. 2.2 Interaction of grain and spark with workpiece	26
Fig 2.3 Thermal model of cut-off grinding	29
Fig 2.4 Finite element mesh of workpiece in cut-off grinding	33
Fig. 2.5 Temperature variations with time during dry cut-off operation (a) depthwise, (b) at the top surface for $U_o = 13.58$ GPa and $R_{wg} = 0.31$ at $V_f = 3.2$ mm/s	39
Fig 2.6 Depthwise temperature Variations with time during dry cut-off operation at $V_f = 9.35$ mm/s (a) $R_{wg} = 0.27$ and $U_o = 6.2$ GPa (b) $R_{wg} = 0.31$ and $U_o = 13.58$ GPa	40
Fig 2.7 Top surface temperature variations during dry cut-off operation for different feed rates after 2.5 s of grinding (a) $U_o = 13.58$ GPa and $R_{wg} = 0.31$ (b) U_o and R_{wg} are feed dependent and selected from table 2.2	42
Fig 2.8 Depthwise temperature variations during dry cut-off operation for different V_f after 2.5 s of grinding (a) $U_o = 13.58$ and $R_{wg} = 0.31$ (b) U_o and R_{wg} are feed dependent and selected from table 2.2	42
Fig 2.9 Temperature variations during dry cut-off grinding using alumina wheel for different R_{wg} at $U_o = 13.58$ GPa and $V_f = 6.4$ mm/s after 2.5 s of grinding (a) along depth (b) top surface	43

- Fig 2.10 Temperature variations during dry cut-off grinding using alumina wheel for different U_o at $R_{wg} = 0.27$ and $V_f = 6.4$ mm/s after 2.5 s of grinding (a) along depth (b) top surface 44
- Fig 2.11 Variation of top surface temperature during cut-off grinding using alumina wheel for different h_c at $V_f = 4.0$ mm/s, $U_o = 13.58$ GPa, and $R_{wg} = 0.31$ after 2.5s of grinding 44
- Fig 2.12 Variation of top surface temperature with time during cut-off grinding using (a) diamond wheel (b) alumina wheel at $V_f = 10.29$ mm/s, $U_o = 10.55$ GPa, and $h_c = 10000.0$ W/m²K (kerosene) 45
- Fig 2.13 Thermal model of EDM 49
- Fig 2.14 Finite element mesh in EDM domain 50
- Fig 2.15 Comparison of variation of top surface temperature in 5 Cr die steel workpiece during EDM with heat flux of different profiles and the results of Shankar et al [70]. $t = 60$ μ s, $t_{on} = 60$ μ s, $t_p = 120$ μ s, without considering phase change and on-/off-time effect 54
- Fig 2.16 Top surface temperature variation in 5 Cr die steel workpiece during EDM computed with Gaussian heat flux profile including the effect of phase change and on-/off- time both, after 60 μ s for $t_{on} = 30$ μ s, $t_p = 120$ μ s 56
- Fig 2.17 Variation of temperature with duty cycle (a) at top surface (b) along depth in HSS workpiece during EDM computed with Gaussian heat flux after one pulse time for $t_{off} = 100$ μ s 57
- Fig 2.18 Depthwise temperature variations in HSS workpiece during EDM with Gaussian heat flux for $t_{on} = 100$ μ s, $t_p = 200$ μ s at radial distance of (a) $r = 0$ (b) $r = R$ (c) $r = 2R$ 58
- Fig 2.19 Top surface temperature variation in HSS workpiece during EDM with Gaussian heat flux for different values of partition ratio (R_{wg}) at $t_{on} = 100$ μ s, $t_p = 200$ μ s after $t = 100$ μ s 58
- Fig 2.20 Temperature variation in HSS workpiece during EDM with Gaussian heat flux for different discharge current at $t_{on} = 100$ μ s, duty cycle=50% after $t = 100$ μ s (a) along depth from top surface (b) along radial distance from centre 60
- Fig. 2.21 (a) 3-D domain of workpiece (b) Descretization of workpiece top surface used in superposition 61

- Fig 2.22 Variation of temperature (a) at top surface along radius (b) along depth at $r=0$, of two different size of workpiece domain after 0.05 s of machining time using EDM 62
- Fig 2.23 Temperature distribution in HSS workpiece during EDDG process for $t_{on}=75 \mu s$, $t_{off}=150 \mu s$ after $t=0.05s$ (a) 3-D surface plots (b) Contour plots 64
- Fig 2.24 Top surface temperature distribution in HSS workpiece during EDDG after $t=0.05s$. (a) along x-axis at $y=1.0$ mm (along X-X in Fig. 2.21 b) (b) along y-axis at $x=3.5$ mm (along Y-Y in Fig. 2.21 b). $t_{on}=75 \mu s$, $t_{off}=150 \mu s$ 65
- Fig 2.25 Depthwise temperature distribution in HSS workpiece during EDDG process after $t=0.05s$ at (a) $x=1.0$ mm and $y=1.0$ mm (Point A), (b) $x=1.5$ mm and $y=1.0$ mm (Point B), (c) $x=1.0$ mm and $y=0.5$ mm (Point C), (d) $x=1.5$ mm and $y=0.5$ mm (Point D). (Fig. 2.21b) 67
- Fig 2.26 Effect of duty cycle on temperature distribution (a) on top surface along x-axis at $y=1.0$ mm (along X-X) (b) on top surface along y-axis at $x=3.5$ mm (along Y-Y) (c) along depth at $x=1.0$ mm and $y=1.0$ mm (point A) (Fig.2.21b) in HSS workpiece during EDDG process after $t=0.05$ s for $V_f=10.29$ mm/s, $t_{on}=150 \mu s$ 68
- Fig 2.27 Effect of on-time on temperature distribution (a) at top surface along x-axis at $y=1.0$ mm (along X-X) (b) along depth at $x=1.0$ mm and $y=1.0$ mm (Point A) (Fig. 2.21b) in HSS workpiece during EDDG process after 0.05 69
- Fig 2.28 Effect of feed velocity on top surface temperature distribution in HSS workpiece during EDDG process after 0.05 s (a) along x-axis at $y=1.0$ mm (along X-X in Fig. 2.21 b) (b) along y-axis at $x=3.5$ mm (along Y-Y in Fig. 2.21 b) 70
- Fig 2.29 Effect of feed velocity on temperature distribution along depth in HSS workpiece during EDDG after 0.05 s at (a) $x=1.0$ mm and $y=1.0$ mm (Point A Fig. 2.21 b) (b) $x=1.0$ mm and $y=0.5$ mm (Point C Fig. 2.21 b) 71
- Fig 2.30 Effect of current on temperature distribution (a) top surface along x-axis at $y=1.0$ mm (along X-X) (b) top surface along y-axis at $x=3.5$ mm (along Y-Y). (c) along depth in at $x=1.0$ mm and $y=1.0$ mm (Point A) (Fig. 2.21 b) in HSS workpiece during EDDG after 0.05 s 72
- Fig 2.31 Effect of R_{ws} on top surface temperature distribution in HSS workpiece during EDDG process after 0.05 s (a) along x-axis at $y=1.0$ mm (along X-X in Fig. 2.21b) (b) along y-axis at $x=3.5$ mm (along Y-Y in Fig. 2.21b) 73

- Fig 2.32 Effect of R_{ws} on temperature distribution along depth in HSS workpiece during EDDG process after 0.05 s at (a) $x=1.0$ mm and $y=1.0$ mm (Point A Fig. 2.21 b) (b) $x=1.0$ mm and $y=0.5$ mm (Point C Fig. 2.21b) 74
- Fig 2.33 Effect of grinding time on top surface temperature distribution in HSS workpiece during EDDG process (a) along x-axis at $y=1.0$ mm (along X-X in Fig. 2.21b) (b) along y-axis at $x=3.5$ mm (along Y-Y in Fig. 2.21b) 75
- Fig 2.34 Effect of grinding time on temperature distribution along depth in HSS workpiece during EDDG process (a) $x=1.0$ mm and $y=1.0$ mm (Point A Fig. 2.21b), (b) $x=1.0$ mm and $y=0.5$ mm (Point C Fig. 2.21b) 76
- Fig. 3.1 Boundary conditions applied to workpiece domain used for finding thermal stresses in cut-off grinding 85
- Fig. 3.2 Variation of (a) σ_{xx} (b) σ_{xz} (c) σ_{zz} with time at top surface during cut-off grinding of HSS workpiece for $V_f=10.29$ mm/s, $R_{wg}=0.08$, $U_o=10.55$ GPa 89
- Fig. 3.3 (a) Top surface temperature variations with time (b) temperature variation of a point on top surface at $x=0.003$ m with time during cut-off grinding for $U_o=10.55$ GPa, $R_{wg}=0.08$ and $V_f=10.29$ mm/s 90
- Fig. 3.4 Variation of (a) σ_{xx} (b) σ_{xz} (c) σ_{zz} with time along depth at the centre of HSS workpiece during cut-off grinding for $V_f=10.29$ mm/s, $R_{wg}=0.08$, $U_o=10.55$ GPa 91
- Fig. 3.5 (a) Depthwise temperature variations with time (b) temperature variation of two points at different depths with time during cut-off grinding for $x=0.003$ m, $U_o=10.55$ GPa, $R_{wg}=0.08$ and $V_f=10.29$ mm/s 92
- Fig. 3.6 Variation of (a) σ_{xx} (b) σ_{xz} and (c) σ_{zz} at top surface with V_f during cut-off grinding of HSS workpiece for $R_{wg}=0.08$, $U_o=10.55$ GPa and machined depth 5 mm 93
- Fig. 3.7 Variation of (a) σ_{xx} (b) σ_{xz} and (c) σ_{zz} along depth at $x=0.003$ m with V_f during cut-off grinding of HSS workpiece for $R_{wg}=0.08$, $U_o=10.55$ GPa and machined depth 5 mm 94
- Fig. 3.8 Boundary conditions applied to workpiece domain used for finding thermal stresses in EDM 99

- Fig. 3.9 Variation of stress components in HSS workpiece for $U_b = 40$ V, $I = 8$ A, $R_{ws} = 0.08$, $R = 125$ μm , $t_{on} = 100$ μs , duty cycle = 50%. Results after 100 μs (a) along the radial distance at 7 μm below from the top surface (b) along depth at $r = 7$ μm 103
- Fig. 3.10 Equivalent isostress (N/m^2) due to one spark within $R/2$ from the center (within one critical element) in HSS workpiece at $U_b = 40$ V, $I = 8$ A, $R_{ws} = 0.08$, $R = 125$ μm , $t_{on} = 100$ μs , duty cycle = 50% 104
- Fig. 3.11 Isotherms (K) due to one spark within $R/2$ from the centre (within one critical element) in HSS workpiece at $U_b = 40$ V, $I = 8$ A, $R_{ws} = 0.08$, $R = 125$ μm , $t_{on} = 100$ μs , duty cycle = 50%. Results after 100 μs 104
- Fig. 3.12 Variation of stress components with duty cycle along radius in HSS workpiece at 7 μm below from the top surface for $U_b = 40$ V, $I = 8$ A, $R_{ws} = 0.08$, $R = 125$ μm , $t_{off} = 100$ μs (a) σ_{rr} (b) $\sigma_{\theta\theta}$ (c) σ_{rz} (d) σ_{zz} . Results after one on-time 105
- Fig. 3.13 Variation of stress components with duty cycle along depth in HSS workpiece at $r = 7$ μm from the center of the spark for $U_b = 40$ V, $I = 8$ A, $R_{ws} = 0.08$, $R = 125$ μm , $t_{off} = 100$ μs (a) σ_{rr} (b) $\sigma_{\theta\theta}$ (c) σ_{rz} (d) σ_{zz} . Results after one spark on-time 106
- Fig. 3.14 Variation of components of thermal stresses with current along radius in HSS workpiece at 7 μm below from the top surface for $U_b = 40$ V, $I = 8$ A, $R_{ws} = 0.08$, $R = 125$ μm , $t_{off} = 100$ μs , duty cycle = 50% (a) σ_{rr} (b) $\sigma_{\theta\theta}$ (c) σ_{rz} (d) σ_{zz} . Results after 100 μs 107
- Fig. 3.15 Variation of components of of thermal stresses with current along depth in HSS workpiece at $r = 7$ μm for $U_b = 40$ V, $I = 8$ A, $R_{ws} = 0.08$, $R = 125$ μm , $t_{off} = 100$ μs , duty cycle = 50% (a) σ_{rr} (b) $\sigma_{\theta\theta}$ (c) σ_{rz} (d) σ_{zz} . Results after 100 μs 108
- Fig. 4.1 Configuration of EDDSG 112
- Fig. 4.2 Thermal model used for EDDSG with negligible current 113
- Fig. 4.3 Different heat flux profiles used for thermal model of surface grinding (i) Rectangular heat flux (ii) Right angle triangular heat flux (iii) Square law heat flux distribution 115
- Fig. 4.4 Variation of (a) thermal conductivity, (b) specific heat with temperature 119
- Fig. 4.5 The finite element mesh of the workpiece used in EDDSG 122

- Fig. 4.6 Variation of top surface temperature during surface grinding computed with heat source of different shapes and the results of Li and Chen [80] 126
- Fig. 4.7 Effect of material thermal properties on top surface temperature at $V_w = 50$ mm/sec and $d=0.04$ mm after 0.224 s 127
- Fig. 4.8 Effect of cooling on top surface temperature at $V_w = 50$ mm/sec and $d=0.04$ mm after 0.224 s 128
- Fig. 4.9 Variation of temperature with time (a) at top surface (b) at a point on top surface ($x= 10.5$ mm) after different time for $V_w = 50$ mm/sec and $d=0.04$ mm 129
- Fig. 4.10 Top surface temperature variation for different depth of cut (d) at $V_w = 50$ mm/sec after $t = 0.224$ s 129
- Fig. 4.11 Top surface temperature variation along x-axis for different table speed at $d = 0.04$ mm after table travel of 11.2 mm 130
- Fig. 4.12 Top surface temperature variation for different wheel diameter at $V_w = 50$ mm/sec and $d=0.04$ mm after $t = 0.224$ s 131

List of Tables

Table 1.1 Interaction of different machining processes to develop a hybrid-machining process	5
Table 1.2 Classification of Hybrid Machining Processes	7
Table 1.3 Key developments in thermal modeling of Grinding	17
Table 1.4 Key developments in thermal modeling of EDM	22
Table 2.1: Properties of workpiece used for Figures 2.5-2.11 [71]	77
Table 2.2: Feed dependent values of R_{wg} and U_o for AISI 1020 steel workpiece and resin bonded Al_2O_3 wheel [71]	77
Table 2.3: Properties of HSS workpiece used in present model [70]	77
Table 2.4: Properties of workpiece used for Figures 2.15-2.16 [70]	78
Table 2.5: Process parameters used for Figures 2.15-2.16	78
Table 2.6: Process parameters used for Figures 2.17-2.36	78
Table 3.1 Details of on-time, off-time and pulse time for different duty cycle	105
Table 4.1: Data related to thermal properties of grinding wheel and workpiece, and process parameters used by Li and Chen [80]	126
Table 4.2: Process parameters used in the present model	127

Nomenclature

$[A]$	Matrix of A
$\{A\}$	Column vector of A
B	Width of the Workpiece (m)
$[B]$	Matrix of differential coefficients of shape functions
C	Specific heat workpiece (J / kg K)
C_s	Specific heat of workpiece in solid state (J / kg K)
C_l	Specific heat of workpiece in liquid state (J / kg K)
D	Diameter of wheel (m)
d	Depth of cut (m)
$[D]$	Elasticity matrix
E	Young's modulus (N/ m ²)
h_c	Convective heat transfer coefficient (W / m ² K)
H	Height of the workpiece
$ J $	Determinant of Jacobean matrix
k	Thermal conductivity (W / m K)
L	Length of Workpiece (m)
L_m	Latent heat of melting (J/kg)
L_v	Latent heat of vaporization (J/kg)
l_c	Geometrical length of contact (m)
l_e	Effective contact length (m)
n	Normal
$\{N^e\}$	Column vector of 2-D bilinear elemental shape functions
q	Heat flux (W / m ²)
R_{wg}	Partition coefficient to workpiece due to grinding
R_{ws}	Partition coefficient to workpiece due to EDM
R	Radius of spark (m)
r	Radial coordinate(m)
S	Deviatoric component of stress (N/ m ²)
T	Temperature (K)
\dot{T}	Derivative of temperature with time
T_o	Ambient Temperature (K)
T_m	Melting temperature (K)
T_v	Vaporization temperature (K)
t	Time (s)
U_o	Specific energy of workpiece material (J/ m ³)
U_b	Discharge voltage (Volt)
V_f	Feed velocity(m/s)
V_s	Wheel velocity(m/s)
W	weighting function
$\{W^e\}$	Vector of elemental nodal weighting functions
x ,y,z	Cartesian Coordinate x, y and z

r, θ, z Cylindrical coordinate r, θ and z

Greek symbols

Γ	Boundary
α	Thermal diffusivity (m^2/s)
α_t	Coefficient of thermal expansion ($1/^\circ\text{C}$)
α_w	Thermal diffusivity of workpiece material (m^2/s)
$\{\delta\}$	Nodal displacement vector (m)
$\{\varepsilon\}$	Strain vector
Ω	Domain
ϕ	Distribution function
η	Perpendicular to axis ξ
ν	Poisson's ratio
θ	Constant
$\{\sigma\}$	Stress vector (N/m^2)
σ_{eq}	Equivalent stress (N/m^2)
σ_y	Yield stress (N/m^2)
ρ	Density (kg/m^3)
ξ	Moving co-ordinate parallel to x-axis

Subscripts

avg	Average, grinding
i	Initial at time = 0
o	Ambient condition
w	Workpiece
wg	Workpiece, grinding
ws	Workpiece, sparking
s	Wheel

Superscript

b	Boundary element
e	Element
T	Transpose

Chapter 1

Introduction and Literature Review

1.1 Machining of Advanced Engineering Materials

Advanced engineering materials are having greatly improved thermal, chemical and mechanical properties such as improved strength, heat resistance, wear resistance, and corrosion resistance [1]. Applications of these materials lie in those areas where high specific characteristics are needed. Titanium-based or nickel based superalloys, engineering ceramics and composites are widely used advanced engineering materials. Use of these materials has been escalating rapidly during the past few decades.

Cemented carbides are enjoying an ever-increasing popularity in industry and especially used for metal-forming dies, cutting tools, and components requiring high resistance to wear. *Polycrystalline diamond (PCD)* is widely used for cutting tools, rock-drilling bits, wire-drawing dies, spray nozzle blanks, and different wear-resistant parts due to its unique properties of high strength and high toughness. *Titanium and its alloys* are very attractive materials for several engineering applications due to their high strength to weight ratio and excellent corrosion resistance [2]. The major application of these materials are in the aerospace industry, where it is used both in airframes and engine components.

Ceramic materials are employed on account of their special thermodynamic and mechanical properties, their light weight characteristics, high flexural strength in conjunction with low density, high hardness and brittleness, accompanied by certain degree of chemical resistance and high compressive strength even at high temperatures [3,4]. Important ceramic materials are aluminium oxide (Al_2O_3), zirconium oxide (ZrO_2), titanium oxide (TiO_2), Silicon nitride (Si_3N_4) and silicon carbide (SiC). Silicon nitride is one of the difficult-to-cut advanced materials having wide applications in gas turbines, rocket engines, melting crucibles, and for balls and rollers. Apart from these, other attractive ceramic materials are boron carbide (B_4C), SiSiC and C/SiC . *Particle reinforced metal matrix composites (PRMMCs)* are a class of advanced materials with a wide potential for application in the automotive and aerospace industries [5]. In this

group of material, hardness, strength and resistance of the reinforcement are combined with the ductility and toughness of a matrix material. Aluminium is one of the most frequently used matrix materials due to its low density. Silicon carbide particle reinforced aluminium MMC is often used in the automotive industries.

These materials are also called as *advanced difficult-to-machine materials* because of difficulty in machining due to improved material properties. Shaping and/or finishing of advanced difficult to machine materials with stringent design requirements such as high precision, complex shapes and high surface quality is inevitable to put them in use. To achieve these objectives through traditional machining techniques, cutting tools with super qualities are needed, which are yet to be developed. Machining of these super hard materials with complex shapes have open the way to develop novel, cost-effective, rapid material removal techniques that are no longer based on pure mechanical cutting. Therefore, to exploit these difficult-to-machine advanced engineering materials with new challenges, it was perceived to develop advanced machining processes (AMPs) [6].

These AMPs have *been classified* [6] into four basic categories. First category includes various mechanical processes such as abrasive/water jet machining (A/WJM), ultrasonic machining (USM), abrasive flow machining (AFM) and magnetic abrasive machining (MAM) etc. Second category includes thermal processes such as electrical discharge machining (EDM), laser beam machining (LBM), electron beam machining (EBM) etc. Third category includes bio-chemical and different chemical processes such as chemical milling (CHM), chemical blanking (CHB), photochemical machining (PCM) and bio-chemical machining (BCHM). Electro-chemical machining (ECM) is placed in fourth category.

Electrical discharge machining is perhaps the most widely used AMP in the present day industries [7]. The scope of the EDM process ranges from the drilling of micro-holes that are smaller than a human hair to machining of 1,00,000-pound automotive dies. EDM can also be used to drill holes with high aspect ratio (upto 100:1). It is now believed to account for over 2% of all machining. The remarkable success of the application of EDM in machining can be appraised by considering the fact that many non-conducting materials, just for sake of machining, are rendered electrically conductive

to the level (>0.01 /ohm-cm) required for electro-discharge processing. It is achieved by doping non-conducting material with conductive elements.

EDM is basically a thermal process [6-7] where material is removed by utilizing high-density thermal energy. In EDM, two electrically conductive electrodes, one being the tool of a predetermined shape, and other being the workpiece, are immersed in a liquid dielectric, such as paraffin or light oil (Fig. 1.1). Kerosene is a very common dielectric fluid used. EDM is accomplished with a system comprising two major components: a machine tool and a power supply. The workpiece is mounted on the table of the machine tool and the tool electrode is attached to the ram of the machine. The advancing of tool electrode into the workpiece is controlled automatically by the servo control system. The power supply produces a high frequency series of electrical spark discharges between the tool electrode and the workpiece through servo control system.

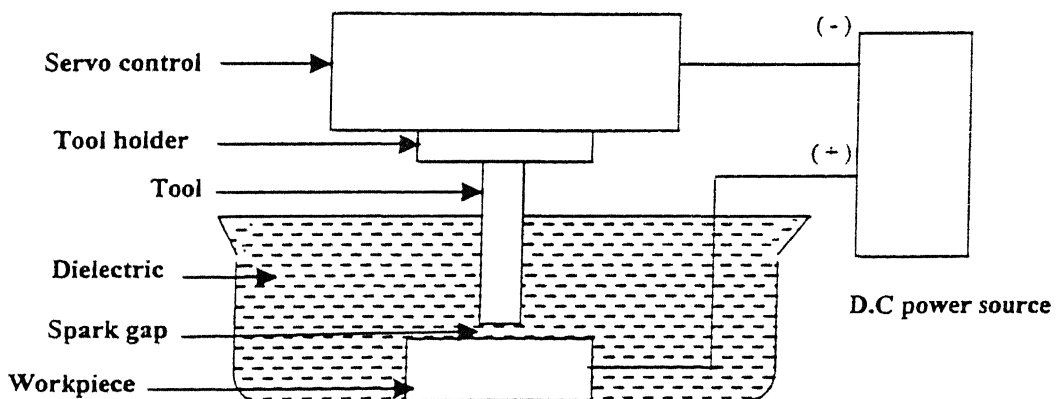


Fig. 1.1 Schematic diagram of EDM process

During EDM, pulsed DC of 80-100 V and approximately 5Hz-5kHz frequency is passed through the electrodes, which are separated by a small gap (typically 0.01-0.5 mm). Localized electrical breakdown of the dielectric occurs and sparks are generated preferentially at the closest locations (narrowest gap) between the two electrode surfaces where local electric field is highest. Each spark *melts and vaporizes* (i.e. erodes) a tiny amount of material from the surfaces of both the electrodes (tool and workpiece). The required discharge conditions are achieved by servo-controlled feed motion. Polarity of electrodes is selected in such a way that substantially more material is removed from the workpiece than from the tool electrode.

There are several ways to apply spark energy for different types of operations depending on the type of the tool used. There are three main categories into which EDM based operations can be divided: *sinking, cutting (including wire cutting) and grinding*. As the name indicates electrical discharge sinking is most suited to make irregularly shaped holes, slots and cavities without any tool wander. Travelling wire EDM removes material by electrical discharge erosion with a wire electrode traveling longitudinally through the workpiece. It is widely used to cut punches and dies, shaped pockets and many other industrial applications. Electro-discharge sawing operation is similar to mechanical band sawing where tool electrode is in the form of a continuously moving band saw made of mild steel.

Rotating disc EDM (RD-EDM) [8] uses a rotating electrically conductive wheel (similar in size to a standard abrasive grinding wheel) as the tool electrode. This process is used as an effective alternate for sharpening carbide and diamond tipped cutting tools, thus reducing the high cost of using diamond grinding wheels. Double rotating disc electrodes EDM (DRD-EDM) uses two rotating electrodes to erode a rotating workpiece. Different combinations of relative positions and angular velocities of tool electrodes and workpiece can produce various workpiece shapes. By keeping identical angular velocities of the two axes, high precision spirals can be generated with a diameter error less than 0.004 mm, circular error less than 0.002 mm and surface roughness of Ra 63 nm.

Technological improvements of AMPs can be achieved by combining different physico-chemical action on the material being processed [6]. The machining process so developed is called *hybrid-machining process* (HMP). In particular a mechanical action, which is used in conventional material removal processes, can be combined with unconventional machining action such as mechanical, thermal, or electro-chemical.

1.2 Hybrid Machining Processes

Recently, *hybrid-machining* processes, which are combination of two or more machining processes, have attracted special interest in the field of machining advanced engineering materials [9]. These processes are developed to exploit the potential advantages and to restrict the disadvantages associated with an individual constituent process. Usually, the performance of hybrid process is better than the sum of their

Table 1.1 Interaction of different machining processes to develop a hybrid-machining process

	Thermal Processes				Chemical and Electro-chemical Processes		Mechanical Processes			
	EDM	LBM	EBM	PBM	CHM	ECM	ABRASION (A)	USM	FLOW (F)	CUTTING (C)
Thermal Processes	EDM					ECM				
		LBM			LAE	LAECM	EDAG	UAEDM		
			EBM					UALBM		LAT
				PBM						
Chemical and Electro-chemical Processes	CHM				CHM		EEM			PAT
	ECM	EALBM				ECM	ECAG/ECAM	UAECM	CHP	
Mechanical Processes	ABRASION(A)									
	USM	UALBM			EEM	ECAG	AM	UAG	UAG	
	FLUID FLOW (F)				CHP			UAP	FFM	
	CUTTING(C)	LAT		PAT				UAT		CUTTING

- AM: Abrasive Machining
- CHM/CHP: Chemical Machining/ Chemical Polishing
- EALBM: Etching Assisted Laser Beam Machining
- EBM: Electron Beam Machining
- ECAG/ECAM: Electro-Chemical Abrasive Grinding/ Electro-Chemical Abrasive Honing
- ECSCM/ECAM: Electro-chemical Spark /Arc Machining
- EDM: Electro- Chemical Machining
- EDAG: Electro- Discharge Abrasive Grinding
- EDM: Electrical Discharge Machining
- EEM: Elastic Emission Machining
- FFM: Fluid Flow Machining
- LAE: Laser Assisted Etching
- LAECM: Laser Assisted Electro-chemical Machining
- LAT: Laser Assisted Turning
- LBM: Laser Beam Machining
- PAT: Plasma Assisted Turning
- PBM: Plasma Beam Machining
- UAECM: Ultrasonic Assisted Electro-chemical Machining
- UAEDM: Ultrasonic Assisted Electrical Discharge Machining
- UAG: Ultrasonic Assisted Grinding
- UALBM: Ultrasonic Assisted Laser Beam Machining
- UAP: Ultrasonic Assisted Polishing
- UAT: Ultrasonic Assisted Turning

performance with the same parameter settings. In some of these processes, besides the performance from individual component processes, an additional contribution may also come from the interaction of the component processes [9]. Table 1.1 shows the major hybrid machining processes either used in industries or under development stage.

HMPs are either electrical energy based (called as *electrical hybrid machining processes*) or mechanical energy based (called *abrasive hybrid machining processes*). Table 1.2 shows the classification of hybrid machining processes based on their energy sources, material removal mechanism, tool used and medium in which process is performed.

Electrical hybrid machining processes are conceived to overcome the major limitation of ECM and EDM in which tool and workpiece are required to be electrically conducting and also to increase the productivity. Electrochemical arc machining (ECAM) and Electrochemical spark machining (ECSM) are such hybrid machining processes in which the phenomenon of electro-chemical discharge is employed for material removal [10-12] from electrically conductive and nonconductive materials respectively. In ECAM, discharge takes place between the tool and the workpiece due to breakdown of entrapped hydrogen gas bubbles causing erosion of both the electrodes. The productivity of ECAM is reported [9, 10] to be 5 to 50 times greater than the productivity using individual process of ECM and EDM. On the other hand, in ECSM the discharge takes place (in the form of desirable sparks) between the tool and the surrounding electrolyte in the vicinity of the electrically non-conducting material workpiece.

These processes have been successfully applied for the machining of soda lime glass, borosilicate glass, quartz, glass fiber reinforced plastics, and ceramics [13]. These processes can be used for hole drilling, die sinking and wire cutting for machining/cutting of composites and partially conducting ceramics [12]. ECAM/ECSM are specifically effective when dealing with materials with tensile strength higher than 1500 N/mm^2 and heat resistance alloys. Machining capacity of the order of $104 \text{ mm}^3/\text{min}$, accuracy of $0.04\text{-}0.02 \text{ mm}$ and surface roughness of $R_a = 1.25\text{-}2.5 \text{ mm}$ are obtained [9].

Ultrasonic assisted electro-chemical machining (UAECM) and ultrasonic assisted electro-discharge machining (UAEDM) are developed by combining ultrasonic

machining (USM) with ECM or EDM respectively [9]. UAEDM has been found [14-15] to increase

Table 1.2 Classification of Hybrid Machining Processes

Major Source of Energy	Process	Combination of Energy Sources	Mechanism of Material Removal	Tool	Transfer Media
Thermal	UAEDM	Thermal and Ultrasonic Vibration	Melting & Evaporation	Sonotrode	Dielectric
	UALBM	Thermal and Ultrasonic Vibration	Melting & Evaporation	Laser beam	Air
Electrochemical and Chemical	ECSM /ECAM	Electrochemical and Thermal	Melting and Evaporation	Electrode	Electrolyte
	ECAG	Electrochemical and Mechanical	Electrochemical dissolution and abrasion	Metal bonded abrasive wheel	Electrolyte
	LAECM	Electrochemical and Thermal	Electrochemical dissolution and heating	Electrode	Electrolyte
	UAECM	Electrochemical and Ultrasonic Vibration	Electrochemical dissolution	Sonotrode	Electrolyte
	BEDMM	Electrochemical Thermal, and Mechanical	Electrochemical, Melting and Mechanical Rupture	Rotating Metal brush	Water glass solution in water
	LAE	Chemical and Thermal	Chemical dissolution and heating	Mask	Etchant
Mechanical	EDAG	Mechanical and Thermal	Melting, Evaporation and abrasion	Metal bonded abrasive wheel	Dielectric
	LAT/PAT	Mechanical and Thermal	Shearing and Heating	Turning tool	Air
	UAG	Mechanical and Ultrasonic Vibration	Abrasion	Sonotrode of abrasive wheel	Coolant
	UAT	Mechanical and Ultrasonic Vibration	Shearing	Turning tool	Air

MRR and grinding ratio while lowering grinding forces for hard materials like WC and TiB₂. Hot machining has also been tried on advanced materials. Softening of materials by localized heating with aid of a plasma jet [16] or a laser beam [17] facilitates substitution of grinding by other machining processes that are less expensive.

The **abrasive hybrid machining processes** are developed [9] by combining EDM, ECM, or USM with abrasive machining, and they are most commonly used in industries. These can be classified in three main subgroups: Electro-Discharge Abrasive Machining (EDAM), Electrochemical Abrasive Machining (ECAM) and Electro-Chemical Spark Abrasive Machining (ECSAM). Electro-chemical abrasive grinding (ECAG), Electro-discharge abrasive grinding (EDAG) and Electro-chemical abrasive honing (ECAH) use abrasive tool with metallic bond. Electro-chemical abrasive finishing (ECAAF), Electro-discharge abrasive finishing (EDAF) and ultrasonic assisted electro-chemical machining (UAECM) use free abrasive grains.

Electro-chemical abrasive grinding (ECAG) with metal bonded rotating abrasive tool is a combined process of mechanical grinding and ECM [9]. An increase in performance index of this process is due to improvement in surface layer properties and reduction in tool wear and energy consumption. ECAG is particularly effective for machining parts made of difficult to cut materials, such as sintered carbides, creep resisting alloys (e.g. Inconel and Nimonic), metallic composites (e.g. PCD-Co, Al-SiC, Al-Al₂CO₃), etc [9]. In this process, about 90% of the material is removed by electro-chemical means and rest by abrasion [6]. Better surface finish can also be obtained after machining non-homogeneous materials like cemented carbide. The quality of surface machined by this process is independent of mechanical properties of workpiece. Since the dimensional accuracy obtained in ECAG is not as good as in conventional grinding, it is normal practice to finish components with no-electro-chemical material removal (or zero current).

Electro-discharge abrasive grinding (EDAG) is a hybrid machining process involving EDM and Grinding. The combination of metal bonded diamond grinding and EDM is the only one so far experimentally successful hence more specifically this hybrid process is called as **Electro-discharge diamond grinding (EDDG)**. In this process, synergetic interactive effect of electro-discharge action and abrasion action are employed to increase machining performance. The electrical discharges of EDDG cause considerable decrease in grinding forces, and grinding wheel wear; and also effectively resharpen the grinding wheel. The abrasive action in this process helps to increase metal removal rate (MRR) and surface quality. The EDDG of advanced engineering materials

has been found to be feasible and advantageous. The details about the working of EDDG process are discussed in the next section.

1.3 Electro-Discharge Diamond Grinding

Figure 1.2 shows a schematic diagram of EDDG system, which is built on an EMS 5535-R 50 EZNC die sinking EDM with a provision to rotate the grinding wheel and thermocouple arrangement for measuring temperature in the workpiece. The rotation to the grinding wheel, about an axis parallel to the machine table, is given by using a grinding spindle assembly and a variable-speed drive mounted on the ram of the machine. While machining, the rotating wheel is fed under servo control. The metallic bonding material of the grinding wheel and workpiece surface physically separated by a gap, the magnitude of which depends as the local breakdown strength of dielectric for a particular gap voltage setting.

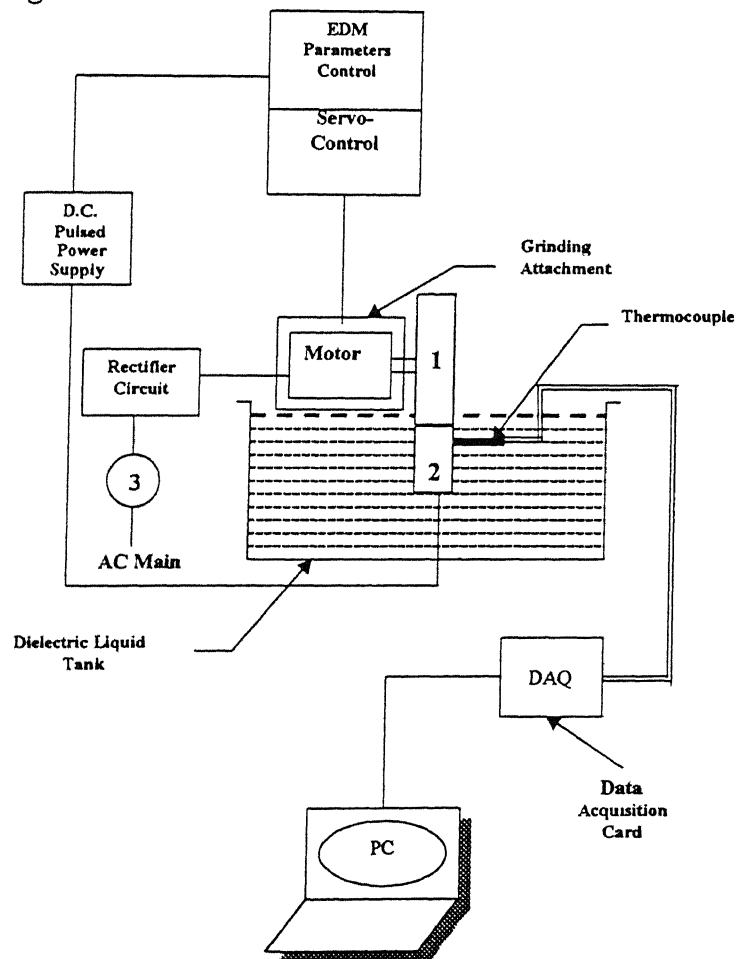


Fig. 1. 2 Experimental set-up for EDDG 1. Metal bonded diamond grinding wheel 2. Workpiece 3. Variac. It also shows the arrangement for temperature measurement during EDDG.

In EDDG process, mechanical grinding and electro-discharge erosion can be controlled by adjusting wheel feed rates and electro-discharge pulse parameters. The improved grinding performance in EDDG is due to continuous in-process dressing and declogging of the grinding wheel. Consequently, the grinding wheel can maintain its grinding ability without becoming dull. Since the contributions of mechanical abrasion and thermal erosion to process performances are adjustable, the EDDG can be used either in a grinding dominant state with a relatively less effect of electrical discharge to acquire a reduced heat-affected surface layer, or in an EDM dominant state with a relatively less effect of grinding to reduce machining force, or in a well balanced state between the grinding and EDM. Applications of this process include machining of components made of advanced engineering materials such as Al-SiC composites (duralcan), inconel, titanium alloy, tungsten carbide, high speed steel (HSS), cemented carbide, polycrystalline diamond etc.

1.4 Modeling of Machining Processes

The modeling of machining process can be defined from the manufacturing engineer's point of view as: simplified mathematical formulation of a machining process which establishes a relation between input and output quantities in order to describe the dynamic as well as the static performance of the machining process. The purpose of modeling a machining operation is to develop predictive capability for machining performance well in advance and finally to achieve optimum productivity, quality, and cost [18].

There are many reasons why the mathematical model of a machining operation may be required. Some of the reasons are [19]:

1. Simulation of process
2. Design and optimization of process
3. Control of process.

Analytical, Experimental, Mechanistic, Numerical, Artificial Intelligence (AI) and Stochastic methods are among the most commonly used ones for predictive modeling [10, 20]. In recent years, hybrid-modeling techniques, which are combination of some of these methods, are becoming more popular.

An analytical model [20] is deductively derived from basic physical principles. Relationships between the parameters, borrowed from physics, mechanics and material science, which have worked well in previous instances, are used. The main advantage of analytical models is that the results can easily be transferred to other machining conditions. Analytical models can be purely deterministic or augmented by probabilistic or stochastic considerations. A large number of unrealistic assumptions (to make problem simple and solvable) are the major limitation of analytical modeling.

An experimental (or empirical) modeling, on the contrary, is developed by means of measured values, which have been obtained in machining tests. In experimental modeling, the model parameters are determined on the basis of measured values and regression analysis methods. Every experimental model can be used for accurate description of the machining operation under the specified machining conditions only. However, compared to analytical models, the development of empirical models requires minimum efforts. Consequently, experimental models are used in all field of machining technology.

Mechanistic methods of modeling are of more recent origin [21]. This modeling is a combination of analytical and experimental modeling techniques. Artificial intelligence (AI) based modeling [21] is a new brand of modeling machining processes using artificial neural network (ANN), expert systems and Fuzzy Logic. Unlike analytical models which provide explicit models with deep physical understanding, ANN provide implicit models captured within the weight matrices of the net. They facilitate learning from prior experimental data but, not yet, from prior analytical insights.

Another class of modeling methods, which is the only recourse to make quantitative predictions of complex real engineering problems, is numerical method [18,21]. At present several numerical methods are available, namely, finite difference method (FDM), finite element method (FEM), finite volume method (FVM), spectral method, boundary element method (BEM) etc for solving different types of engineering problems. Each of these techniques has its own potential advantages and weaknesses. FEM is a versatile method that can solve a wide range of different engineering problems of complex geometry, heterogeneous materials, varying loading and different boundary conditions. In view of these flexibilities, FEM has been employed for modeling of

machining processes in recent years. The major limitations of applying FEM for modeling of machining processes are large computational burden and incorporation of dynamic aspects.

The foregoing discussion clearly indicates that modeling of EDDG process for various aspects are needed to obtain deep understanding about the process behaviors. The following section provides a review of the relevant literature available.

1.5 Literature Survey

The Electro-Discharge Diamond Grinding (EDDG) has been developed in USSR during late seventies. But in late 80s its applications gained momentum in various industries where there is a need to grind parts made of difficult-to-machine materials. EDDG process is in its early stage of development and publications available are scarce. Most of the researchers have conducted experiments to investigate the effects of process parameters on its performance. Theoretical treatment of EDDG process is almost nil. An extensive literature survey yield few references related to experimental studies on EDDG and theoretical treatment of its constituent processes, e.g. EDM and Grinding. A brief review as given below, is presented in three parts, viz. experimental investigation of EDDG, thermal modeling of grinding and thermal modeling of EDM.

1.5.1 Experimental Investigations of EDDG

Grodzinskii and other researchers [23-26] have done extensive experimental work on EDDG. But they all are more of an exploratory in nature. The role of electrical discharges on grinding forces, grinding wheel wear, and geometrical accuracy while grooving and cutting-off of cemented carbide and few other advanced ceramics have been experimentally studied by Aoyama and Inasaki [27]. They used electrically conducting diamond grinding wheel which is made by making grooves around the periphery of the wheel to insert resinoid bonded diamond grains of 100 μm grit size. They found that the normal and tangential grinding forces decrease with an increase in the applied voltage at the expense of an increase in wheel wear. The reasons for decrease in the grinding forces have been attributed to two factors (i) some portion of the uncut material is removed by sparks erosion, and (ii) self-sharpening of the grinding wheel due

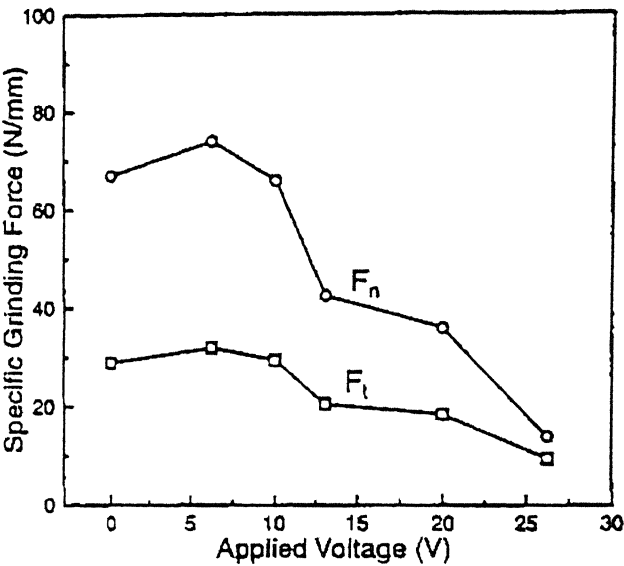
to sparks. The primary limitation of the process was found to be high wear rate of the wheel.

Rajurkar et al. [28] have reported the characteristics of EDM-grinding hybrid process, which they call Abrasive electro-discharge grinding (AEDG). Experiments have been conducted to machine Al-SiC composite, and titanium alloy with copper bonded diamond wheel. The electrical parameters, such as peak current and pulse on-time, and wheel speed as mechanical parameter have been identified to be the main parameters influencing the process responses for a particular wheel and servo reference voltage.

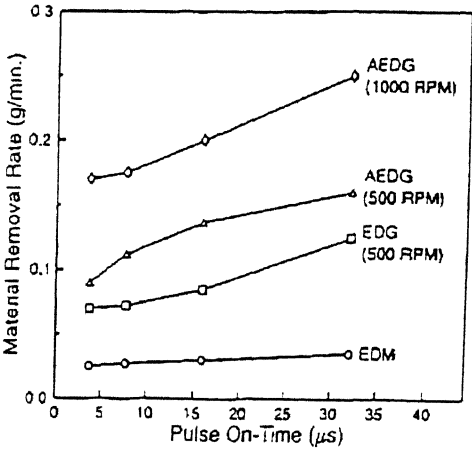
Introducing abrasion effects into the EDDG process has been observed [28] as responsible to increase in material removal rate in comparison to conventional EDM and EDG [Fig. 1.3a]. Material removal rate of the EDDG process at pulse on-time of 10 μ s and wheel speed of 500 rpm is found to be about five times greater than that of EDM and about twice of EDG in case of Al-SiC composite machining. Effect of pulse on-time on material removal rate is not significant [Fig. 1.3b] during machining of Al-SiC composite. But in case of EDG and AEDG, under the same conditions, a material removal rate is markedly increased (Fig. 1.3b). It may be an evidence of better utilization of electrical discharge energy. Similarly, higher peak current yields higher removal rate due to the intensified electro-erosion (Fig. 1.3c).

Koshy et al. [29] have found a way for removing problem of rapid wear of diamond wheel due to graphitization during grinding of ferrous materials (HSS) by using electrical discharge diamond grinding (EDDG). The role of current and wheel speed on the material removal rate, the grinding forces and power consumption have been studied to elucidate the mechanism of material removal. The trend exhibited by the MRR-wheel speed characteristics has been found to be different in different current ranges [Fig. 1.4a]. They have found that MRR initially increases with wheel speed but tends to decrease at higher end of the wheel speed at a current of zero and 1A value due to blunting of the abrasives. But the MRR increases monotonically with speed at the current of 2.5 and 5A. They have found that specific grinding energy in EDDG decreases with increase in current for any wheel speed [Fig 1.4b]. The effect of current during EDDG of cemented carbide has also been studied [30] [Fig.1.5a]. Such studies are advantageous for exploring the possibility of use of less expensive abrasives in place of costly diamond wheel.

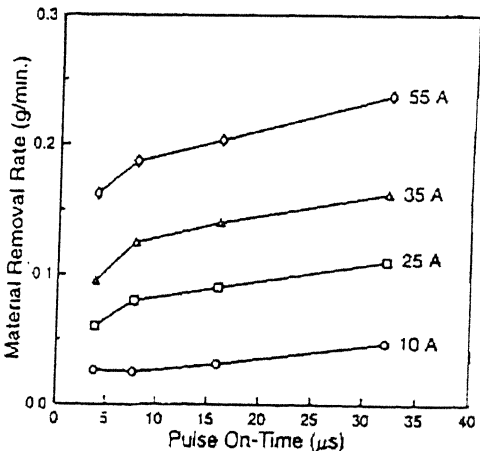
Choudhury et al. [31] have studied the effect of current on MRR and grinding forces for different voltage, pulse on-time and duty factor during EDDG of HSS. It has been observed that tangential grinding force decreases with increase in voltage and duty factor for a particular value of current [Fig. 1.5b]. They have also reported the effect of process parameters on the MRR.



(a)



(b)



(c)

Figure 1.3 (a) Effect of applied voltage on specific grinding forces (b) Effect of pulse on time on MRR for different wheel speed and (c) Effect of pulse on-time on MRR for different current, in EDDG [28]

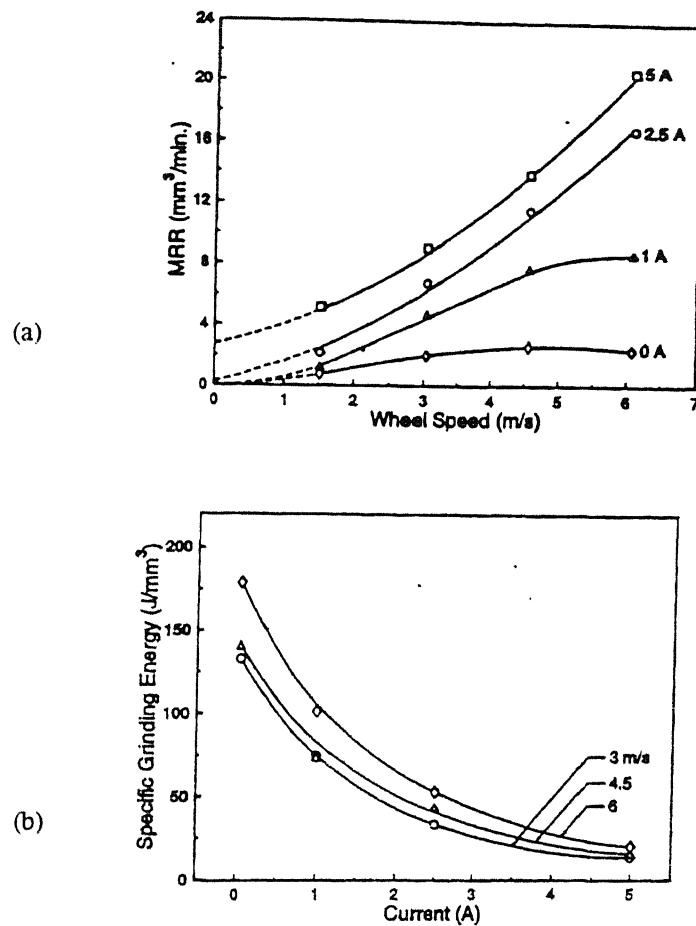


Figure 1.4 (a) Effect of wheel speed on MRR for different current (b) Effect of current on the specific grinding energy for different wheel speed during EDDG [29]

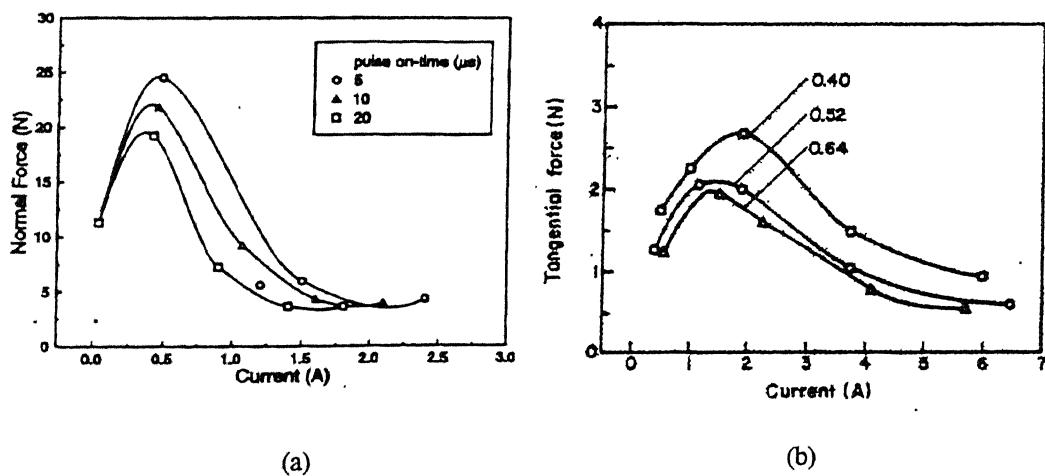


Figure 1.5 (a) Effect of current on normal force for different pulse on-time (cemented carbide workpiece) [30] (b) Effect of current on tangential force for different duty cycle (HSS workpiece) [31] during EDDG

1.5.2 Thermal modeling of Grinding

The grinding process is an important precision machining process, which requires high specific energy input in comparison to other machining processes. In any grinding process, virtually whole of the *grinding energy is converted into heat* in the grinding zone (wheel-workpiece contact) due to friction and plastic deformation. This leads to high temperatures in the workpiece which can cause undesirable effects at the ground surface such as thermal damage (burn marks and cracks), variation in hardness, and generation of residual stresses. Elevated temperatures generated in the grinding zone also have essential influence on the performance of the grinding wheel. In an attempt to avoid these effects, it is important to be able to predict workpiece temperature distributions in terms of grinding conditions, so that the process parameters can be adjusted to yield acceptable workpiece temperatures. Many researchers have intensively studied thermal modeling of grinding and many papers have been published.

Most of the thermal models developed for grinding are mainly focused on heat transfer to the workpiece with specified heat flux and with or without convection at the workpiece surface. The earlier works related to thermal model of grinding have been compiled in detailed reviews by Snoeys et al. [32], Malkin [33] and Zhang et al. [34]. Some findings related to the development of thermal modeling of grinding are listed in Table 1.3. The pioneering and widely accepted work for determining temperature field in shallow cut grinding was carried out by Jaeger [35], who presented a two-dimensional model with a band heat source of constant strength moving with a constant velocity across adiabatic semi-infinite stationary body. Most researchers up to the present day use this model with little modifications to make it more realistic.

Outwater and Shaw [36] assumed that the grinding energy is generated at the shear plane only. No consideration was given to the heat generated at the wear flat areas. Also, with cutting edges of large negative rake angles, this model under-estimate the proportion of the heat energy entering into the workpiece. In contrast, Hahn [37] pointed out that the friction forces at the wear flat areas (grain-workpiece rubbing surface) is extremely important and it is the principal heat generation source in grinding. The heat energy generated at shear plane can be neglected.

Table 1.3 Key developments in thermal modeling of Grinding

Year	Author(s)	Ref. No.	Remarks
1942	Jaeger	35	Sliding uniform rectangular heat source model. No cooling.
1952	Outwater and Shaw	36	Sliding heat source at the shear plane. No cooling
1956	Hahn	37	Sliding heat source at the grain-workpiece rubbing surface (wear flat). No cooling
1970	Des Ruisseaux and Zerkle	38	Temperature at workpiece surface which remains after grinding due to shear heat source. Jaeger's model is applied. No cooling
1970	Des Ruisseaux and Zerkle	39	Sliding uniform rectangular heat source model with uniform convective cooling
1974	Malkin	40	Temperature rise due to the frictional energy at the wear flats.
1978	Snoeys et al.	32	Various heat flux model-triangular, rectangular and parabolic
1983	Peters and Vansevenant	41	Jaeger's model supplemented with the consideration of heat loss to the chip, which is valid for creep feed and pendulum grinding.
1984	Kopalinsky	42	Temperature distribution by super imposing the two distributions (1) produced by grits which have left the contact area; (2) individual grain cutting edge with wear flats currently engaged with workpiece.
1988	Lavine	43	Convective heat transfer between the workpiece, wheel and grinding fluid, wheel and grinding fluid together is called composite solid.
1991	Lavine	44	Major part of the grinding energy is generated at wear flat area and some part is generated at the shear planes.
1994	Guo and Malkin	45	Thermal model to predict the burnout heat flux limit at a critical temp. for film boiling.
1994	Zheng and Gao	46	Thermal model for slotted / segmented wheel, Heat flux shape- triangular, rectangular and trapezoidal
1995	Jen and Lavine	47	Grinding zone temperature and heat flux distributions. Duhmal's theorem is used, No need to specify a priori the value of the fraction of grinding energy entering the workpiece or the convective heat transfer coefficient of the grinding fluid
1995	Zhang and Mahdi	48	FEM based steady state thermal model with moving heat flux of triangular profile. Convective cooling.
1995	Guo and Malkin	49	FDM based thermal model to find transient temperature distribution during cut-in, steady state and cutout.
1996	Zhang and Faghri	50	Thermal model for grinding zone heat flux and temperature distributions with or without film boiling. Integral approximation method is used.
1997	Biermann and Schneider	51	Workpiece unsteady temperature distribution, rectangular heat source and convective cooling
2000	Demetriou and Lavine	52	Coupled thermal model of the wheel grains, fluid, chips, and workpiece to predict heat flux into the workpiece and resulting temperature distribution. Duhmal's theorem is used.

The models [35-38] discussed above are used for predicting workpiece surface temperatures without considering the effect of surface cooling (dry grinding). The effect of surface cooling by the grinding fluid was analyzed by Des Ruisseaux and Zerkle [39]. They have considered constant convection coefficient over the entire top surface of the semi-infinite body. It was found that, convective cooling outside the contact region is more important than within the contact region for bulk cooling of the workpiece.

Malkin [40] assumed uniformly distributed heat flux due to frictional energy at the wear flats to find temperature rise over the workpiece surface in dry grinding. It implicitly indicated that frictional heat generated at the grain-chip interface was relatively small in comparison to wear flat area. Snoeys et al. [32] have argued that transient effects should be negligible if the workpiece speed is higher than about 50 mm/s for grinding of steel. This fact is generally true for regular grinding but not necessary for creep-feed grinding. Kopalinsky [42] has concentrated on predicting workpiece temperature distribution by superimposing the two temperature distributions, one produced by grits which have left the contact area and other produced by wear flats currently engaged with workpiece.

All the papers discussed above have assumed some value for the fraction of energy entering the workpiece. Lavine [43] eliminated the need to specify a priori the fraction of the energy entering the workpiece, by developing a model of convective heat transfer between the workpiece, wheel and grinding fluid. She has considered wheel and grinding fluid together as composite solid. However, it was assumed that all the grinding energy was generated at the wear flats rather than at the shear planes. But, she [44] modified her heat transfer model to account for the grinding energy generated at the shear plane. With this consideration, the results of conventional grinding with CBN wheels were found significant but not for Al_2O_3 wheel.

Guo and Malkin [45] found the burn-out heat flux limit at a critical temperature for film boiling during creep-feed grinding. Beyond this limit cooling becomes ineffective and temperature rises catastrophically. Zheng and Gao [46] also suggested use of slotted or segmented wheel as one of the effective ways to reduce grinding thermal damage. They developed a more general thermal model for prediction of grinding temperature for segmented or slotted wheels.

Jen and Lavine [47] developed a thermal model in down grinding using Duhamel's theorem to solve the conjugate problem of heat transfer in the workpiece, wheel grains and fluid, in order to predict the workpiece surface temperature in the grinding zone. Zhang and Mahdi [48] used finite element method to simulate surface grinding process. Temperature distribution was obtained considering triangular heat flux profile moving with uniform velocity over the workpiece top surface. Convective cooling was also taken into consideration, Guo and Malkin [49] used finite difference method to find transient temperature distribution in the workpiece during cut-in and cut out period. They have also found that the workpiece actually follows a transient behavior during the entire grinding pass for thermally short workpieces.

Zhang and Faghri [50] developed a heat transfer model to simulate the heat transfer to the workpiece, wheel, and fluid during surface grinding using integral approximation method. The grain is approximated as semi-infinite frustum of cone for finding heat transfer to the abrasive grain. This model was also used to simulate the grinding process when the boiling occurs in the grinding zone, in which the heat flux has discontinuous changes.

Biermann and Schneider [51] used Jaeger's model and finite element method to simulate the surface grinding of cemented carbides with resin bonded diamond grinding wheel. Also, the numerical results were supplemented by measurements of the grinding temperature. Recently, Demetriou and Lavin [52] developed a completely coupled model of the wheel grains, fluid chips, and workpiece with which it could be possible to predict heat flux into the workpiece, and the resulting temperature distribution.

Most of the thermal models developed as discussed above are applicable for surface grinding. References available on thermal modeling of cut-off grinding are not many.

Eshghy [53] was theoretically analyzed the thermal aspect of abrasive cut-off operation to find the temperature of cutting zone. The mathematical model developed by him consists of two interacting one-dimensional semi-infinite domains in transient conditions. The solution was obtained by Laplace transformation to find cutting zone temperature. Korolev [54] studied the temperature distribution in abrasive cut-off operation with rubber bond wheels of 2-4 mm thickness cutting 10-mm long rods of steel

at peripheral speed of 50 m/s. The mean surface temperature at the wheel-work contact layer of metal, termed as contact temperature, was measured by using thermocouples. He found that the temperature rises rapidly as the wheel penetrates the first few mm into the steel workpiece, and drops steadily as the wheel heats up causing bond softening. Korolev [54] concluded that various cutting conditions that promote self-sharpening of the wheel lowered the contact temperature.

1.5.3 Thermal Modeling of EDM

Electric discharge is a complex phenomenon of EDM process where several disciplines of science and engineering are involved in its theory. Researchers have proposed several mathematical models based on heat transfer techniques. Some key findings in the development of thermo-mathematical modeling of EDM are listed in Table 1.4 and also discussed in the following section. Melting and vaporization of material are considered to be important phenomena in predicting MRR in EDM process [55].

Van Dijk and Dutre [56] developed a thermal model based on two-dimensional transient heat conduction in a semi-infinite body subjected to a time-dependent uniform heat flux over a small circular part of its upper surface. The computational procedure for numerical calculation of crater boundary was based on the exact solution methodology. Toren et al. [57] modeled electrical erosion based on the propagation of the melting craters with evaporation. The discharge channel was considered as constant point heat source. Numerical quadrature rule was used for finding melting radius and evaporation radius. Marty [58] found that a thermal model based on a disc heat source on the surface of a semi-infinite solid with a constant heat flux is a good approximation for the spark erosion process. The crater depth was considered as a function of both the pulse duration and radius of heat source at work surface.

Erden and Kaftanoglu [59] presented a thermal model based on the uniformly-distribution-point-source assumption. In this model, the main assumption is that the electrode surface intersecting the spark channel is covered by point sources. An increase in discharge radius means that there are more point sources over the heat source area. Total energy released by these sources is equal to total spark energy. It was also reported [59] that only 10-20% of the total molten material is removed at the end of a pulse.

plasma model was also developed [67] for spark created by EDM in a liquid media. Madhu et al [68] developed a thermal model using finite element method (FEM) for determining material removal and depth of damaged layer during EDM. They assumed Gaussian heat distribution of power within a spark and updated the machined surface periodically.

Table 1.4 Key developments in thermal modeling of EDM

Year	Author(s)	Ref.	Remarks
1971	Snoeys and Van Dyck	55	Semi-infinite cylindrical workpiece, Disc heat source
1974	Van Dizck and Dutre	56	Finite or semi-infinite body, Time dependent uniform heat flux over a small circular part.
1975	Toren et al.	57	Heat conduction model with constant point heat source. Melting radius and evaporation radius is calculated.
1977	Marty	58	Constant disc heat source over a semi-infinite solid. Crater depth and radii of heat source are correlated by an universal function for given heat input and maximum surface temperature
1980	Erden and Kaftanoglu	59	Two thermal models are developed based on (1) uniformly distributed point-heat-source (2) Variations of heat source density and its radius, Agreement with experimental results are closer with second model but computational time is more.
1980	Erden and Kaftanoglu	60	Optimization of discharge energy pulse form
1980	Dharmadhikari and Sharma	61	Multi heat source model.
1982	Jilani and Pandey	62	2-D heat conduction model, Semi-infinite body, Disc heat source with constant radius
1986	Pandey and Jilani	63	Semi-infinite body, disc heat source with expanding plasma channel.
1983	Pandit and Rajurkar	64	Thermal model based on data dependent systems (stochastic empirical), Predictions are much closer to the experimental results
1989-93	DiBitonto and Co-workers	65-67	Point heat source model for (PHSM) cathode erosion. Expanding circular heat source model (ECHSM) for anode erosion. Also, a comprehensive spark model for the EDM plasma based on equations from fluid mechanics, thermodynamics and radiation. Superheating mechanism of EDM is explained.
1991	Madhu et al.	68	FEM based heat conduction model with Gaussian heat distribution of power within a spark and periodic updating of machined surface, Heat absorption owing to melting is also accounted
1996	Bhattacharya et al.	69	Model used in ref. [68] is updated by including more realistic effects such as on/-off-time and latent heat of melting and vaporization.
1997	Shankar et al.	70	An integrated approach where discharge phenomenon and temperature distribution in the electrodes have been treated together. Concave spark profile in the centre is obtained theoretically.

Further, Bhattacharya et al. [69] improved this model by accounting more realistic cases, such as on/-off-time and latent heat of melting and vaporization. An integrated approach has also been applied [70] where the discharge phenomenon and temperature distributions in the electrodes have been treated together. Spark profile across the gap in terms of the spark radius at different cross-sections has been found to be different (concave at the centre).

Survey described above show that EDDG is a complex hybrid machining process where several disciplines of science and engineering are involved in its theory. It is difficult to formulate a mathematical model, which explains the nature of the process with every detail. This thesis makes an attempt to develop a theoretical thermal analysis model of EDDG process. The scope and objectives of the present work, and the organization of the thesis are described in the following section.

1.6 Scope and objectives of the present work

Published literature available on EDDG hybrid machining process is scarce. However, the available literature reveals that the feasibility of EDDG has been experimentally tested in cut-off grinding and cut-off grinding configurations. Most previous studies of EDDG are experimental. Demands for theoretical studies have arisen because purely experimental investigation is too expensive and some times very difficult to perform. A theoretical method can simultaneously account for many principal factors, like those from mechanical, thermal and chemical effects, so that it is captured in terms of physics and mathematics.

Thermal modeling of EDDG is of major importance in order to avoid thermal residual stresses and thermal damage to the workpiece. Hence, thermal model can be developed to determine temperature distribution within the workpiece. The residual stresses in the workpiece are the best indicators of thermal and mechanical influences on the surface integrity. The residual stresses are generated in the workpiece due to plastic deformation, thermal disturbances, and phase transformation during EDDG. Hence, thermal stress model is needed to determine stress distribution within the workpiece.

The work reported in the thesis comprises analysis of temperature distribution in the workpiece for each constituent process of EDDG and also for combined process. Thermal stresses, which are induced due to each of the constituent process of EDDG,

have also been analyzed. Also, temperature distribution behaviour in the workpiece has been analyzed during EDDG when it is applied in surface grinding mode without spark to understand the nature of variation of temperature in diamond surface grinding. The findings of the thesis will be helpful in developing a comprehensive surface integrity model for EDDG.

The following are the objectives of the present work:

- To analyze thermal aspects of cut-off grinding and EDM (both are the constituent process of EDDG) using finite element method. Rectangular domain for diamond cut-off grinding and axisymmetric domain for EDM are considered for temperature analysis.
- To develop and analyze thermal model for EDDG using superposition theorem.
- To develop mathematical models for determination of components of thermal stresses in cut-off grinding and EDM both.
- To analyze the thermal aspects of Electro-discharge diamond surface grinding (EDDSG) with zero current.

1.7 Organization of the thesis

First chapter of the thesis comprises introduction of hybrid machining processes with their potential and limitations, working principle of electro-discharge diamond grinding, need of modeling of machining processes, potential of FEM, review of literature, and scope and objectives of the present work. Thermal analysis of cut-off grinding and EDM with associated results of temperature distribution only in the workpiece constitutes chapter 2 of the thesis. The results of superposition of the two temperature distributions to get temperature distribution in the combined process (EDDG) are also reported in the same chapter. Chapter 3 presents two thermal stresses models in which the first one is used for cut-off grinding and the second one is used for EDM. Thermal analysis of electro-discharge diamond surface grinding (EDDSG) with zero current is presented in chapter 4. Chapter 5 presents the main conclusions of this work and guidelines for future work.

Chapter 2

Thermal Analysis of EDDG

2.1 Introduction

Electro-discharge Diamond grinding (EDDG) integrates diamond grinding and EDM. Heat energy generated during EDDG (due to grinding and EDM both) can cause undesirable effects such as micro-cracks, generation of critical residual stresses, and metallurgical damage that may affect the surface integrity of finished components. An accurate prediction of thermal history (or transient temperature distribution) in any machined component is a prerequisite for a reliable prediction of surface integrity. But hardly any analytical/empirical/numerical study has been reported in the literature for predicting transient temperature distribution in the workpiece during EDDG process.

Modeling of such a complex process like EDDG is not possible by analytical method because of complex boundary conditions and coupling of EDM and grinding processes. EDDG process is too complicated to warrant appropriate analytical models. FEM is a versatile method that can solve a wide range of different engineering problems of complex geometry, heterogeneous materials, varying loading and different boundary conditions. In view of these flexibilities, FEM is employed for modeling of EDDG process.

Configuration of a typical EDDG process in cut-off grinding mode is shown in Fig. 2.1. Here, L is workpiece length, V_f is feed velocity, V_s is wheel speed, D is diameter of metal bonded diamond grinding wheel, B is width of workpiece and H is height of the workpiece. Two electrodes of the EDDG namely workpiece and metal bonded diamond grinding wheel are dipped in liquid dielectric (usually kerosene) as shown in Fig. 2.1. Metallic wheel bond and work surface are physically separated by a gap, magnitude of which depends on protrusion height of grains and uncut thickness as shown in Fig. 2.2.

In the present chapter an attempt has been made to determine temperature distribution in the workpiece during EDDG for metal bonded diamond wheel in cut-off grinding mode (Fig. 2.1). Finite element based codes have been developed for the simulation of temperature distribution. Separate codes have been developed for grinding

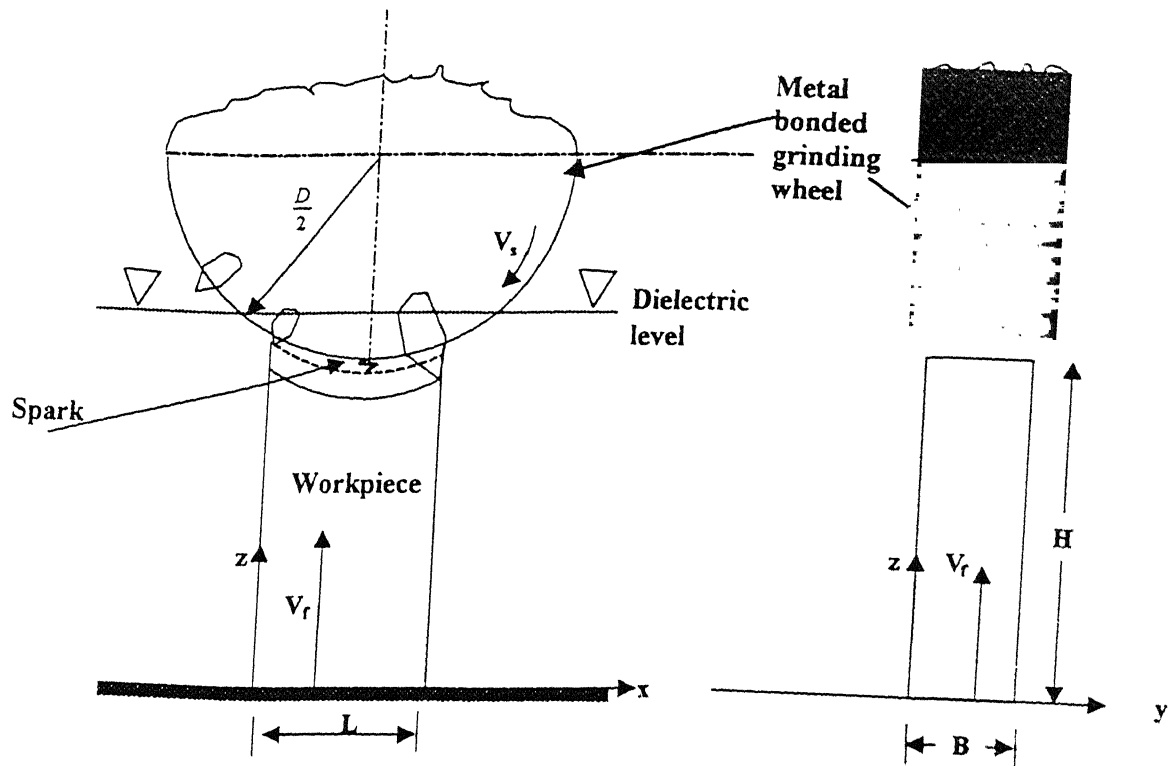


Fig. 2.1 Schematic of EDDG process in cut-off grinding mode

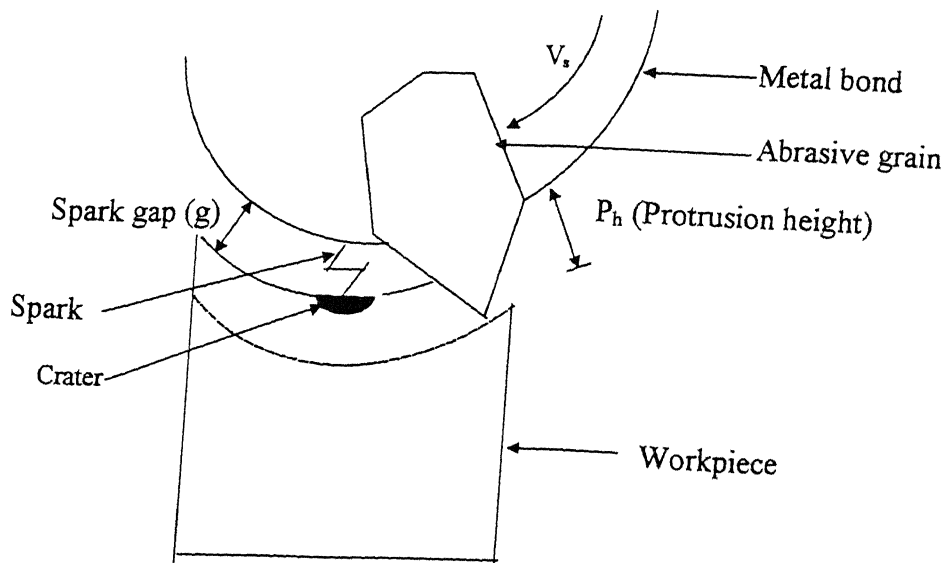


Fig. 2.2 Detailed view of the grinding process

and EDM due to the difference in the nature of the temperature distribution, i.e being 2-D for grinding and axisymmetric for EDM. The temperature distribution in whole workpiece domain due to EDDG is obtained by superposing the temperature distributions obtained from these two codes.

The workpiece is simultaneously subjected to heating due to electrical sparks generated between the bond and workpiece, and heat generated due to abrasion by abrasive grains having protrusion height more than the inter-electrode gap (Fig. 2.2). Both these phenomena (sparking and location of a grain and thereby abrasion), under actual operation, occur randomly over the top surface of the workpiece. The transient temperature distribution due to EDDG process is considered as superposition of transient temperature due to both-grinding heat source as well as EDM heat source neglecting the interaction effect between grinding and EDM. The interaction effect may be in terms of reduction in grinding forces because of temperature softening effect due to EDM and increase in material removal rate by EDM due to flushing action of grinding. The stresses developed during machining will also change if interaction effect is taken into consideration. Here, temperature distribution due to grinding is determined by considering whole domain as 2-D boundary-initial value problem whereas, temperature distribution due to sparking action is treated as axisymmetric boundary-initial value problem.

Assumptions

Due to random and complex nature of EDDG process, following assumptions are made to make the problem mathematically tractable.

1. The workpiece material is homogeneous and isotropic. Although the materials used in real practice like HSS are not homogeneous in structure however to simplify the problem it is considered to be homogeneous throughout. Hence, the average values of thermal properties are used.
2. The thermal properties, viz. specific heat and thermal conductivity, of the workpiece material are treated as temperature independent.
3. Only a fraction of grinding as well as spark energy is dissipated as heat into the workpiece. Rest of the heat is assumed to be distributed between the grinding

- wheel, chip, debris, and dielectric. However, the present study is restricted only to the analysis of temperature distribution within the workpiece.
4. The protrusion height of all the grains is equal and remains constant throughout the operation. Since the time of computational machining taken in this model is short (≈ 0.05 s) hence grain wear, fracture and change in grain spacing for this small period of machining time can be considered as negligible. While considering machining for a longer duration, grain wear and fracture are required to be considered with probabilistic approach which can account the randomness of grains as well as their behavior.
 5. Length scales of grinding and EDM domains are different. Grinding 2-D domain considered in present study is 6 mm X 20 mm whereas EDM axisymmetric domain is considered within 2 mm diameter and 1 mm depth.

The above stated assumptions 1-3 are valid for both the cut-off grinding as well as EDM where as assumption 4 is valid for cut-off grinding only. Assumption 5 is used for superposition. These five assumptions are not valid in practical cases. Since it is the first theoretical approach to model a complex hybrid process like EDDG, some assumptions are made to simplify the problem. Otherwise the problem will become complex which will be difficult to solve.

2.2 Thermal Analysis of Cut-off Grinding

In cut-off grinding operation, which is a constituent process of EDDG, it is assumed that total grinding energy is converted into heat within a small grinding zone, which leads to high temperature in the grinding zone. The heat is taken away by the workpiece, grinding wheel, dielectric, and chips. To avoid thermal damage to the workpiece, it is important to understand heat transfer in the workpiece. Here, only heat transfer to the workpiece is analyzed. Some researchers have intensively studied heat transfer in grinding experimentally as well as analytically (see section 1.5.2). Heat transfer study has been done only analytically for abrasive cut-off operation [53-54,71] to find the critical down feed (easiest one to vary) for maximum temperature for different wheel work combinations. Shaw et al. [71] found that specific energy (U_o) decreases with down feed in cut-off grinding operation.

2.2.1 Mathematical Modeling

In this section, a thermal model for the cut-off grinding is presented. Knowledge of operating temperature within the grinding wheel and the workpiece is essential to understand the cutting phenomenon involved. To find temperature distribution in the workpiece, proper modeling of heat flux profile and energy partition for workpiece-abrasive wheel combination are needed.

The **heat flux** generated during cut-off grinding is considered as a rectangular heat flux over the workpiece top surface (Fig. 2.3). Here, L and H are the length and height of the workpiece enclosed by the boundary surfaces $S1$, $S2$, $S3$, and $S4$. Its value is calculated by using following equation [72].

$$q_{wg} = R_{wg} U_o V_f \quad (2.1)$$

where, R_{wg} is energy partition due to grinding, V_f is feed given to the workpiece, and U_o is specific grinding energy.

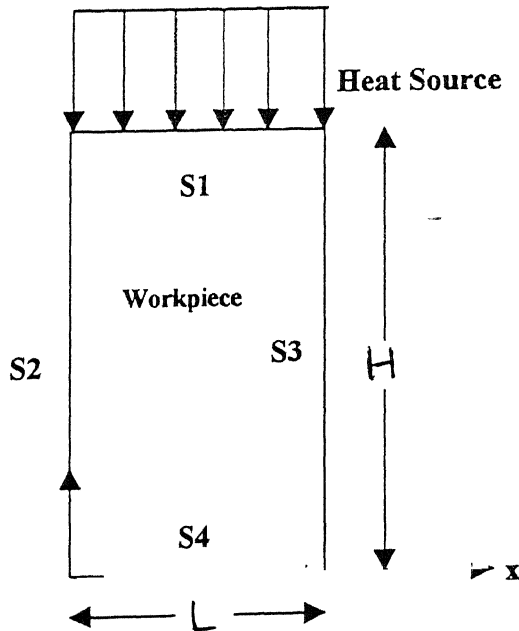


Fig 2.3 Thermal model of cut-off grinding

The effect of cutting speed (V_s) on q_{wg} is taken care of by specific grinding energy (U_o) term because they are related with each other by following equation [72].

$$U_o = \frac{F_c V_s}{MRR_v} = \frac{F_c V_s}{V_f A} \quad (2.1a)$$

Here, F_c is tangential grinding force, V_s is grinding speed related to RPM of grinding wheel, MRR_v is volumetric material removal rate and A is the area of cross-section of workpiece top surface.

Selection of energy partition (R_{wg}) value, which is defined as a ratio of the energy going to the workpiece and the total grinding energy, is of special importance in determining thermal load on the workpiece. Shaw [71] has reported that the value of R_{wg} decreases from 0.31 to 0.22 by increasing feed rate from 4.23 to 12.7 mm/s during dry cut-off grinding of AISI 1020 steel workpiece with alumina grinding wheel. It further reduces (upto 0.10) with feed if special graded alumina wheel is employed. But, information about R_{wg} for metal bonded diamond wheel in cut-off grinding of steel is nonexistent in the literature. Here, the value of R_{wg} is chosen as 0.08 for cut-off grinding of high speed steel (HSS) workpiece with metal bonded diamond wheels, which is closer to the value of R_{wg} for special graded alumina grinding wheel and AISI 1020 workpiece [71]. Further, high thermal conductivity of diamond grains and metallic bond of a diamond grinding wheel leads to slightly less energy partition (< 0.10) than used for special graded resin bonded alumina grinding wheel.

2.2.2 Finite Element Formulation

The physical phenomenon of cut-off grinding can be described by boundary-initial value problem i.e. by energy equation (which is a differential equation) and appropriate boundary and initial conditions. Solving this problem using available classical methods would be very difficult and tedious. Finite element method can be used for such complicated problem to obtain approximate solution by converting its governing equation (2.2) into set of algebraic equations.

Governing equation

Temperature field due to cut-off grinding is governed by thermal diffusion equation:

$$\rho C_s \frac{\partial T}{\partial t} = \frac{\partial}{\partial x} \left(k \frac{\partial T}{\partial x} \right) + \frac{\partial}{\partial z} \left(k \frac{\partial T}{\partial z} \right) \quad (2.2)$$

where, T is temperature, t is time, ρ is density, k is thermal conductivity, and C_s is specific heat capacity of workpiece material in solid state.

Boundary and initial conditions

Energy transferred to the workpiece as heat input serves as thermal boundary condition on the top surface $S1$ (Fig. 2.3). The bottom surface of the workpiece is assumed to be sufficiently away from the top surface so as to remain at its initial temperature throughout the grinding pass. The heat loss to the coolant on the surfaces $S1$, $S2$, and $S3$ (Fig. 2.3) is modeled using convective boundary condition. Thus, the boundary conditions are:

$$\left. \begin{aligned} q &= -k \nabla T \cdot n = -q_w + h_c T \quad \text{on } S1, S2, S3 \\ \text{where} \\ q_w &= q_{wg} + h_c T_0 \quad \text{on } S1 \\ q_w &= h_c T_0 \quad \text{on } S2, S3 \\ T &= T_0 \quad \text{on } S4 \end{aligned} \right\} \text{when } t > 0 \quad (2.3)$$

Here, h_c is convective heat transfer coefficient, T_0 is ambient temperature (i.e. dielectric temperature) and q_{wg} is heat flux supplied to the workpiece due to grinding.

The initial temperature T_i can be taken as normal room temperature T_0 of the dielectric in which workpiece is completely dipped. Thus, the initial condition becomes

$$T_i = T_0 \quad \text{at } t=0 \quad (2.4)$$

Galerkin Formulation

The Galerkin weighted residual method [73] is used to convert the governing differential equation (Eq. 2.2) into algebraic equations by using appropriate weighting

functions. When the residue is made orthogonal to the weight function, the following integral equation is obtained.

$$\int_{\Omega} \left\{ \rho C_s \frac{\partial T}{\partial t} - \left[\frac{\partial}{\partial x} \left(k \frac{\partial T}{\partial x} \right) + \frac{\partial}{\partial z} \left(k \frac{\partial T}{\partial z} \right) \right] \right\} W dx dz = 0 \quad (2.5)$$

where, W is weighting function and Ω is the domain of interest. In vector form, this can be written as

$$\int_{\Omega} \rho C_s \frac{\partial T}{\partial t} W dx dz - \int_{\Omega} [\nabla \cdot (k \nabla T)] W dx dz = 0 \quad (2.6)$$

which can be simplified to

$$\int_{\Omega} \rho C_s \frac{\partial T}{\partial t} W dx dz - \int_{\Omega} [\nabla \cdot (W k \nabla T)] dx dz + \int_{\Omega} \nabla W \cdot \nabla (k T) dx dz = 0 \quad (2.7)$$

The expression (2.7) is further simplified by using the divergence theorem, which gives rise to certain boundary terms.

$$\int_{\Omega} \rho C_s \frac{\partial T}{\partial t} W dx dz - \int_{\Gamma} W k \nabla T \cdot \hat{n} d\Gamma + \int_{\Omega} \nabla W \cdot \nabla (k T) dx dz = 0 \quad (2.8)$$

where, \hat{n} is outward normal to the boundary.

Note that $W=0$ on S_4 (the boundary on which T is specified). Using this condition as well as the boundary conditions of equation (2.3), the above expression becomes

$$I_1 + I_2 + I_3 = 0 \quad (2.9)$$

Where

$$\left. \begin{aligned} I_1 &= \int_{\Omega} \rho C_s \frac{\partial T}{\partial t} W dx dz \\ I_2 &= \int_{\Omega} \nabla W \cdot \nabla (k T) dx dz \\ I_3 &= - \int_{\Gamma} W q_w d\Gamma + \int_{\Gamma} h_c W T d\Gamma \end{aligned} \right\} \quad (2.10)$$

$$\text{Here, the boundary } \Gamma \text{ is given by } \Gamma = S_1 \cup S_2 \cup S_3 \quad (2.11)$$

Finite Element Approximation

In contrast to the traditional Galerkin weighted residual method where a global approximation is chosen for the field variable, in Galerkin finite element method the domain of interest is discretized into small elements [Fig. 2.4]. Then, the weighted residual integrals are evaluated over each element and finally the elemental expressions are assembled appropriately to get the global expressions.

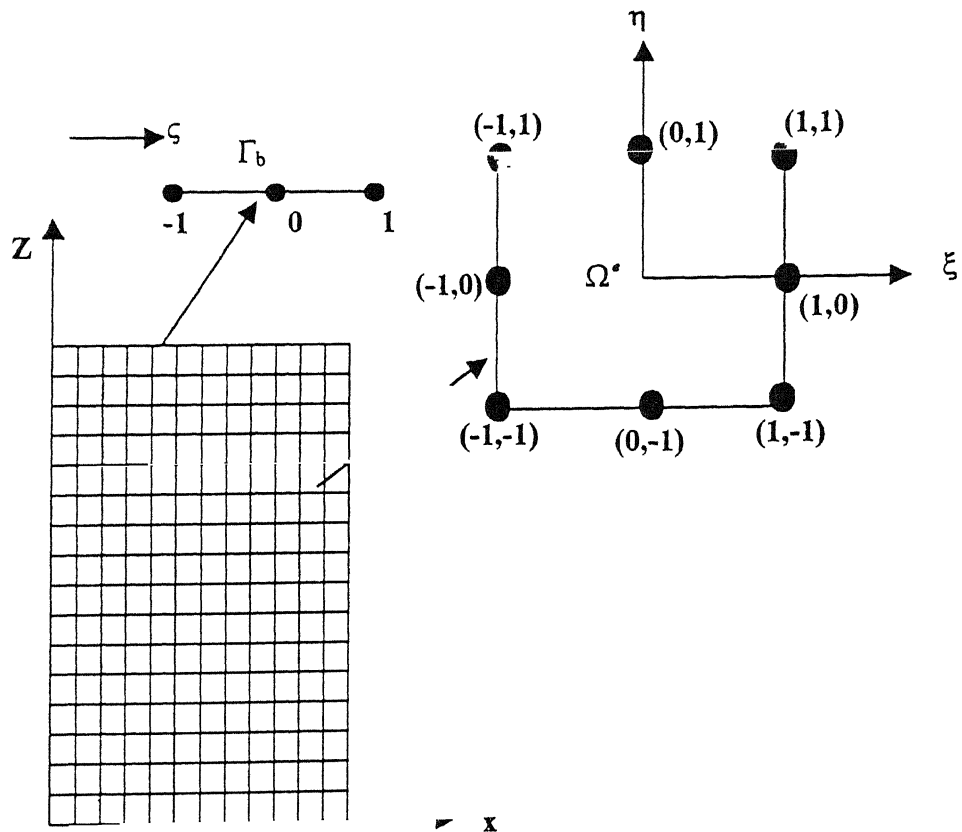


Fig 2.4 Finite element mesh of workpiece in cut-off grinding

Different types of elements (triangles, rectangles, quadrilaterals, and curved triangles) are available for discretising the domain and choosing a suitable approximation for the primary variable. While selecting the element type and the corresponding shape functions, it must be ensured that the shape functions satisfy the following two mesh convergence criteria:

- (1) completeness of the approximation in the limit of the element size approaching to zero, and
- (2) compatibility condition which states that the continuity across the interelement boundaries of the primary variable and its derivatives upto one order less than the highest order appearing in the weighted residual integral.

There are quite a few 2-D elements which satisfy the above mesh convergence criteria. Amongst them, 8-noded quadrilateral isoparametric element seems to give better results. Therefore in the present work, 8-noded quadrilateral isoparametric element is used (Fig. 2.4) [73].

To obtain the finite element equation from expression (2.10), the domain is discretized into nem number of elements [Fig. 2.4]. Further, over a typical element, the temperature is approximated using the unknown nodal values T_i^e and the known interpolation (or shape) functions N_i^e .

Thus,

$$T(x, z, t) = \sum_{i=1}^8 N_i^e(x, z) T_i^e(t) = \{N^e\}^T \{T^e\} \quad (2.12)$$

where

$$\{N^e\}^T = \{N_1^e \quad N_2^e \quad \dots \dots \dots N_8^e\} \quad (2.13 \text{ a})$$

and

$$\{T^e\}^T = \{T_1^e \quad T_2^e \quad \dots \dots \dots T_8^e\} \quad (2.13 \text{ b})$$

In Galerkin's method, the weighting functions are also expressed using the same shape functions. Therefore

$$W(x, z) = \sum_{i=1}^8 N_i^e(x, z) W_i^e = \{N^e\}^T \{W^e\} \quad (2.14)$$

$$\{\nabla T\} = \left\{ \begin{array}{c} \frac{\partial T}{\partial x} \\ \frac{\partial T}{\partial z} \end{array} \right\} = [B^e] \{T^e\} \quad (2.15)$$

where,

$$[B^e] = \begin{bmatrix} \frac{\partial N_1^e}{\partial x} & \frac{\partial N_2^e}{\partial x} & \frac{\partial N_3^e}{\partial x} & \frac{\partial N_4^e}{\partial x} & \frac{\partial N_5^e}{\partial x} & \frac{\partial N_6^e}{\partial x} & \frac{\partial N_7^e}{\partial x} & \frac{\partial N_8^e}{\partial x} \\ \frac{\partial N_1^e}{\partial z} & \frac{\partial N_2^e}{\partial z} & \frac{\partial N_3^e}{\partial z} & \frac{\partial N_4^e}{\partial z} & \frac{\partial N_5^e}{\partial z} & \frac{\partial N_6^e}{\partial z} & \frac{\partial N_7^e}{\partial z} & \frac{\partial N_8^e}{\partial z} \end{bmatrix}$$

Similarly,

$$\{\nabla W\} = [B^e] \{W^e\} \quad (2.16)$$

Further,

$$\frac{\partial T}{\partial t} = \{N^e\}^T \left\{ \dot{T}^e \right\} \quad (2.17)$$

In the present work, the geometry of the workpiece is also approximated by the same shape functions:

$$x = \{N^e\}^T \{x^e\} \quad , \quad z = \{N^e\}^T \{z^e\} \quad (2.18)$$

The vectors $\{x^e\}$ and $\{z^e\}$ contain the nodal values of x and z coordinates respectively.

To express the boundary terms in terms of the nodal quantities, approximation over the boundary is needed. Note that, as the domain is divided into *nem* number of area elements, the boundary automatically gets divided into *nbe* number of line elements. The approximation for T, W, and q_w over a typical boundary element can be written as:

$$T = \{N^b\}^T \{T^b\} = \{N_1^b \quad N_2^b \quad N_3^b\} \begin{Bmatrix} T_1^b \\ T_2^b \\ T_3^b \end{Bmatrix} \quad (2.19)$$

$$W = \{N^b\}^T \{W^b\} = \{N_1^b \quad N_2^b \quad N_3^b\} \begin{Bmatrix} W_1^b \\ W_2^b \\ W_3^b \end{Bmatrix} \quad (2.20)$$

$$q_w = \{N^b\}^T \{q_w^b\} = \{N_1^b \quad N_2^b \quad N_3^b\} \begin{Bmatrix} q_{w1}^b \\ q_{w2}^b \\ q_{w3}^b \end{Bmatrix} \quad (2.21)$$

Note that the vector $\{N^b\}$ contains 1-D quadratic shape functions, which are consistent with the 2-D shape functions N_i^e .

Finite Element Equations

Substituting expressions (2.15-2.17) and (2.19-2.21), the integrals I_1, I_2, I_3 can be written as:

$$I_1 = \sum_{e=1}^{nem} \{W^e\}^T \left(\int_{\Omega^e} \rho C_s \{N^e\} \{N^e\}^T dx dz \right) \{T^e\}^* \quad (2.22)$$

$$I_2 = \sum_{e=1}^{nem} \{W^e\}^T \left(\int_{\Omega^e} k [B^e]^T [B^e] dx dz \right) \{T^e\} \quad (2.23)$$

$$I_3 = \sum_{b=1}^{nbe} -\{W^b\}^T \left(\int_{\Gamma_b} \{N^b\} \{N^b\}^T d\Gamma_b \{q_w^b\} \right) + \{W^b\}^T \left(\int_{\Gamma_b} h_c \{N^b\} \{N^b\}^T d\Gamma_b \right) \{T\}^b \quad (2.24)$$

Here, Ω^e is the domain of typical area element while Γ_b is the domain of typical boundary element (Fig. 2.4).

Then, the expression (2.9) becomes

$$\sum_{e=1}^{nem} \{W^e\}^T [GC^e] \{T^e\}^* + \sum_{e=1}^{nem} \{W^e\}^T [GK^e] \{T^e\} - \sum_{b=1}^{nbe} \{W^b\}^T \{Gf^b\} + \sum_{b=1}^{nbe} \{W^b\}^T [GK^b] \{T\}^b = 0 \quad (2.25)$$

where,

$$\left. \begin{aligned} [GC^e] &= \int_{\Omega^e} \rho C_s \{N^e\} \{N^e\}^T dx dz \\ [GK^e] &= \int_{\Omega^e} k [B^e]^T [B^e] dx dz \\ [GK^b] &= \int_{\Gamma_b} h_c \{N^b\} \{N^b\}^T d\Gamma \\ \{Gf^b\} &= \int_{\Gamma_b} \{N^b\} \{N^b\}^T \{q_{wg}^b\} d\Gamma \end{aligned} \right\} \quad (2.26)$$

Here, $[GC^e]$ is elemental capacitance matrix, $[GK^e]$ is element conductivity matrix, $[GK^b]$ is boundary conductivity matrix, and $\{Gf^b\}$ is boundary flux vector.

For the purpose of numerical evaluation of the integrals, the area integrals (over Ω^e) are transformed to the natural coordinate (ξ, η) using the following transformation:

$$\int_{\Omega^e} (\dots) dx dz = \int_{-1}^1 \int_{-1}^1 (\dots) |J| d\xi d\eta \quad (2.27)$$

where, $|J|$ is the determinant of the Jacobian matrix of transformation

$$[J] = \begin{bmatrix} \frac{\partial x}{\partial \xi} & \frac{\partial x}{\partial \eta} \\ \frac{\partial z}{\partial \xi} & \frac{\partial z}{\partial \eta} \end{bmatrix} \quad (2.28)$$

The matrix $[J]$ is evaluated using the transformation Eq. (2.18). The integrands of the integrals (2.26) also need to be expressed in terms of the natural coordinates ξ and η . The choice of the natural coordinate system is dictated by the Gauss quadrature rule [73] used in the numerical evaluation of integrals over the element.

Similarly the boundary integrals (over Γ_b) are transformed to the natural coordinate ς using the transformation:

$$\int_{\Gamma} (\dots) d\Gamma = \int_{-1}^1 (\dots) |J_b| d\varsigma \quad (2.29)$$

where, $|J_b|$ is the Jacobian for the boundary element and is given by

$$|J_b| = \sqrt{\left(\frac{\partial z}{\partial \varsigma}\right)^2 + \left(\frac{\partial x}{\partial \varsigma}\right)^2} \quad (2.30)$$

Gauss-Legendre numerical integration scheme is used in evaluating the area as well as boundary integrals (2.26). The formula for area integral is

$$\int_{-1}^1 \int_{-1}^1 f(\xi, \eta) d\xi d\eta = \sum_{i=1}^{n_\xi} \sum_{j=1}^{n_\eta} w_i w_j f(\xi_i, \eta_j) \quad (2.31)$$

while, that for the boundary integral is

$$\int_{-1}^1 f(\varsigma) d\varsigma = \sum_{i=1}^{n_\varsigma} W_i f(\varsigma_i) \quad (2.32)$$

Here, n_ξ , n_η and n_ς denote the number of Gauss points in ξ , η and ς directions respectively. Further, w_i and w_j denote the weights, and ξ_i , η_j and ς_i denote the Gauss point coordinates.

All the elemental matrices are evaluated using 3×3 Gauss quadrature for reasonably accurate evaluation of the integrals. Similarly, the elemental boundary integrals are evaluated using 3 point Gauss quadrature [73].

The final global element equations are obtained by assembling the elemental equations (2.26) at appropriate locations. The assembled finite element equation can be written as:

$$[GGC] \left\{ \dot{T} \right\} + [GGK] \{T\} = \{GGF\} \quad (2.33)$$

Where $[GGC]$ is global capacitance matrix due to grinding, $[GGK]$ is global conductivity matrix due to grinding, $\{GGF\}$ is global heat flux due to grinding, $\{T\}$ is global temperature vector and $\left\{ \dot{T} \right\}$ is time derivative of $\{T\}$.

Equations (2.33) represent a set of ordinary differential equations in the variable T as function of time t . These equations are solved after application of implicit Finite Difference Method (FDM) discussed in subsequent section.

Finite Difference Scheme

The θ family finite difference approximation for the time derivative $\left\{ \dot{T} \right\}$ is used to convert the set of differential equations (2.33) into a set of algebraic equations:

$$\theta \left\{ \dot{T} \right\}_{i+1} + (1-\theta) \left\{ \dot{T} \right\}_i = \frac{1}{\Delta t_{i+1}} (\{T\}_{i+1} - \{T\}_i) \quad 0 \leq \theta \leq 1 \quad (2.34)$$

where, $\{T\}_i$ and $\left\{ \dot{T} \right\}_{i+1}$ are the temperature at step (i) and step (i+1),

$\left\{ \dot{T} \right\}_i$ and $\left\{ \dot{T} \right\}_{i+1}$ are the derivatives of temperature with time at step (i) and step

(i+1), and Δt_{i+1} is the time interval of step (i+1).

The resulting algebraic equations are:

$$[A]_{i+1} \{T\}_{i+1} = \{B\}_{i,i+1} \quad i = 0, 1, 2, 3, \dots, n \quad (2.35)$$

where,

$$[A]_{i+1} = [C] + \theta \Delta t_{i+1} [K] \quad (2.36)$$

$$\{B\}_{i,i+1} = \Delta t_{i+1} (\theta \{F\}_{i+1} + (1-\theta) \{F\}_i) + ([C] - (1-\theta) \Delta t_{i+1} [K]) \{T\}_i \quad (2.37)$$

In the present case, the value of θ is chosen to be $2/3$ (Galerkin scheme). In each time interval Δt , the nodal temperatures at the new time level are calculated by using the

set of simultaneous algebraic equations (2.35). The solution thus marches in time, in steps of Δt until the desired final time is reached. In grinding, Δt is selected as time required to move down exactly by one element length of the grinding domain.

2.2.3 Results and Discussion

The temperature distribution on the top surface and along the depth are determined using FEM model and compared with the previously obtained experimental results [71] for the same machining parameters and material properties (table 2.1 and 2.2). However, the feed value has been changed to 3.2 mm/s from 3.38 mm/s for some computational convenience. Rectangular heat flux is assumed to be distributed over all elements of the top surface and it moves downward exactly by one element after every time step. Convergence study has revealed that the mesh of (19) X (22) isoparametric eight noded quadrilateral elements with 1337 nodes are adequate for this problem.

Figures 2.5 show the temperature variation along depth as well as top surface temperature variation in dry cut-off operation at different grinding times. Figure 2.5a shows an agreement between the experimental and computed results obtained for different grinding times. The discrepancy between the computed and experimental results could be assigned to the difference in the feed value used (3.2 mm/s in place of 3.38 mm/s used in reference [71]) and unknown grinding time for which experimental results

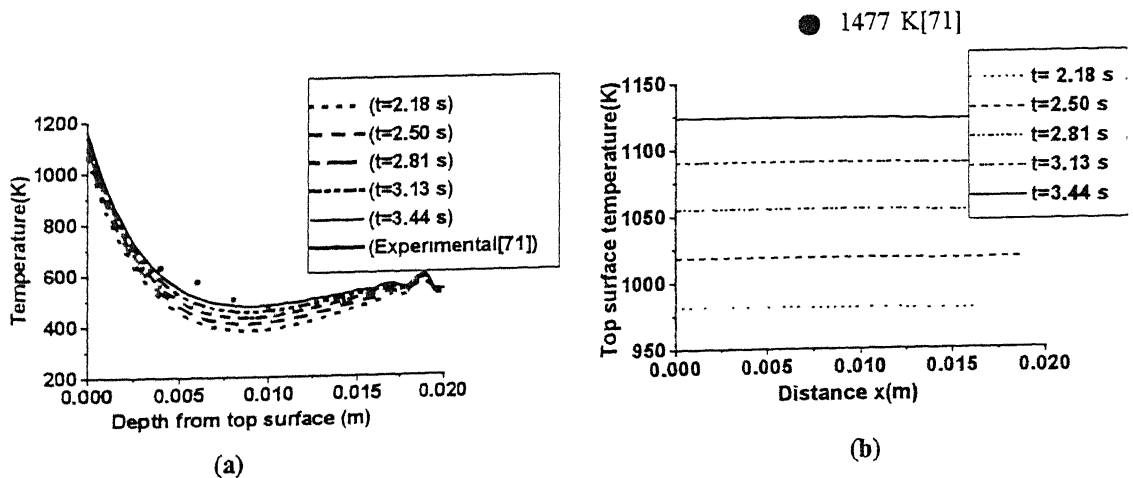


Fig. 2.5 Temperature variations with time during dry cut-off operation (a) depthwise, (b) at the top surface, for $U_s=13.58$ GPa and $R_{wg}=0.31$ at $V_f=3.2$ mm/s

are reported. The workpiece top surface temperature was extrapolated using measured temperature at different depths below the top surface. The extrapolated top surface temperature is 1477 K for $V_f=3.38$ mm/s. Using the present model, top surface temperature in similar conditions is determined as 1124 K for $V_f = 3.2$ mm/s (Fig. 2.5b).

The results for depthwise temperature variation are also compared at higher feed of 9.35 mm/s (Fig. 2.6). Here, results (Fig. 2.6a) are in close agreement if specific grinding energy U_o of work material and energy partition R_{wg} are considered feed dependent [71]. The values of U_o and R_{wg} for various feed rates are given in table 2.2. Theoretically calculated temperature values are higher as compared to the experimental values [71] if U_o and R_{wg} are considered feed independent (Fig. 2.6b). The top surface temperature in similar conditions is 1440 K (Fig. 2.6a where depth = 0) against the extrapolated value of 1144 K [71] if U_o and R_{wg} are considered feed independent. By choosing feed dependent U_o and R_{wg} (table 2.2), top surface temperature is obtained as 855 K (Fig. 2.6b). One of the reasons for these discrepancies in the values of top surface temperature may be unknown time for which actual experiments were conducted.

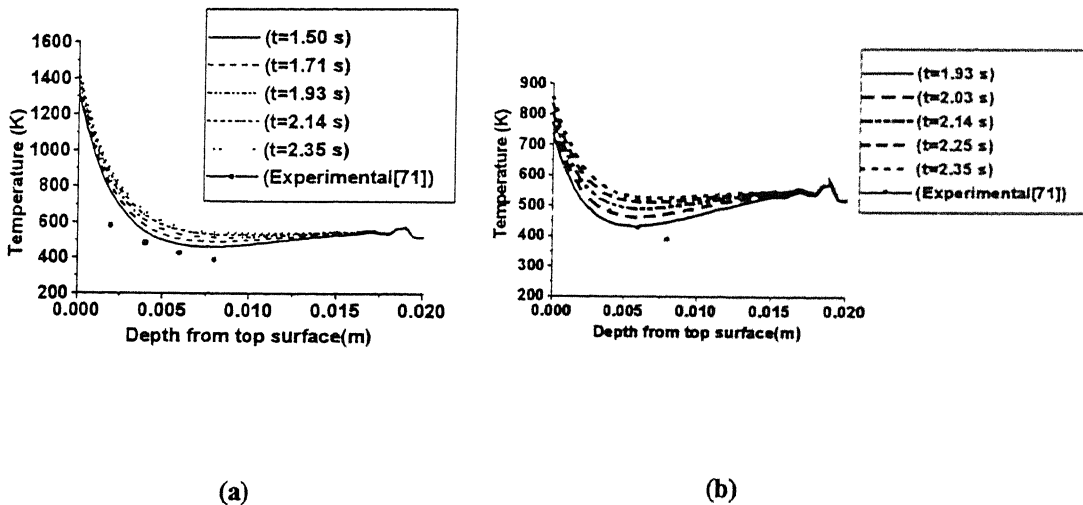


Fig 2.6 Depthwise temperature Variations with time during dry cut-off operation at $V_f = 9.35$ mm/s
 (a) $R_{wg} = 0.27$ and $U_o = 6.2$ GPa (b) $R_{wg} = 0.31$ and $U_o = 13.58$ GPa

From above comparison it is evident that accurate prediction of temperature can be made if accurate values of U_0 and R_{wg} are known in advance.

Figures 2.5 and 2.6 show that as one moves down from the top surface the temperature decreases, reaches a minimum value, and then increases. This phenomenon is observed because of higher thermal front speed than the rate of down feed into the workpiece and consideration of bottom surface always at room temperature.

Temperature distribution

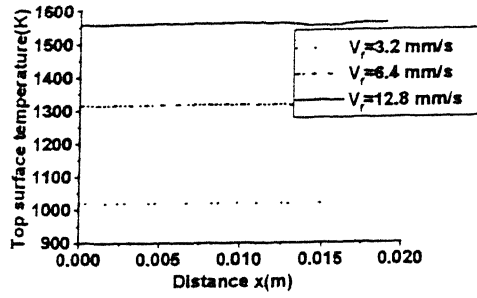
Effects of different feeds, energy partitions, specific energy, different dielectrics (as coolant) and diamond grinding wheel on temperature distribution are discussed below.

Feed

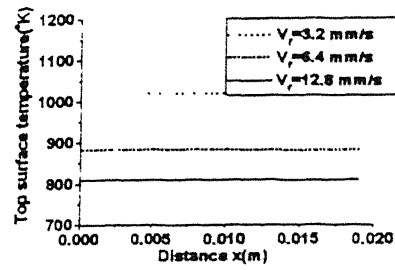
Figure. 2.7 shows the calculated top surface temperature distribution obtained at different feeds. Here, it is observed that the temperatures are higher at higher feeds if U_0 and R_{wg} are considered feed independent (Fig. 2.7a). In similar conditions top surface temperatures are lower (Fig. 2.7b) at higher feeds if U_0 and R_{wg} are considered feed dependent (table 2.2) because U_0 and R_{wg} both decrease with increase in V_f for the constant heat flux (Eq. 2.1).

Fig 2.8 shows the depthwise change in temperature. It is also observed that when R_{wg} and U_0 are taken feed independent then the temperature gradient are higher for higher feed (Fig. 2.8a). But, trend becomes reverse if feed dependent values of R_{wg} and U_0 are considered (Fig. 2.8b).

Further, accurate prediction of temperature is possible only when sufficient data are available for variation of U_0 and R_{wg} with different feeds for different grinding wheel and workpiece combination. At higher feed, initially a high temperature is generated due to higher values of U_0 , R_{wg} , and V_f (Eq. 2.1) but after some grinding time U_0 and R_{wg} start to decrease due to temperature softening effect

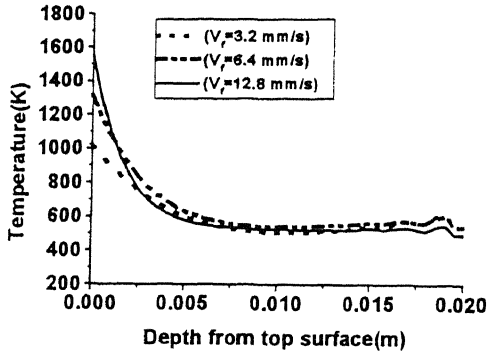


(a)

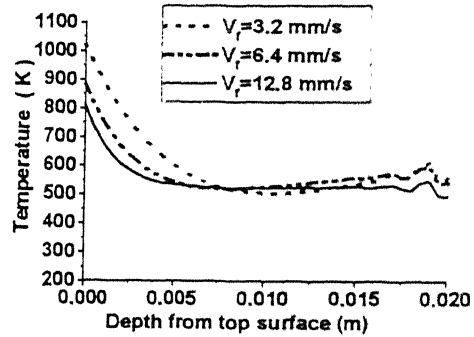


(b)

Fig 2.7 Top surface temperature variations during dry cut-off operation using Al_2O_3 grinding wheel for different feed rates after 2.5 s of grinding (a) $U_o = 13.58$ GPa and $R_{wg} = 0.31$, (b) U_o and R_{wg} are feed dependent and selected from table 2.2.



(a)



(b)

Fig 2.8 Depthwise temperature variations during dry cut-off operation using Al_2O_3 grinding wheel for different V_r after 2.5 s of grinding (a) $U_o = 13.58$ and $R_{wg} = 0.31$, (b) U_o and R_{wg} are feed dependent and selected from table 2.2.

Energy Partition

Figure. 2.9 shows the temperature distribution obtained at different energy partition values. Here, it is observed that the temperatures are higher at higher R_{wg} because of higher heat flux supplied to the workpiece which is calculated by using Eq. 2.1.

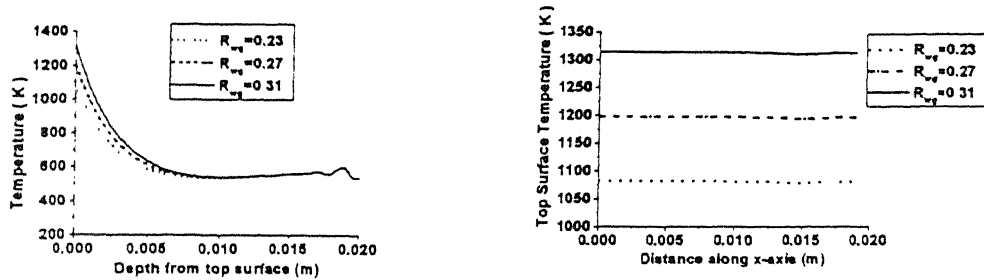


Fig 2.9 Temperature variations during dry cut-off grinding using alumina wheel for different R_{wg} at $U_o = 13.58$ GPa and $V_f = 6.4$ mm/s after 2.5 s of grinding (a) along depth (b) top surface.

Specific Energy

Figure. 2.10 shows the temperature distribution obtained at different specific energy values. Here, it is observed that temperatures are higher at higher U_o because of higher heat flux supplied to the workpiece, which is calculated by using Eq. 2.1.

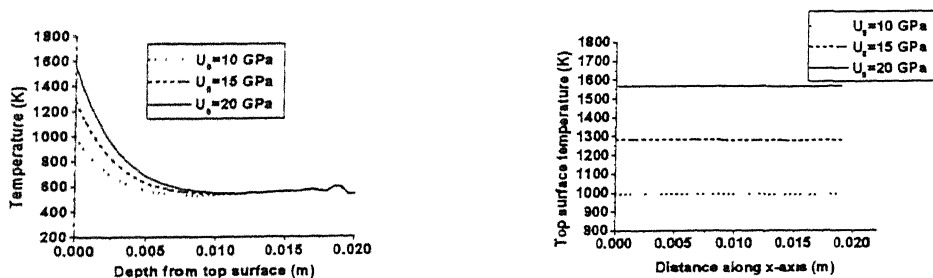


Fig 2.10 Temperature variations during dry cut-off grinding using alumina wheel for different U_o at $R_{wg} = 0.27$ and $V_f = 6.4$ mm/s after 2.5 s of grinding (a) along depth, (b) top surface.

Dielectrics

Figure 2.11 shows the effect of different dielectrics on top surface temperature variations with alumina wheel at $V_f=4.0$ mm/s after 2.5 s of grinding. The data related to the workpiece are taken from table 2.1. The top surface temperature drops to half of its value when a coolant having cooling capacity of $25000 \text{ W/m}^2\text{K}$ is used in place of dry grinding. Curvature in top surface temperature plot is observed at two ends due to convection at surfaces S2 and S3 (Fig. 2.3).

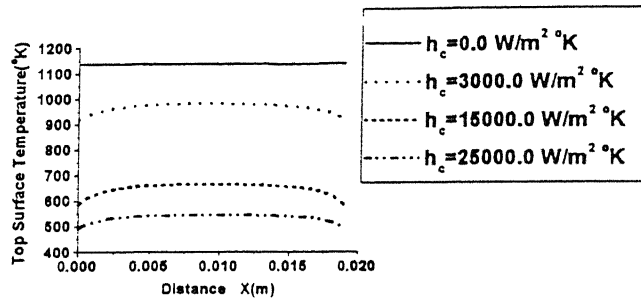


Fig 2.11 Variation of top surface temperature during cut-off grinding using alumina wheel for different h_c at $V_f=4.0$ mm/s, $U_o=13.58$ GPa, and $R_{wg}=0.31$ after 2.5s of grinding

Diamond wheel

Figure 2.12a depicts the variation of top surface temperature with time during diamond cut-off grinding of HSS workpiece. Coolant is also applied during the process. The material property data are given in table 2.3. The temperature is found to be lower with diamond wheel in comparison to alumina wheel (Fig. 2.12b) because of lower value of R_{wg} (0.08) used for the case of diamond cut-off grinding. Further thermal diffusivity of diamond is much higher (due to higher thermal conductivity) and hence major portion of heat generated during grinding is taken away by the grinding wheel. No information is available in literature for actual value of R_{wg} during diamond cut-off grinding. The value of R_{wg} varies from 0.08 to 0.18 with different feed rates if special graded alumina abrasives are used for cut-off grinding of AISI 1020 steel workpiece [71]. The value of R_{wg} for grinding of HSS with diamond wheel has been assumed to be approximately equal to the value of R_{wg} for grinding of AISI 1020 steel with special graded alumina

wheel. Wheel clogging is neglected but in actual conditions this is a major problem in diamond grinding of steel.

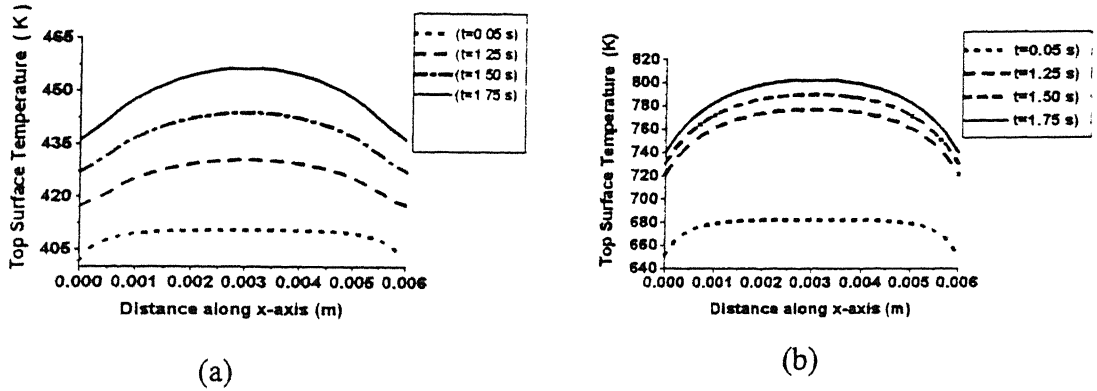


Fig 2.12 Variation of top surface temperature with time during cut-off grinding using (a) diamond wheel, (b) alumina wheel at $V_f = 10.29$ mm/s, $U_o = 10.55$ GPa, and $h_c = 10000.0$ W/m²K (kerosene)

2.3 Thermal Analysis of EDM

EDM is another constituent process of EDDG, which is basically a thermal process. Large literature is available regarding thermo-mathematical modeling of EDM process, which is summarized in section 1.5.3. Here, the following aspects of EDM are discussed first: spark radius at workpiece-flux contact surface, quantitative value of flux, energy partition of flux, and latent heat consideration for phase change.

2.3.1 Mathematical Modeling

Spark radius (R)

It is found that electrode material influences the discharge channel diameter during EDM. However, quantification/measurement of spark radius are extremely difficult due to very high pulse frequencies. Erden [74] suggested an empirical relationship to evaluate radius of a spark for the selected pairs of electrodes and dielectric. For a rectangular pulse, the spark radius $R(t)$ as a function of time (t) is written as:

$$R(t) = KQ^m t^n \quad (2.38)$$

where Q is discharge power, and m , n and K are empirical constants. These constants are defined in terms of experimental coefficients L , M and N determined experimentally for different electrode materials:

$$K = \frac{L}{lM + 0.5N}, \quad m = 0.5N, \quad n = N \quad (l \text{ is discharge length}) \quad (2.39)$$

Snoeys and Van Dijck [55] varied heat source diameter and studied its effects on various responses. Shankar et al. [70] have found noncylindrical spark shape with different radii at different cross sections across the spark length based on their integrated model wherein temperature distributions in the electrodes and dielectric are analyzed together. Pandey and Jilani [62] have proposed the following model for calculation of discharge radius R:

$$T_b = \frac{E_o R}{k \pi^{0.5}} \tan^{-1} \left[\frac{4\alpha t}{R^2} \right]^{0.5} \quad (2.40)$$

where, T_b is boiling temperature, E_o is energy density, α is thermal diffusivity, t is the time at which spark radius is calculated, and k is thermal conductivity of workpiece material. But, the application of this expression is limited, as it is valid only for a few cases of selected electrode pairs and dielectric. Literature survey indicates that although importance of spark radius during EDM process has been acknowledged, there is a scarcity of comprehensive work on the evaluation of its shape and size. In the present work the radius of a spark is calculated based on the results of reference [70].

Heat flux due to a single spark

Most researchers [63,74,75] have considered uniform disc heat source distribution within a spark. This assumption is far from reality. This fact is evidenced from the actual shape of a crater formed during EDM. In the present work, a Gaussian heat flux distribution (Appendix A) is assumed. The heat flux $q_{ws}(r)$ at a radius (r) can be calculated if maximum intensity q_o at the axis of the spark and its radius (R) are known.

$$q_{ws}(r) = q_o \exp \left\{ -4.5 \left(\frac{r}{R} \right)^2 \right\} \quad (2.41)$$

If it is assumed that total energy of each pulse is to be used only by one spark, then the above equation can be written as follows (Appendix -A):

$$q_{ws}(r) = \frac{4.45 R_{ws} U_b I}{\pi R^2} \exp \left\{ -4.5 \left(\frac{r}{R} \right)^2 \right\} \quad (2.42)$$

where U_b is breakdown (discharge) voltage, I is current and R_{ws} is the energy partition (fraction of input heat going into the workpiece) due to EDM.

Energy partition (R_{ws}) in EDM

Another important parameter required for computational analysis of EDM process is heat distribution between cathode, anode, and dielectric (neglecting radiation). The material properties of individual electrodes determine the fraction of input heat going into the electrodes. Theoretically, steel anode gets lower share of the input power than copper due to its lower thermal diffusivity.

Researchers [65-67] assumed that different fraction of the total discharge power ($= U_b I$) is lost to cathode (18%), anode (8%) and dielectric (remaining 74 %). The fraction that goes to cathode and anode is independent of current and pulse-time (t_p). The validity of this assumption was verified by DiBitonto et al. [65] by showing the agreement between theoretical and experimental optimum pulse times with same erosion rate. Shankar et al. [70] have theoretically calculated that about 40-45 % of the heat input is absorbed by the workpiece made of 5 Cr die steel. They have calculated this value using water as dielectric and copper as tool electrode. But nobody has given a comprehensive way to calculate theoretically or determine experimentally the value of R_{ws} during EDM process. In the present work, R_{ws} is taken as 0.08.

Latent heat for phase change

The latent heat required for phase change is accounted for by modifying the expression for specific heat of workpiece (C_s). Considering the enthalpy before and after phase change, latent heat of melting (L_m) and latent heat of evaporation (L_v) are incorporated into modified specific heats C_l and C_v in the vicinity of melting temperature T_m and boiling temperature T_v , respectively [69]:

$$C_l = C_s + \frac{L_m}{2\Delta T} \quad \text{for } T_m - \Delta T \leq T \leq T_m + \Delta T \quad (2.43)$$

$$C_v = C_l + \frac{L_v}{2\Delta T} \quad \text{for } T_v - \Delta T \leq T \leq T_v + \Delta T \quad (2.44)$$

where C_l and C_v are specific heats of workpiece material in liquid and vapor states, respectively.

2.3.2 Finite Element Formulation

Governing equation

Heating of workpiece due to a single spark (Gaussian distributed) is assumed to be axisymmetric, i.e. $\frac{\partial T}{\partial \theta} = 0$. Therefore, temperature field is governed by thermal diffusion

differential equation

$$\rho C_s \frac{\partial T}{\partial t} = \frac{1}{r} \frac{\partial}{\partial r} \left(k \frac{\partial T}{\partial r} \right) + \frac{\partial}{\partial z} \left(k \frac{\partial T}{\partial z} \right) \quad (2.45)$$

where, r and z are coordinate axes (Fig. 2.13).

Boundary and initial conditions

A small cylindrical portion of the workpiece around a spark is used as the domain. Energy transferred to the workpiece as heat input serves as thermal boundary condition on the top surface Γ_1 (Fig. 2.13). Heat loss to the coolant on the surface Γ_1 is modeled using the convective boundary condition. Further, the boundaries Γ_2 and Γ_3 are at such a large distance that there is no heat transfer across Γ_2 and Γ_3 (Fig. 2.13). Similarly, there is no heat transfer across the axis of axisymmetry i.e. across Γ_4 (Fig. 2.13).

The heat transfer across any boundary is given by

$$q = -\nabla T \cdot \hat{n} = -q_w + hT$$

where,

$$\left. \begin{aligned} q_w &= -q_{ws} \quad \text{for } r \leq R \\ &= h_c T_o \quad \text{for } r \geq R \\ &= 0 \quad \text{for off-time} \end{aligned} \right\} \quad \text{for } t > 0 \quad \text{on } \Gamma_1 \quad (2.46)$$

$$\left. \begin{aligned} h &= 0 \quad \text{for } r \leq R \\ &= -h_c \quad \text{for } r \geq R \\ &= 0 \quad \text{for off-time} \end{aligned} \right\}$$

$$q = 0 \quad \text{on } \Gamma_2, \Gamma_3 \text{ and } \Gamma_4 \quad (r = 0) \quad (2.47)$$

Here, q_{ws} is quantity of heat flux entering into the workpiece, R is radius of spark, R_{ws} is discharge energy partition fraction and n is normal to the surface.

The initial temperature T_i can be taken as temperature of the dielectric in which workpiece is completely dipped.

$$T_i = T_o \quad \text{at } t=0 \quad (2.48)$$

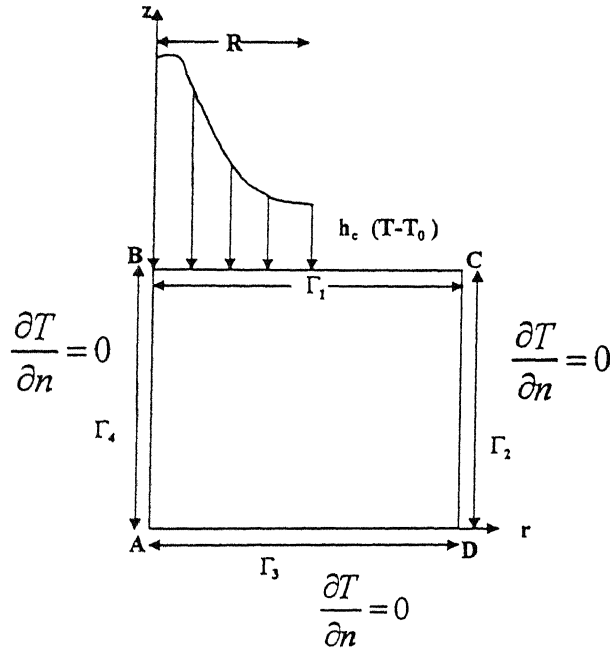


Fig 2.13 Thermal model of EDM

Galerkin formulation

Here also, Galerkin weighted residual method [73] is used to convert the governing differential equation into algebraic equations by using approximate weighting functions. When the residue is made orthogonal to weight functions, the following integral equation is obtained:

$$\int_{\Omega} \rho C_s \frac{\partial T}{\partial t} W 2 \pi r dr dz - \int_{\Omega} \left[\frac{1}{r} \frac{\partial}{\partial r} (r k \frac{\partial T}{\partial r}) + \frac{\partial}{\partial z} \left(k \frac{\partial T}{\partial z} \right) \right] W 2 \pi r dr dz = 0 \quad (2.49)$$

The expression (2.49) is simplified using divergence theorem, which gives rise to certain boundary terms:

$$\int_{\Omega} \rho C_s W \frac{\partial T}{\partial t} r dr dz + \int_{\Omega} \left[\frac{\partial W}{\partial r} k \frac{\partial T}{\partial r} + \frac{\partial W}{\partial z} k \frac{\partial T}{\partial z} \right] r dr dz - \int_{\Gamma_b} r W \nabla T \cdot \hat{n} d\Gamma = 0 \quad (2.50)$$

Using the boundary conditions (2.46), the above expression (2.50) becomes

$$I_1 + I_2 + I_3 = 0 \quad (2.51)$$

where

$$\left. \begin{aligned} I_1 &= \int_{\Omega} \rho C_s W \frac{\partial T}{\partial t} r dr dz \\ I_2 &= \int_{\Omega} \left[\frac{\partial W}{\partial r} \cdot k \cdot \frac{\partial T}{\partial r} + \frac{\partial W}{\partial z} \cdot k \cdot \frac{\partial T}{\partial z} \right] r dr dz \\ I_3 &= - \int_{\Gamma_1} W q_w r d\Gamma + \int_{\Gamma_1} h T W r d\Gamma \end{aligned} \right\} \quad (2.52)$$

Finite element approximation

To obtain the finite element equation from expression (2.52), the domain is discretized into nem number of elements (Fig. 2.14). Further, over a typical element, the temperature is approximated using the unknown nodal values T_i^e and the known interpolation (or shape) functions N_i^e . In the present work, 8-noded quadrilateral isoparametric element is used (Fig. 2.14).

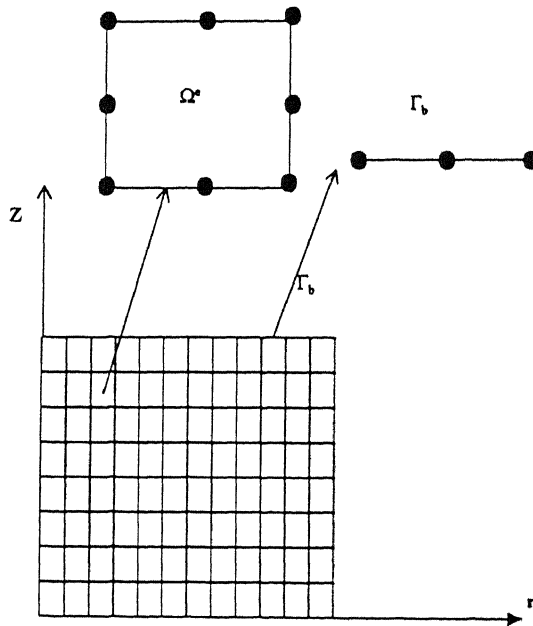


Fig 2.14 Finite element mesh in EDM domain

Thus, over a typical element

$$T(r, z, t) = \sum_{i=1}^8 N_i^e(r, z) T_i^e(t) = \{N^e\}^T \{T^e\} \quad (2.53)$$

where

$$\{N^e\}^T = \{N_1^e \quad N_2^e \quad N_3^e \quad \dots \quad N_8^e\} \quad (2.54)$$

For Galerkin's method:

$$W(r, z) = \sum_{i=1}^8 N_i^e(r, z) W_i^e = \{N^e\}^T \{W^e\} = \{W^e\}^T \{N^e\} \quad (2.55)$$

Then, the expression for derivatives of W and T becomes:

$$\begin{Bmatrix} \frac{\partial W}{\partial r} \\ \frac{\partial W}{\partial z} \end{Bmatrix} = \begin{bmatrix} \frac{\partial N_1^e}{\partial r} & - & - & - & \frac{\partial N_8^e}{\partial r} \\ \frac{\partial N_1^e}{\partial z} & - & - & - & \frac{\partial N_8^e}{\partial z} \end{bmatrix} \{W^e\} \quad (2.56)$$

$$= [B^e] \{W^e\} \quad (2.57)$$

$$\begin{Bmatrix} \frac{\partial T}{\partial r} \\ \frac{\partial T}{\partial z} \end{Bmatrix} = \begin{bmatrix} \frac{\partial N_1^e}{\partial r} & - & - & - & \frac{\partial N_8^e}{\partial r} \\ \frac{\partial N_1^e}{\partial z} & - & - & - & \frac{\partial N_8^e}{\partial z} \end{bmatrix} \{T^e\} \quad (2.58)$$

$$= [B^e] \{T^e\} \quad (2.59)$$

$$\frac{\partial T}{\partial t} = \{N^e\}^T \frac{d\{T^e\}}{dt} = \{N^e\}^T \{\dot{T}^e\} \quad (2.60)$$

Here, the nodal values of W are known but arbitrary. The geometry is also approximated by the same shape functions:

$$r = \{N^e\}^T \{r^e\} \quad z = \{N^e\}^T \{z^e\} \quad (2.61)$$

The vectors $\{r^e\}$ and $\{z^e\}$ contain the nodal values of r and z coordinates respectively.

To express the boundary conditions in terms of the nodal quantities, approximation over the boundary is needed. Note that, as the domain is divided into nem number of elements, the boundary automatically gets divided into nbe number of elements. Now approximation for W , T , and q_w over a typical boundary element can be written as:

$$W = \{N^b\}^T \{W^b\} = \begin{Bmatrix} N_1^b & N_2^b & N_3^b \end{Bmatrix} \begin{Bmatrix} W_1^b \\ W_2^b \\ W_3^b \end{Bmatrix} \quad (2.62)$$

$$T = \{N^b\}^T \{T^b\} = \begin{Bmatrix} N_1^b & N_2^b & N_3^b \end{Bmatrix} \begin{Bmatrix} T_1^b \\ T_2^b \\ T_3^b \end{Bmatrix} \quad (2.63)$$

$$q_w = \{N^b\}^T \{q^b\} = \begin{Bmatrix} N_1^b & N_2^b & N_3^b \end{Bmatrix} \begin{Bmatrix} q_w^b \\ q_w^b \\ q_w^b \end{Bmatrix} \quad (2.64)$$

Note that the vector $\{N^b\}$ contains 1-D quadratic shape functions, which are consistent with the 2-D shape functions N_i^e .

Finite element equations

Substituting expressions (2.56-2.60) and (2.62-2.64), the integrals I_1, I_2 and I_3 can be written as

$$I_1 = \sum_{e=1}^{nem} \{W\}^e T \left(\int_{\Omega^e} \rho C_s \{N^e\} \{N^e\}^T dr dz \right) \{T^e\} \quad (2.65)$$

$$I_2 = \sum_{e=1}^{nem} \{W\}^e T \left(\int_{\Omega^e} k [B^e]^T [B^e] dr dz \right) \{T^e\} \quad (2.66)$$

$$I_3 = \sum_{b=1}^{nbe} -\{W^b\}^T \left(\int_{\Gamma_b} \{N^b\} \{N^b\}^T d\Gamma_b \{q_w^b\} \right) + \{W^b\}^T \left(\int_{\Gamma_b} h_b \{N^b\} \{N^b\}^T d\Gamma_b \right) \{T^b\} \quad (2.67)$$

Here, Ω^e is the domain of typical area element while Γ_b is the domain of typical boundary element. Then the expression (2.51) becomes

$$\sum_{e=1}^{nem} \{W^e\}^T [SC^e] \{T^e\} + \sum_{e=1}^{nem} \{W^e\}^T [SK^e] \{T^e\} + \sum_{b=1}^{nbe} \{W^b\}^T [SK^b] - \sum_{b=1}^{nbe} \{W^b\}^T [Sf^b] = 0 \quad (2.68)$$

where,

$$\left. \begin{aligned} [SC^e] &= \int_{\Omega^e} \rho C_s \{N^e\} \{N^e\}^T r dr dz \\ [SK^e] &= \int_{\Omega^e} k [B^e]^T [B^e] r dr dz \\ [SK^b] &= \int_{\Gamma_b} h \{N^b\} \{N^b\}^T r d\Gamma \\ \{Sf^b\} &= \int_{\Gamma_b} \{N^b\} \{N^b\}^T \{q_w^b\} r d\Gamma \end{aligned} \right\} \quad (2.69)$$

Here, $[SC^e]$ is elemental capacitance matrix, $[SK^e]$ is element conductivity matrix, $[SK^b]$ is boundary element conductivity matrix, and $\{Sf^b\}$ is boundary element flux vector.

When the elemental quantities of Eqs. (2.69) are assembled, the following global equations are obtained.

$$[GSC] \left\{ \dot{T} \right\} + [GSK] \{T\} = \{GSF\} \quad (2.70)$$

Where $[GSC]$ is global capacitance matrix due to spark, $[GSK]$ is global conductivity matrix due to spark, $\{GSF\}$ is global heat flux due to spark, $\{T\}$ is global temperature vector, and $\left\{ \dot{T} \right\}$ is time derivative of $\{T\}$.

Equations (2.70) represent a set of ordinary differential equations in the variable T as a function of time t . These equations are solved after application of implicit Finite Difference Method (FDM).

Finite difference scheme

The finite difference scheme used is the same as discussed in section 2.2.2 with the differences that $[C]$, $[K]$ and $\{F\}$ are replaced by $[GSC]$, $[GSK]$ and $\{GSF\}$ respectively. Here, two-time steps, Δt_1 for the on-time and Δt_2 for the off-time of EDM pulse power supply, are selected.

2.3.3 Results and Discussion

In order to assess the accuracy and sensitiveness of the EDM model, a problem involving variable heat flux profile over an axisymmetric zone is considered. Results are compared with the known theoretical results of Shankar et al. [70]. Since the heat flux profile is not of a standard configuration in Shankar's model, the results are obtained using two commonly used shapes: Circular disc heat source and Gaussian distributed heat source. The effect of heat flux is assumed [70] to be significant only upto a distance of $4R$ from spark center along radial direction as well as depthwise direction. The material properties are given in table 2.4 and process parameter in table 2.5. The heat flux is distributed over four elements along radial direction at workpiece top surface. From convergence point of view, it has been found that 256 elements with 833 nodes are adequate for the specified accuracy. Top surface temperature variation after $60 \mu s$ (after one spark) along radial direction is shown in Fig. 2.15. The results of present model with circular disc heat source are in closer agreement with the results of Shankar et al. [70] than the one with Gaussian heat source. But temperature distribution trend with Gaussian heat flux is closer to the shape of the crater formed at the workpiece surface by a spark.

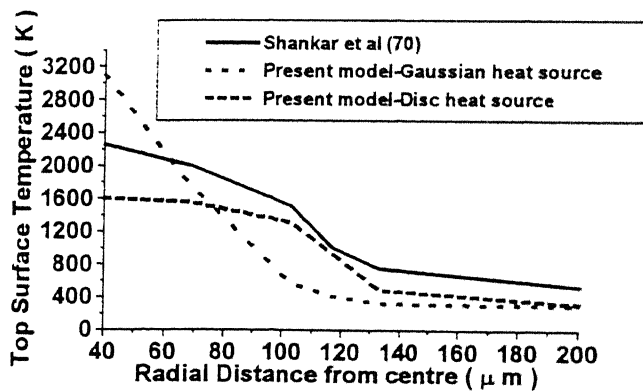


Fig 2.15 Comparison of variation of top surface temperature in 5 Cr die steel workpiece during EDM with heat flux of different profiles and the results of Shankar et al [70]. $t=60 \mu s$, $t_{on}=60 \mu s$, $t_p=120 \mu s$, without considering phase change and on-/off-time effect.

Effects of On-/off-time, duty cycle, energy partition and current on temperature distribution are discussed below.

On-/off-time

Figure 2.16 shows the top surface temperature variation considering the effects of on-/off-time and phase change (change of state from solid to liquid and liquid to vapour). The material properties are given in table 2.4 and process parameters are given in table 2.5. Further, to study the effect of on-off time on temperature distribution the time selected is $60 \mu\text{s}$ which falls in the off period of the pulse. The temperature is calculated using equation 2.70 and taking the time step $\Delta t = 30 \mu\text{s}$ (= on-time). Computational results can be obtained after a time interval, which is an integral multiple of on-time. Hence, the results are given after $60 \mu\text{s}$.

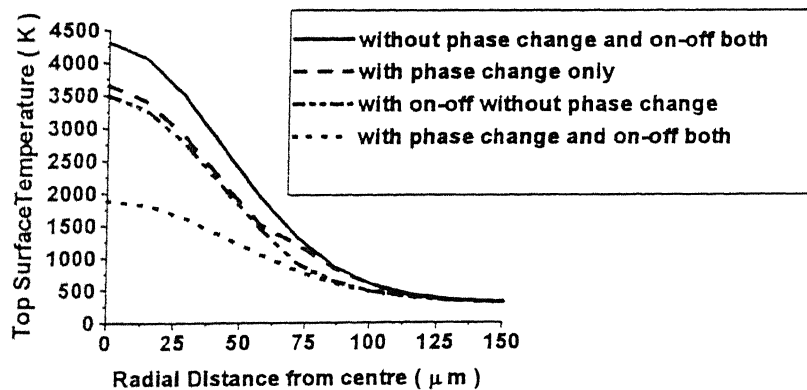


Fig 2.16 Top surface temperature variation in 5 Cr die steel workpiece during EDM computed with Gaussian heat flux profile including the effect of phase change and on-/off- time both after $60 \mu\text{s}$ for $t_{on} = 30 \mu\text{s}$, $t_p = 120 \mu\text{s}$

Obviously, higher peak temperature is observed if the effects of off-time of a pulse and phase change in the work material are not considered. This is so because it is assumed that the heat is supplied over the entire pulse period (off-time = 0), and further no heat is utilized for the change of phase from solid to liquid and then liquid to vapour. Further, reduction in temperature is observed if only phase change effect is considered because of the fact that some (latent) heat is utilized for phase change at constant

temperature. Therefore, the temperature rise is less in comparison to the previous case. If both the effects (on-/off-time and phase change) are taken into consideration, the peak temperature is still lower. This is because of the fact that heat is supplied only during the on-time of the pulse, and no heat is supplied during the off-time. Also, some fraction of the supplied heat is also spent on phase change. Hence, the overall temperature rise is much lower. This case is closer to real life situation.

Duty cycle

Figure 2.17 shows the effect of duty cycle (which is defined as the ratio of on-time to pulse time) on top surface temperature distribution in HSS workpiece after one pulse time. The duty cycle is changed by changing the on-time of the power supply by keeping the off-time same. The material properties are given in table 2.3 and process parameters are given in table 2.6. The curves show that higher temperature is obtained with higher value of duty cycle with the same off-time. About 10 % increase in peak temperature is observed by increasing the cycle time by 25%.

From above, it can be concluded that the present model simulates EDM process satisfactorily. It accounts many realistic facts viz., consideration of heat loss to the dielectric medium, on-/off-time consideration, energy partition to workpiece, duty cycle current, and consideration of phase change (Fig. 2.15-Fig. 2.20).

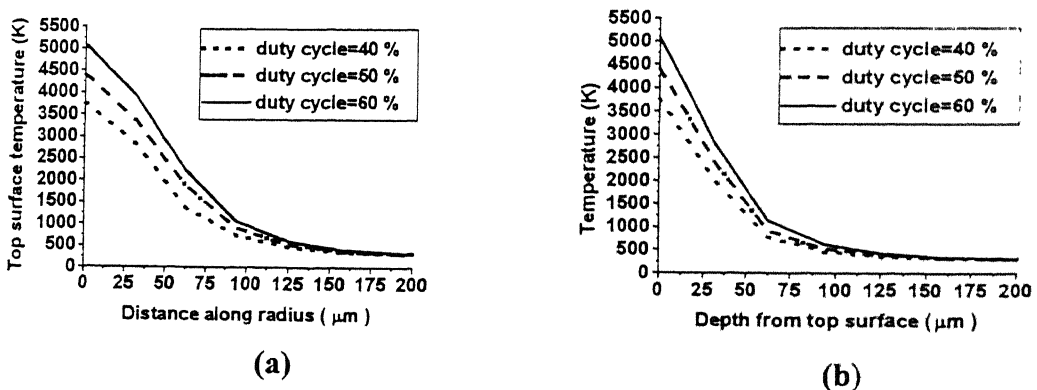


Fig 2.17 Variation of temperature with duty cycle (a) at top surface, (b) along depth, in HSS workpiece during EDM computed with Gaussian heat flux after one pulse time for $t_{on}=100 \mu s$.

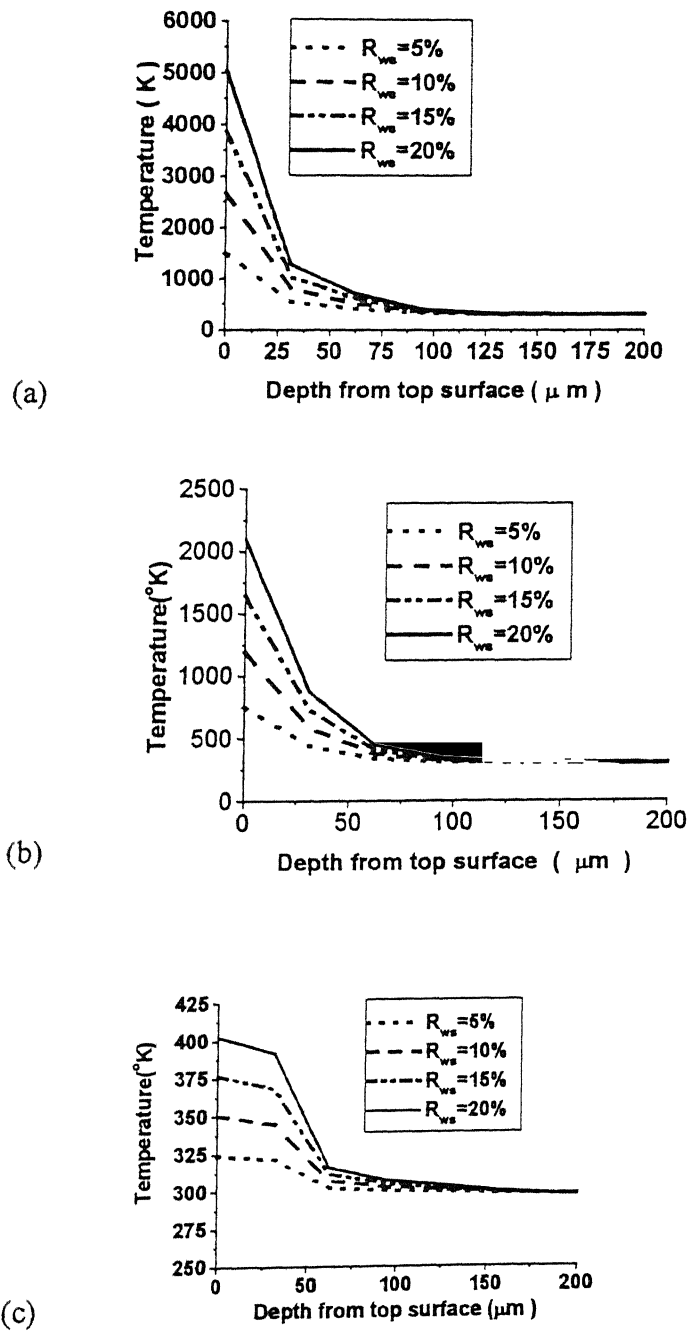


Fig 2.18 Depthwise temperature variations in HSS workpiece during EDM with Gaussian heat flux for $t_{on}=100 \mu s$, $t_p=200 \mu s$ after $100 \mu s$ at radial distance of (a) $r = 0$, (b) $r = R$, (c) $r = 2R$

Energy partition (R_{ws})

In the present FEA model prediction of temperature is governed by another important parameter, i.e. energy partition (R_{ws}). The thermal properties of workpiece electrode are given in table 2.3. Theoretically, electrode having lower value of thermal diffusivity ($k/\rho C_p$) receives lower share of heat energy than the one having higher value. Fig. 2.18 depicts the effect of R_{ws} on depthwise temperature distribution at different radial distances from the center of spark ($r = 0$, $r = R$ and $r = 2R$) after 100 μs . Process parameters are given in table 2.6. Higher temperature is observed at higher R_{ws} , which is expected because it gives more amount of heat entering into the workpiece. Trends are similar at all radial distances except at $r = 2R$ which is lying outside spark radius. The curves show that the temperature gradients are high along the depth of the workpiece if radial distance is small.

Figure 2.19 shows the top surface temperature variation along the radius for different values of R_{ws} after 100 μs . The top surface temperature at the center of the spark is also three times high when R_{ws} is increased by four fold. The temperature gradients at the top surface (within the spark radius) are high but comparatively less than the depthwise temperature gradient (Fig. 2.18a).

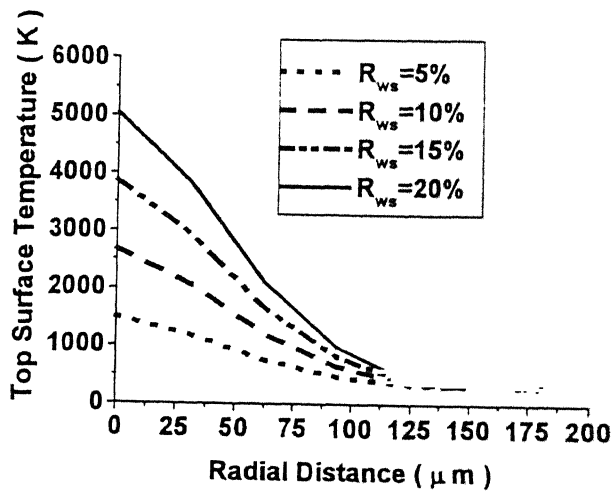


Fig 2.19 Top surface temperature variation in HSS workpiece during EDM with Gaussian heat flux for different values of partition ratio (R_{ws}) at $t_{on} = 100 \mu s$, $t_{off} = 200 \mu s$ after $t = 100 \mu s$.

Current

Figure 2.20 shows the effect of current on temperature distribution at top surface as well as along the depth after 100 μ s. The workpiece (HSS) material properties are given in table 2.3 and the process parameters are given in table 2.6. It is observed that increase in current leads to increase in peak temperature due to increase in heat flux (Eq. 2.44). The temperature gradient along depth is found to be steeper than temperature gradient along radial distance from center.

It is also noted that the temperature gradient is very high upto 30 μ m depth from top surface for all current values. Hence, from thermal stresses point of view, this thin surface layer is most critical. After this depth, temperature gradient gradually decreases. Almost no change in temperature at top surface as well as along depth is observed beyond the distance of one spark radius.

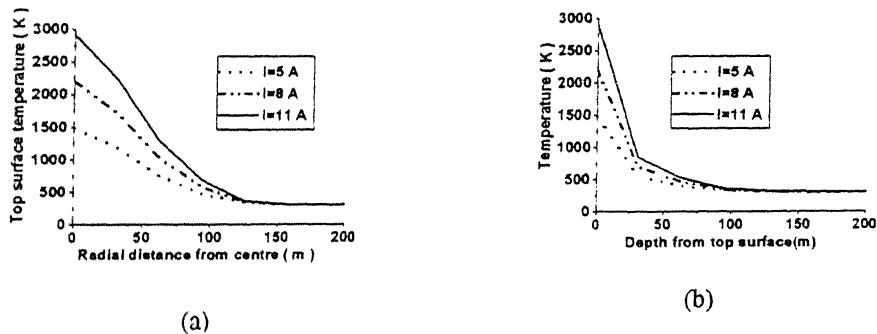


Fig 2.20 Temperature variation in HSS workpiece during EDM with Gaussian heat flux for different discharge current at $t_{on} = 100 \mu$ s, duty factor=50% after $t = 100 \mu$ s (a) along depth from top surface (b) along radial distance from centre

2.4 Temperature distribution in EDDG process

2.4.1 Theory of Superposition

Since, temperature independent properties of workpiece material are considered, the heat conduction equation is linear, hence the sum of known solutions also satisfies the heat conduction equation. Under these circumstances the combined temperature variation with time can also be obtained by addition of known solutions of simpler component problem [76]. According to this method different boundary temperature distributions with different initial conditions can be added to find final temperature distribution. Hence, the

resulting temperature (TT) due to grinding and EDM both is obtained by superposition of the two temperatures as follows:

$$TT = T_o + GTR + EDMTR \quad (2.71)$$

Where, GTR is temperature rise due to grinding and EDMTR is temperature rise due to EDM.

2.4.2 Results and Discussion

The EDDG in cut-off grinding mode is used for a HSS workpiece (6 mm X 6 mm X 20 mm) (Fig. 2.21a and table 2.3) with a grinding wheel having its width (6.5 mm) greater than the width of the workpiece (6 mm). Top surface discretization and locations of sparks (points •) on the workpiece surface are shown in Fig. 2.21b. Superposition technique is used to obtain temperature distribution in the workpiece due to EDDG, which includes the effect of diamond cut-off grinding as well as EDM on the rise in temperature at a point (a node).

First, 3-D temperature distribution in the workpiece due to cut-off grinding is obtained by using 2-D thermal analysis of cut-off grinding (Fig. 2.3-2.4). Let us consider a plane $Y_1Y_2Y_3Y_4$ parallel to y-z plane (Fig. 2.21a). It is assumed that the temperature along the width of the workpiece (y-axis) at a specified depth in the given plane, say $Y_1Y_2Y_3Y_4$, is same during cut-off grinding. For example, temperature at any point along the line Y_1-Y_2 on the top surface of the workpiece will be same during cut-off grinding. In the same way, temperature at any point along the line PP_1 (Fig. 2.21a) will also be same but of different magnitude as compared to that along Y_1-Y_2 in the plane $Y_1Y_2Y_3Y_4$. Using this procedure, 3-D nodal temperatures are obtained at any specified grinding time which is an integral multiple of time required for grinding wheel to move downward by one element length (0.5 mm).

During EDM, sparking takes place at a point of least resistance [6], which depends on surface roughness of both the electrodes. Chances of occurrence of next spark at the location in the next cycle are comparatively less. Until spark does not reoccur at the same location, there will be no heat input at that point (or node). Keeping this

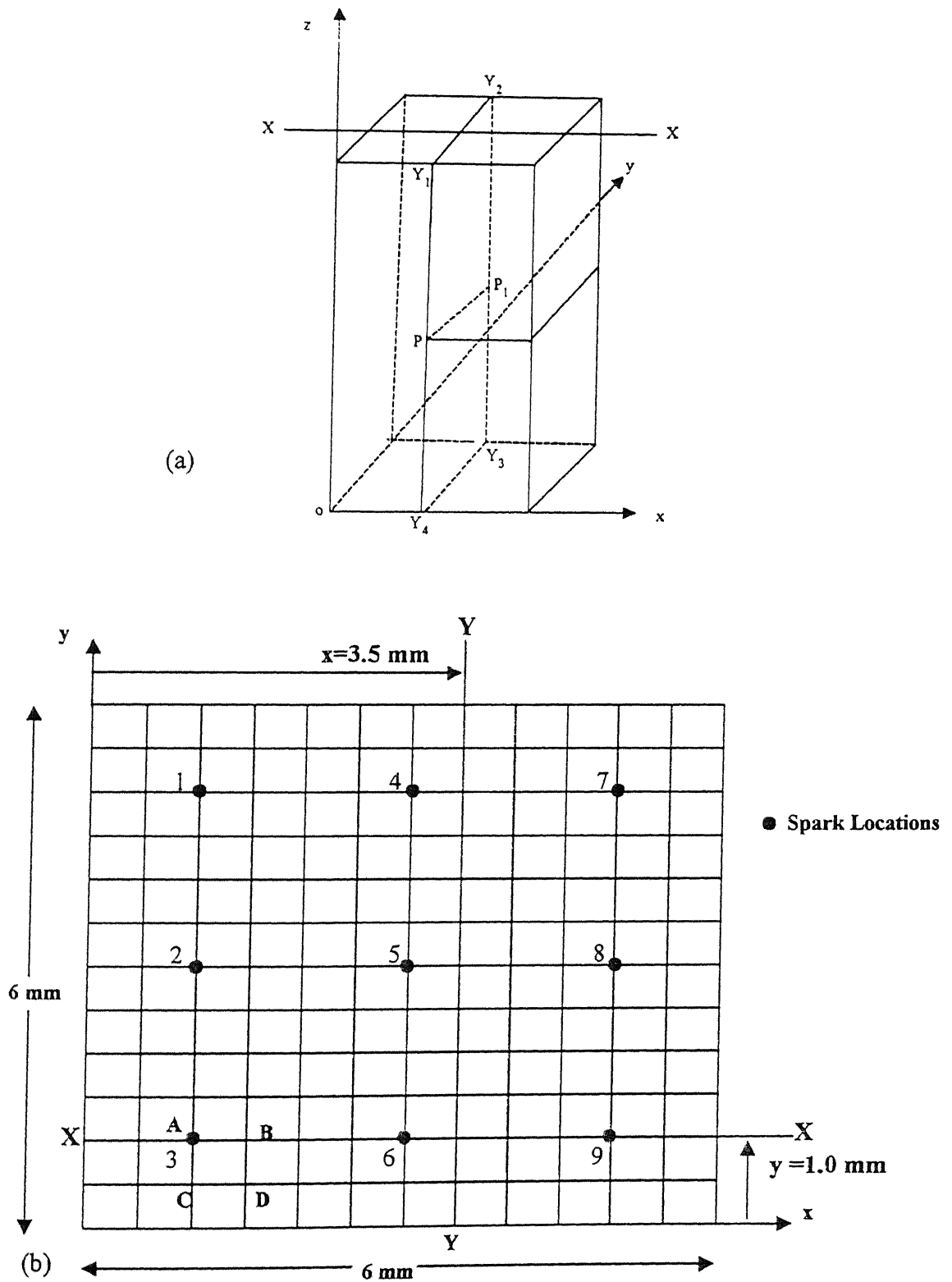


Fig. 2.21 (a) 3-D domain of workpiece (b) Discretization of workpiece top surface used in superposition

characteristic of EDM in mind, heat input to the workpiece by sparks has been simulated as follows.

It has been assumed that spark strikes at the workpiece top surface at selected points (Fig. 2.21b). It is considered that only one spark takes place at a time (say, at point 1) and next spark at the same location is repeated in sequence after sparking at all other selected locations (2 to 9 in Fig. 2.21b) are over. This pattern has been assumed to simplify the problem as well as to match the grinding time for one element movement in downward direction (in FEM computation) with total time of sparking in that duration. The grinding time for one element movement in downward direction is completely matched with total time of sparking at all other 9 locations. For this matching of time, 24 times sparking is needed at each of the nine spark locations with on time of $75\text{ }\mu\text{s}$ and off time of $150\text{ }\mu\text{s}$. In this way, at each spark location, heat will be supplied for $75\text{ }\mu\text{s}$ and again it will be repeated after $1950\text{ }\mu\text{s}$ (sum of the cycle time of 8 sparks of 8 locations plus off time of the spark at present location).

After several numerical experiments it has been found that the axisymmetric 3-D domain influenced by the heat of a spark is upto $8R$ distance along radius as well as depth from the center of the spark after EDDG for 0.05 s (Fig. 2.22). This range of $8R$ may change with the time of machining (say, 0.05 s in this case). It is seen (Fig. 2.22) that the temperature achieved at $8R$ after 0.05 s is almost room temperature. Further, this whole

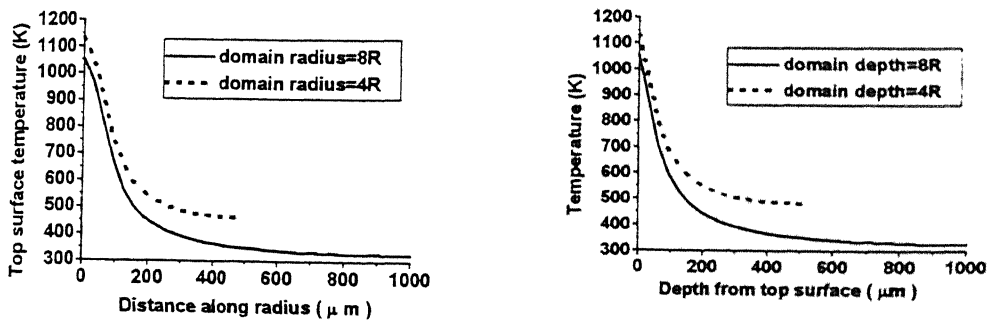


Fig 2.22 Variation of temperature (a) at top surface along radius (b) along depth at $r=0$, of two different size of HSS workpiece domain after 0.05 s of machining time using EDM

axisymmetric domain is found to lie within 4-elements length along x- and y-axis, and two-element length along z-axis of grinding domain. Nodal temperatures of the axisymmetric domain due to sparks, which lie on the nodes of grinding domain, are scalarly added to the temperature rise due to grinding to get combined temperature (i.e. the change in nodal temperature due to EDDG process as a whole).

The rectangular parallelepiped domain of 16R X 16R X 8R around a spark could be reasonably considered as a domain independent of the effect of heat from the neighboring sparks (assuming that the temperature distribution is evaluated after 0.05 s of grinding). Nine such solid blocks are assumed to be fitted within a single solid block of dimension 48R length along x-axis, 48R width along y-axis, and 8R depth from top surface opposite to z-axis.

Due to spark the temperature is affected only in certain small domain around the spark. If the subsequent spark occurs outside the zone of influence of the first spark then it will not affect the temperature distribution given by the proposed model. Thus, even if spark locations are chosen randomly the temperature distribution will not change as long as subsequent spark locations are outside the zone of influence of the current spark. However, if the subsequent spark occurs within the zone of influence of current sparks, the temperature distribution will certainly gets affected but then the problem will become 3-D. To avoid this complexity it is assumed that the subsequent spark occurs outside the zone of influence of current spark.

Fig. 2.23(a) shows the top surface temperature distribution after superposition of grinding and EDM temperature distributions. Process parameters are given in table 2.6. The figure shows that the peak temperatures are observed at the nine spark locations. The contour plot of isotherms is shown in Fig. 2.23(b). It is seen under microscope that the EDM'd surfaces have craters all around it. These very high temperature peaks (Fig. 2.23a) are responsible for the craters on the EDM'd surface. However, during EDDG, most of these craters would vanish during grinding part of the EDDG process. It is evidenced by the micrograph of EDDG'd surfaces given in reference [29].

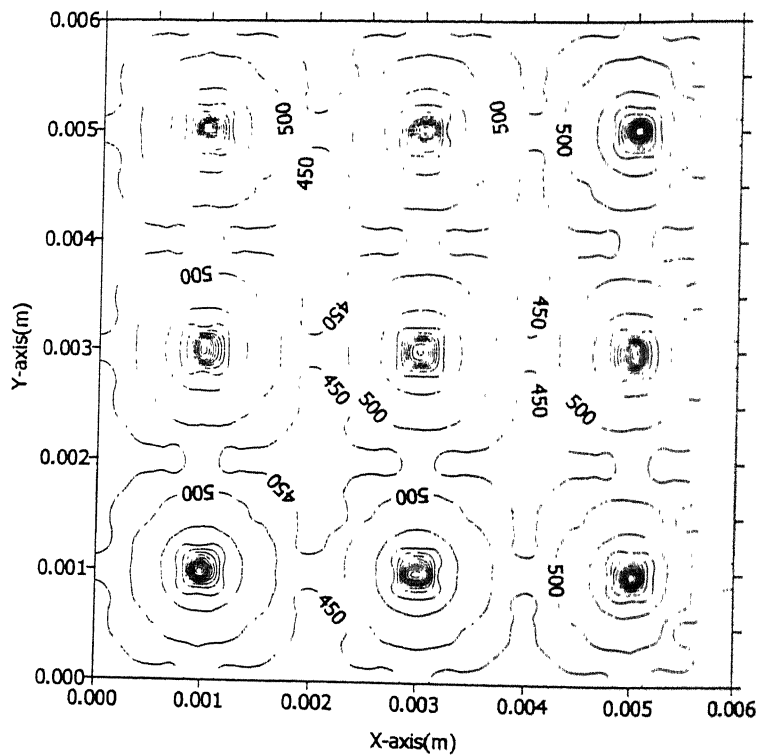
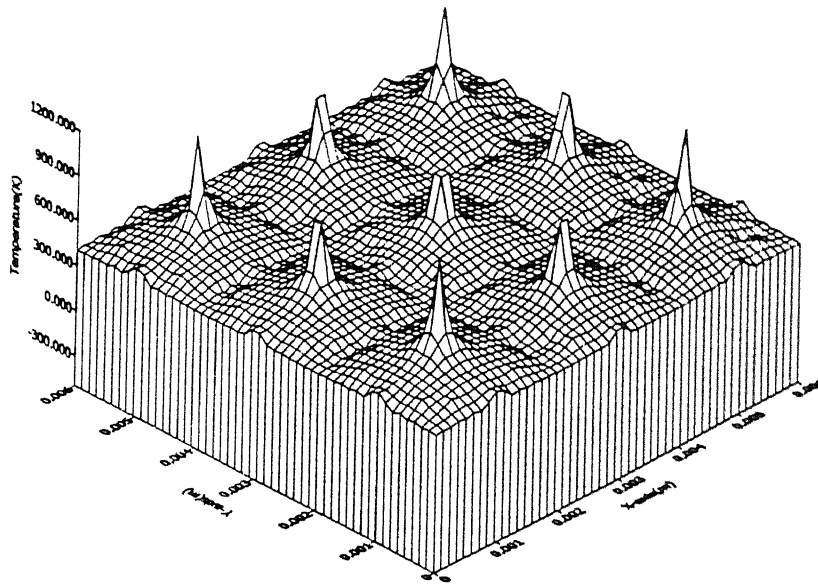
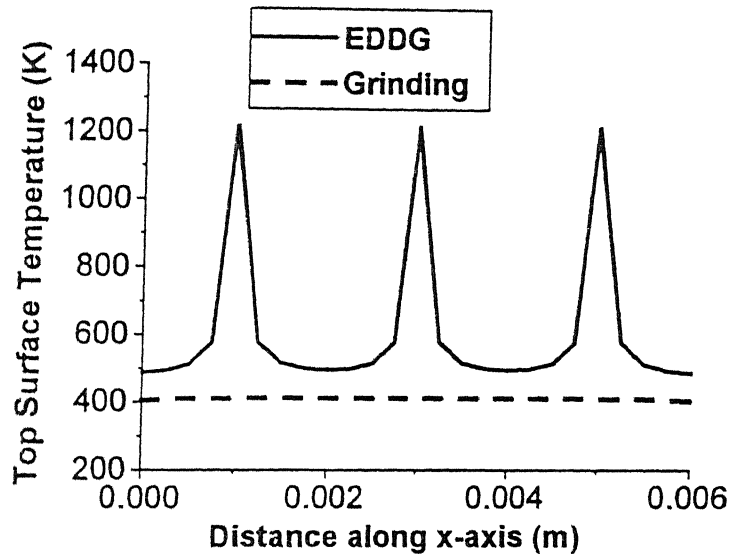
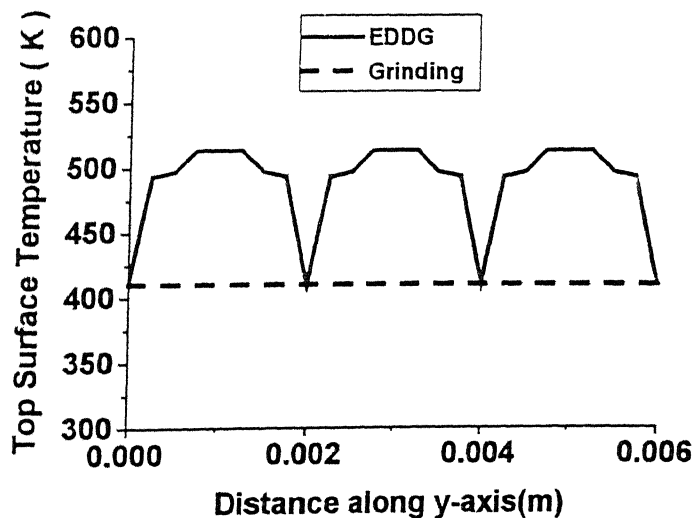


Fig 2.23 Temperature distribution in HSS workpiece during EDDG process for $t_{on}=75 \mu s$, $t_{off}=150 \mu s$ after $t=0.05s$ (a) 3-D surface plots (b) Contour plots

Figure 2.24(a) shows the temperature distribution at workpiece top surface due to EDDG process in X-X plane (parallel to x-axis) at $y=1.0$ mm (Fig. 2.21b). As expected, a sharp increase in temperature is observed around spark locations. Top surface temperature of about 400 K is calculated due to grinding when no sparking is allowed to



(a)



(b)

Fig 2.24 Top surface temperature distribution in HSS workpiece during EDDG after $t=0.05$ s. (a) along x-axis at $y=1.0$ mm (along X-X in Fig. 2.21 b), (b) along y-axis at $x=3.5$ mm (along Y-Y in Fig. 2.21 b). $t_{on}=75$ μ s, $t_{off}=150$ μ s

take place by switching off the power supply. The peak temperature due to grinding and EDM both at the spark location is calculated about 1206 K after 0.05 s. Temperature gradient is found to be very high near the spark locations. Similarly top surface temperature variation along Y-Y (parallel to y-axis) at $x = 3.5$ mm (Fig. 2.21b) is shown in Fig. 2.24(b).

Depthwise variation of temperature at locations A, B, C and D (Fig. 2.21b) in the workpiece due to EDDG is shown in Fig. 2.25. It is noted that temperature gradient is very high within a thin surface layer of 0.63 mm. Beyond this depth temperature gradient variation is almost zero. This shows that temperature-softening effect is limited to a thin layer near the spark flux.

Effects of duty cycle, on-time, current, energy partition, feed velocity, and time of machining are discussed below (Fig. 2.26-2.34). The process parameters other than the parameter under study are taken from table 2.6.

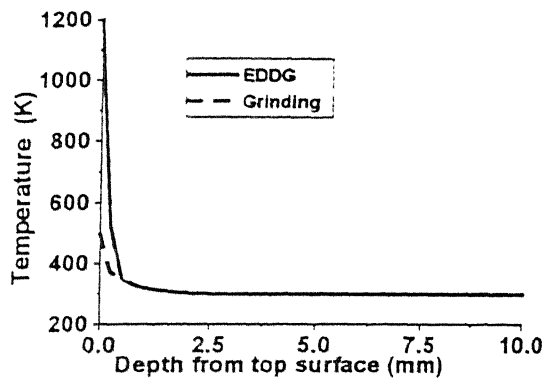
Duty Cycle

Figure 2.26a and 2.26b shows the effect of duty cycle on top surface temperature distribution in the workplace due to EDDG process. The process parameters are given in table 2.6. Duty cycle is changed by changing off-time and keeping on-time constant. No significant change in top surface temperature is noticed due to variation in duty cycle. This is because, after the on-time duration the heat supply at each of the spark location resumes after a long period (which is the sum of off-time duration of the present location plus the pulse time of other eight spark locations). Hence, the temperature of the EDM domain comes down to the same level for all duty cycles.

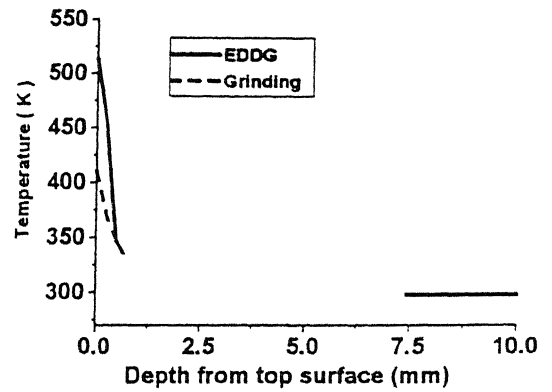
Figure 2.26c shows the effect of duty cycle on depthwise temperature variation for the same set of conditions as used in Fig. 2.25. Very small change in temperature is observed upto 175 μm depth. This shows that the temperature-softening zone at the top surface does not change with the duty cycles.

On time

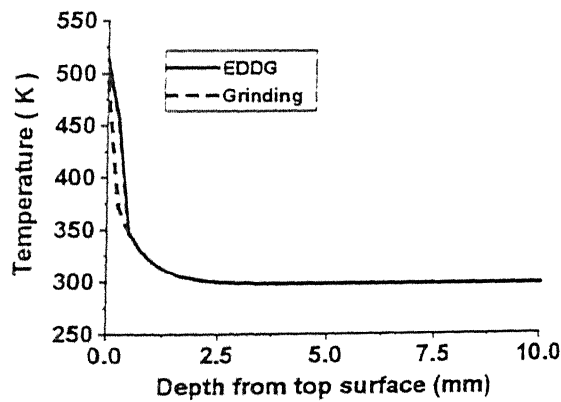
Figure 2.27 shows the effect of on-time on top surface and depthwise temperature distribution in the workpiece due to EDDG process. The process parameters are same as in table 2.6. Significant change in top surface temperature is noticed due to variation in



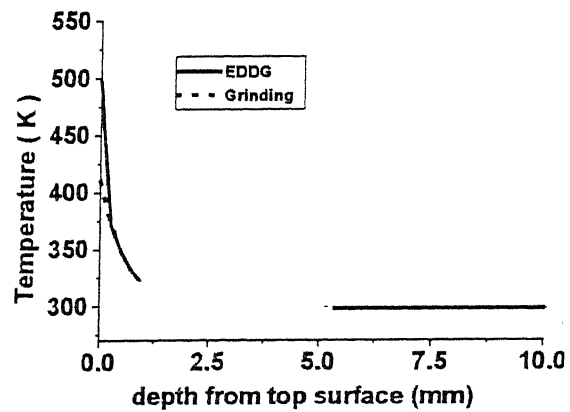
(a)



(b)



(c)



(d)

Fig 2.25 Depthwise temperature distribution in HSS workpiece during EDDG process after $t=0.05s$ at (a) $x=1.0$ mm and $y=1.0$ mm (Point A), (b) $x=1.5$ mm and $y=1.0$ mm (Point B), (c) $x=1.0$ mm and $y=0.5$ mm (Point C), (d) $x=1.5$ mm and $y=0.5$ mm (Point D). (Fig 2.21b)

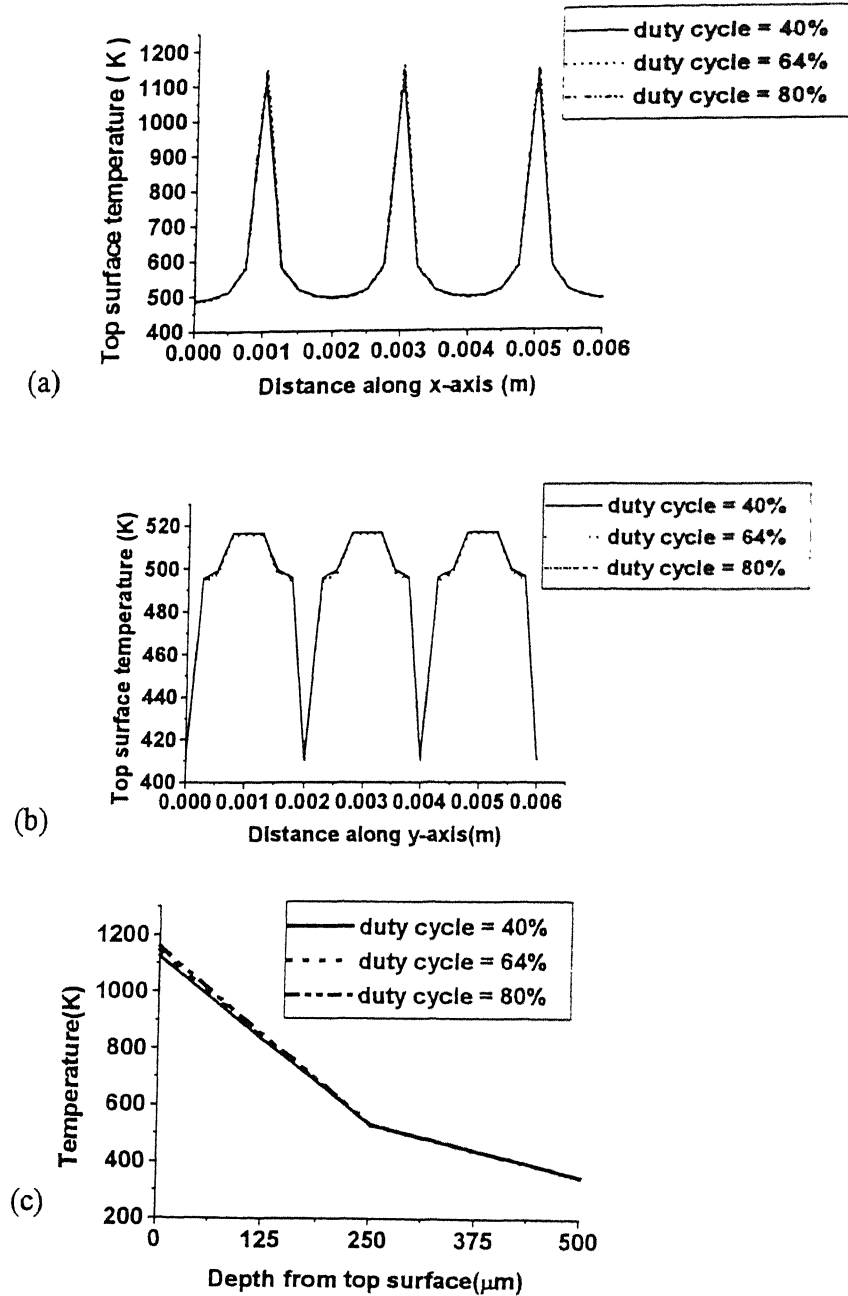
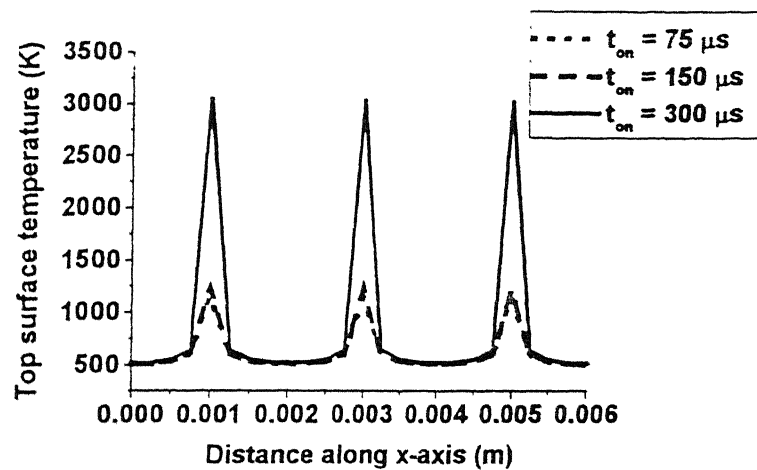
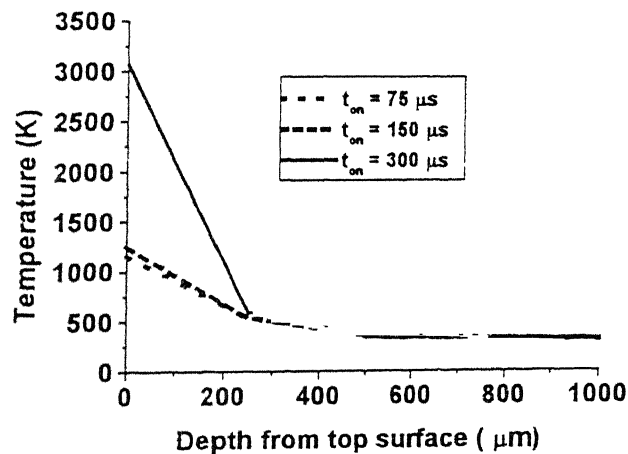


Fig. 2.26 Effect of duty cycle on temperature distribution (a) on top surface along x-axis at $y=1.0$ mm (along X-X) (b) on top surface along y-axis at $x=3.5$ mm (along Y-Y) (c) along depth at $x=1.0$ mm and $y=1.0$ mm (Point A) (Fig. 2.21b) in HSS workpiece during EDDG process after $t=0.05$ s for $V_f = 10.29$ mm/s, $t_{on}=150\mu\text{s}$



(a)



(b)

Fig 2.27 Effect of on time on temperature distribution (a) at top surface along x-axis at $y=1.0$ mm (along X-X) (b) along depth at $x=1.0$ mm and $y=1.0$ mm (Point A) (Fig. 2.21b) in HSS workpiece during EDDG process after 0.05

on-time. This is so because larger amount of heat is supplied at each of the spark location during longer on-time than the shorter on-time pulses.

Feed

Figure 2.28 (a) shows the top surface temperature distribution in X-X plane at different feed rates. The process parameters are same as in table 2.6. At every spark location, the temperature at the center of a spark remains the same, as there is no change in electrical power input related to EDM. Secondly, after one spark has occurred, the heat supply by

the next spark at the same location resumes after a long period (which is the sum of off-time duration of the present location plus the pulse time of other eight spark locations). However, number of sparks at a spark location with increase in feed may decrease which may lead to higher contribution by grinding in EDDG.

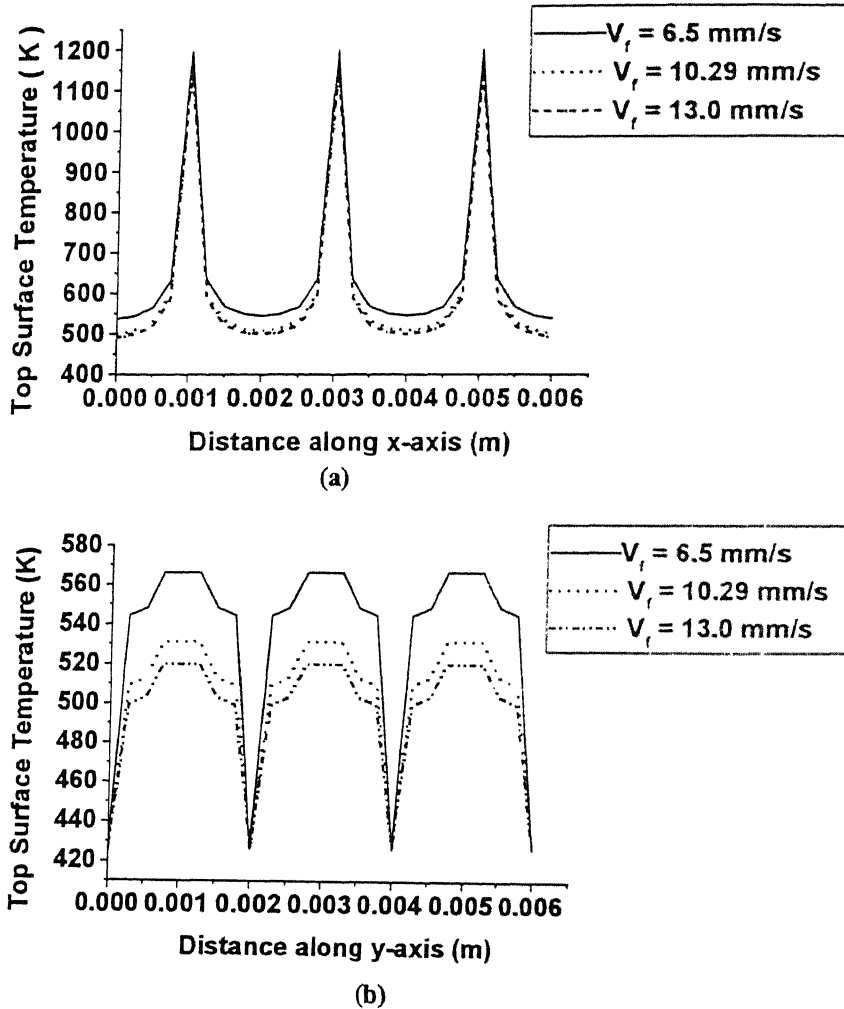
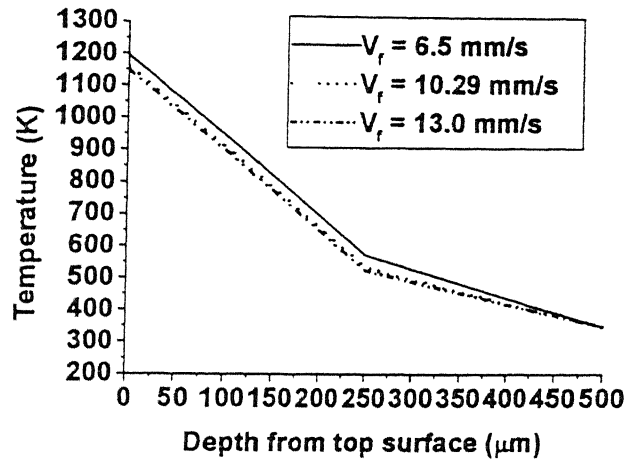


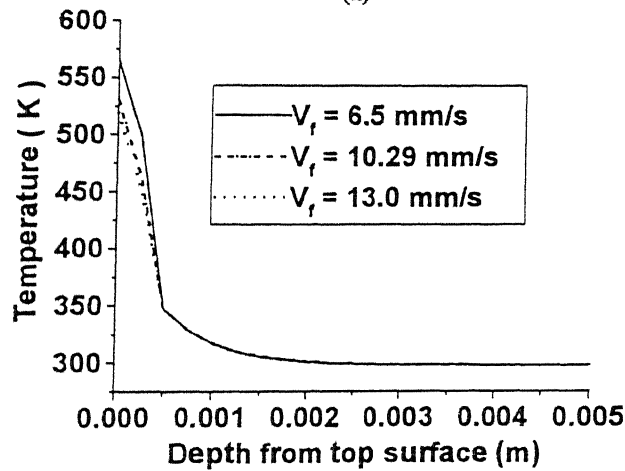
Fig 2.28 Effect of feed velocity on top surface temperature distribution in HSS workpiece during EDDG process after 0.05 s (a) along x-axis at $y=1.0$ mm (along X-X in Fig. 2.21 b) (b) along y-axis at $x=3.5$ mm (along Y-Y in Fig. 2.21 b).

Away from the spark center, the effect of feed is noticed. Higher temperature is observed for lower feed and vice versa (Fig. 2.28a). This is because, the contact duration of grinding wheel with workpiece is more at the lower feed. Similar trend is observed along y-axis at $x=3.5$ mm (Fig. 2.28(b)). Figure 2.29 shows the effect of feed on

depthwise temperature distribution. Increase in temperature is noticed due to decrease in feed.



(a)



(b)

Fig 2.29 Effect of feed velocity on temperature distribution along depth in HSS workpiece during EDDG after 0.05 s at (a) $x=1.0$ mm and $y=1.0$ mm (Point A Fig. 2.21 b) (b) $x=1.0$ mm and $y=0.5$ mm (Point C Fig. 2.21 b).

Current

Effect of current on top surface temperature distribution is shown in Fig. 2.30(a) and 2.30(b). A significant change in the peak temperature is observed at spark locations. This is due to the fact that heat flux increases with the increase in current (Eq. 2.44). About five fold increase in temperature is observed when the current is increases to three times. The peak temperature is about 5900 K when the current is 24 A along X-X at

$y=1.0$ mm (Fig. 2.21b). Fig. 2.30c shows the effect of current on depthwise temperature distribution at point A of Fig. 2.21b. The effect is observed upto $500\text{ }\mu\text{m}$.

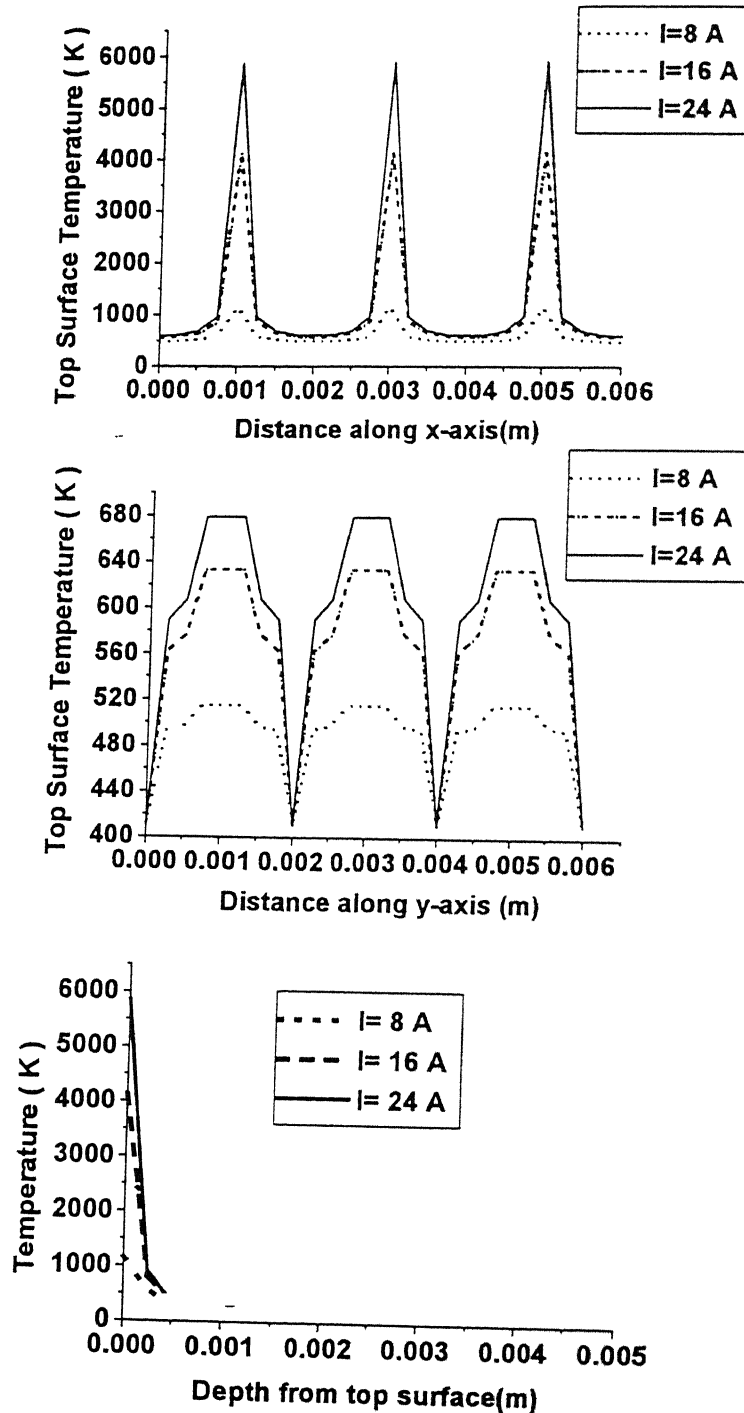


Fig 2.30 Effect of current on temperature distribution (a) top surface along x-axis at $y=1.0$ mm (along X-X) (b) top surface along y-axis at $x=3.5$ mm (along Y-Y). (c) along depth in at $x=1.0$ mm and $y=1.0$ mm (Point A Fig. 2.21 b) in HSS workpiece during EDDG after 0.05 s

Energy Partition due to EDM (R_{ws})

Effect of energy partition on top surface temperature distribution is shown in Figs. 2.31(a) and 2.31(b). A significant change in the peak temperature is observed at spark locations. This is due to the fact that heat flux increases with R_{ws} (Eq. 2.44). The peak temperature is about 7200 K when the R_{ws} is 0.40 along X-X at $y=1.0$ mm (Fig. 2.21b). Fig. 2.32 shows the effect of R_{ws} on depthwise temperature distribution at point A of Fig. 2.21b. A sharp decrease in temperature gradient is observed upto 250 μm depth and then decreases slowly upto 500 μm before approaching to grinding temperature. This shows that the critical zone for high thermal stresses (because of high temperature gradient) lies within 250 μm depth only (for the used process condition) irrespective of energy partition due to EDM.

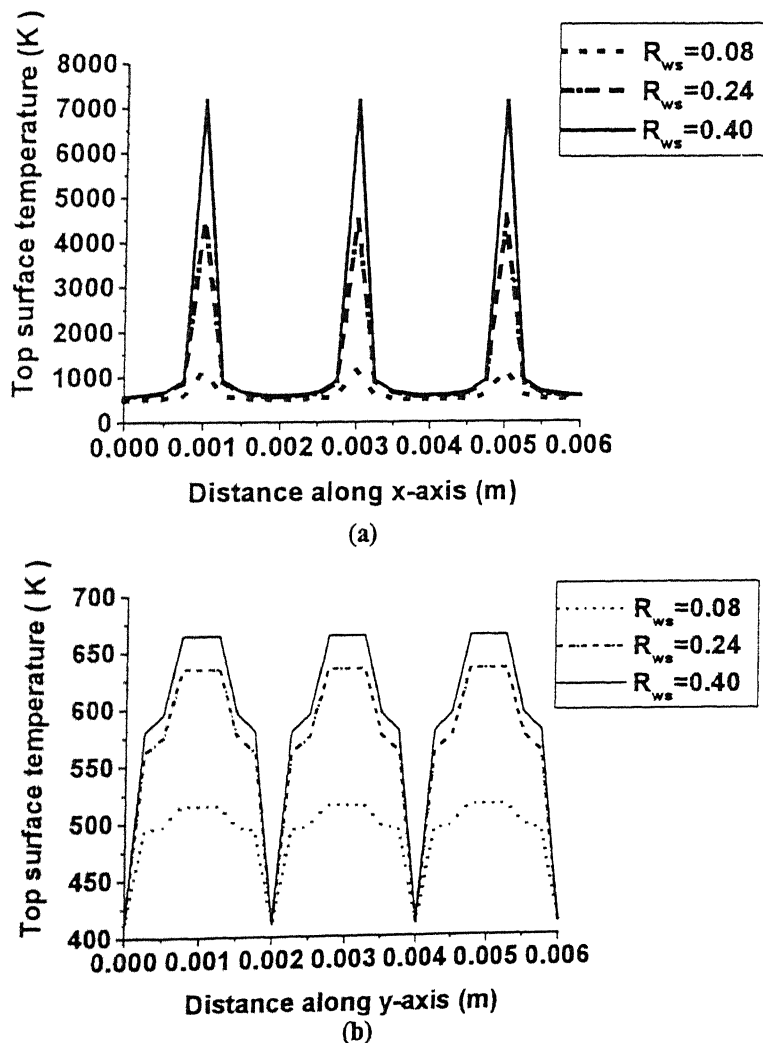


Fig 2.31 Effect of R_{ws} on top surface temperature distribution in HSS workpiece
 (a) along x-axis at $y=1.0$ mm (along X-X in Fig. 2.21b)

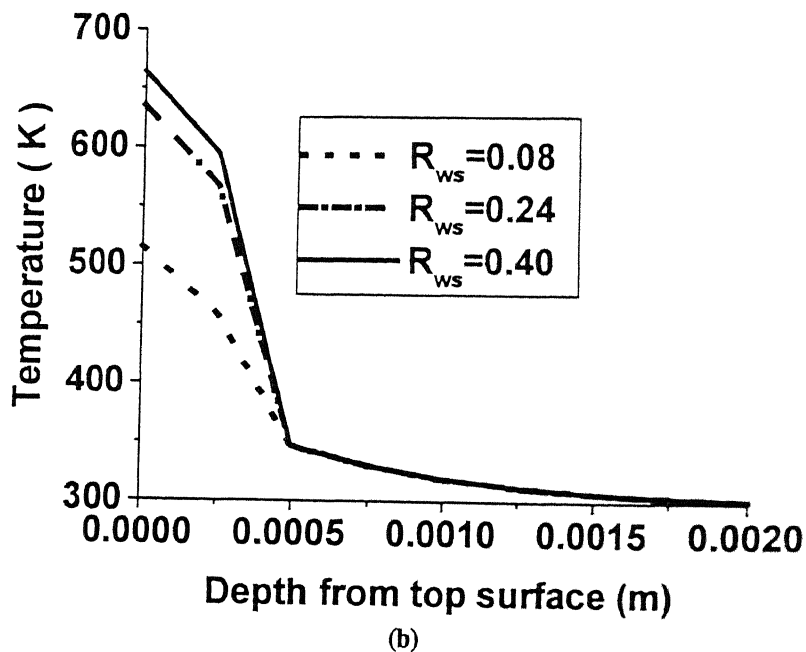
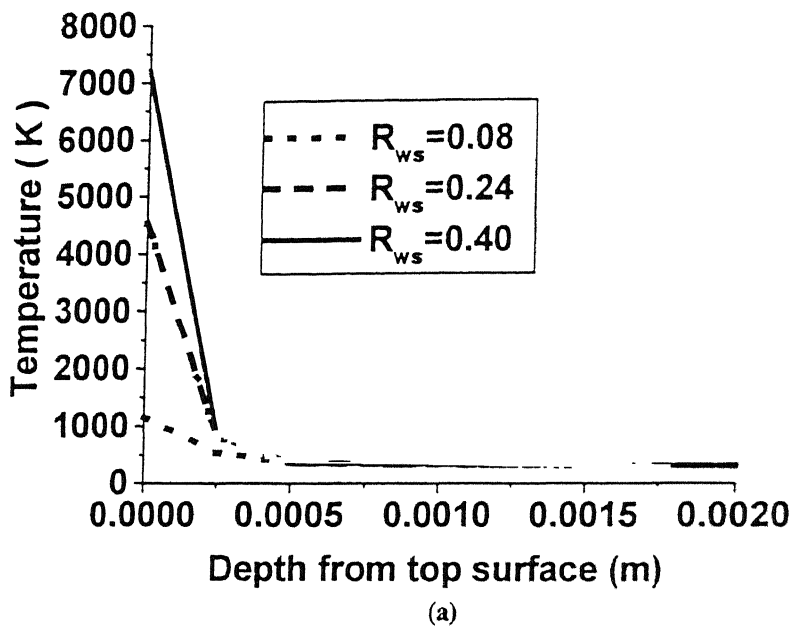


Fig 2.32 Effect of R_{ws} on temperature distribution along depth in HSS workpiece during EDDG process after 0.05 s at (a) $x=1.0$ mm and $y=1.0$ mm (Point A Fig. 2.21 b) $x=1.0$ mm and $y=0.5$ mm (Point C Fig. 2.21b)

Time of machining (t)

Effect of machining time on top surface temperature distribution is shown in Fig. 2.33(a) and 2.33(b). A significant change in temperature is observed away from the spark radius. This is due to the fact that cut-off grinding temperature increases with the machining time. The peak temperature of about 1400 K is noted after machining time of 0.04 s along X-X at $y=1.0$ mm (Fig. 2.21b). Temperature at spark center is increased by 200 K after four fold increase in machining time. Fig. 2.34 shows the effect of machining time on depthwise temperature distribution. The effect is observed upto 500 μm only.

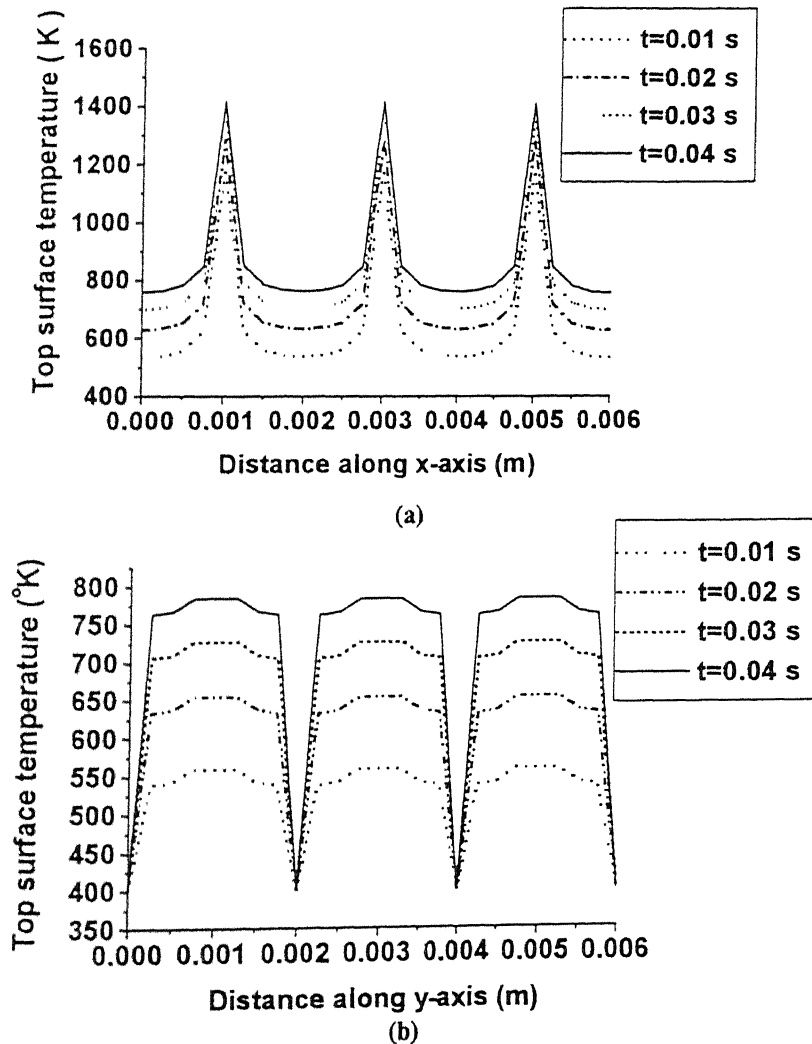
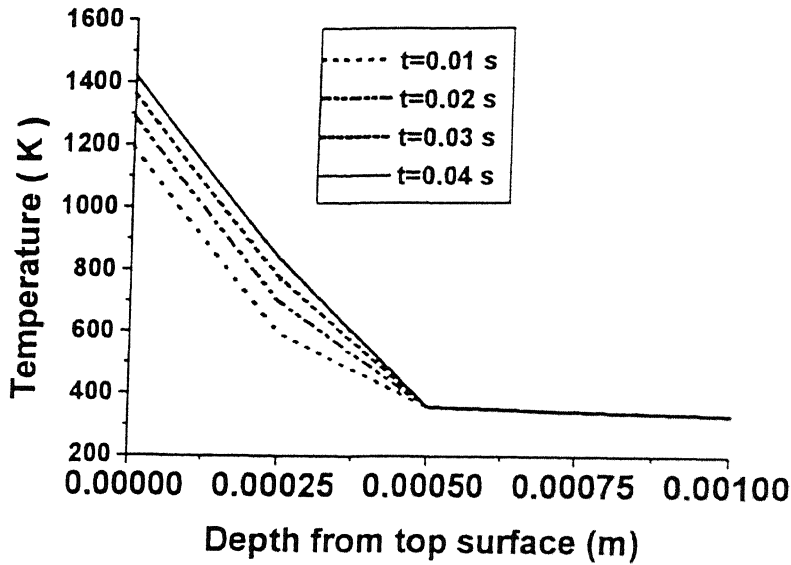
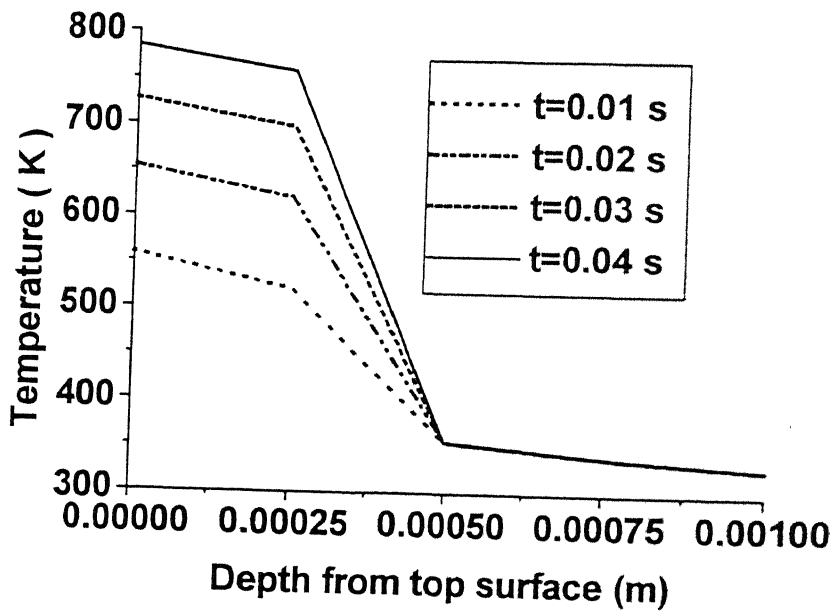


Fig 2.33 Effect of grinding time on top surface temperature distribution in HSS workpiece during EDDG process (a) along x-axis at $y=1.0$ mm (along X-X in Fig. 2.21b) (b) along y-axis at $x=3.5$ mm (along Y-Y in Fig. 2.21b).



(a)



(b)

Fig 2.34 Effect of grinding time on temperature distribution along depth in HSS workpiece during EDDG process (a) $x=1.0$ mm and $y=1.0$ mm (Point A Fig. 2.21b), (b) $x=1.0$ mm and $y=0.5$ mm (Point C Fig. 2.21b).

Table 2.1: Properties of workpiece used for Figures 2.5-2.11 [71]

Workpiece	AISI 1020 Steel
Wheel	19 mm X 6 mm X22 mm Resin bonded Al_2O_3
ρ_w (kg/m ³)	7800
C_s (J/kg K)	448.7
k (W/mK)	70.0
T_o (K)	298

Table 2.2: Feed dependent values of R_{wg} and U_o for AISI 1020 steel workpiece and resin bonded Al_2O_3 wheel during cut-off grinding [71]

V_f (mm/s)	R_{wg}	U_o (GPa)
3.2	0.31	13.58
4.0	0.31	13.58
6.4	0.29	7.55
9.35	0.27	6.2
12.8	0.23	5.3

Table 2.3: Properties of HSS workpiece used in present model [70]

Size	6 mm X 6 mm X 20 mm
Wheel	Metal bonded diamond wheel
ρ_w (kg/m ³)	8691
ρ_s (kg/m ³)	3520
C_s (J/kg K)	419
C_l (J/kg K)	752
L_m (J/kg K)	2735000.0
L_v (J/kg K)	15760000.0
T_m (K)	1965
T_v (K)	3100
k (W/mK)	40.2
k_s (W/mK)	2000
h_c (W/m ² K)	10000.0 (Kerosene)
E (GN/m ²)	208
α_t (/K)	11.7×10^{-6}
α_w (m ² /s)	11×10^{-6}

Table 2.4: Properties of workpiece used for Figures 2.15-2.16 [70]

Workpiece	5 Cr Die Steel
ρ_w (kg/m ³)	8593
C_s (J/kg K)	425.0
C_l (J/kg K)	752.0
k (W/mK)	48.5
L_m (J/kg)	2735000.0
L_v (J/kg)	15760000.0
T_m (K)	1965
T_v (K)	3100

Table 2.5: Process parameters used for Figures 2.15-2.16

R_{ws}	0.42
I (A)	6.5
U_b (Volt)	28
R (μ m)	115

Table 2.6: Process parameters used for Figures 2.17-2.34

V_f (mm/s)	10.29
R_{wg}	0.08
R_{ws}	0.08
U_o (GPa)	10.55
I (A)	8
U_b (Volt)	40
R (μ m)	125
t_{on} (μ s)	75
t_{off} (μ s)	150

2.5 Conclusions

The present investigation shows that the temperature distribution in workpiece during EDDG can be simulated by means of FEM. This reduces the need for costly and time-consuming measurements to determine workpiece temperature. The proposed FEM approach takes care of the different length scales of the constituent process of EDDG (grinding and EDM) by using the superposition theorem. Thus, the 2-D temperature analysis of cut-off grinding and the axisymmetric analysis of EDM it is possible to predict the 3-D temperature distribution in the workpiece due to EDDG. Temperature studies based on 2-D temperature analysis of cut-off grinding and axisymmetric analysis of EDM compose favorably well with the experimental/theoretical results available in the literature.

A sharp increase in temperature is observed around spark locations at the top surface of the workpiece. This shows that temperature-softening effects is limited to a thin layer around the spark flux. These are the well known facts in case of EDM but these facts were not verified in case of EDDG quantitatively where sparking and grinding both are taking place simultaneously at the top surface of the workpiece. In EDDG the convection is taking place at the side surfaces due to presence of dielectric. I have found temperature and its softening effects quantitatively in case of EDDG where governing equations are different for EDM and grinding both with variable boundary conditions. The softening effect is significant upto 500 μm for the conditions taken. These results would be useful in the design of EDDG operations. The model can predict temperature distribution in the workpiece including the effects of duty cycle, current, feed and time of machining if accurate values of energy partition due to both cut-off grinding and EDM, and for the conditions under consideration are known in advance.

Chapter 3

Thermal Stress Analysis of EDDG

3.1 Introduction

The concept of surface integrity has been widely accepted by researchers and industry experts in evaluating surface integrity of the machined surface. This term includes all aspects of the quality of surface, including surface finish, metallurgical damage and residual stresses [71]. Machining operation produces a surface with a variety of surface alterations. The major types of alterations are: plastic deformation, micro-and macro cracking, untempered and overtempered martensite, phase transformation and residual stresses [77]. High temperature and/or high temperature gradients, and plastic deformation are the major cause of surface alterations.

The thermal stresses in the workpiece are the best indicators of thermal influence on the surface integrity. Undesired residual stress distribution in a machined component results in lowering its dynamic strength, fatigue life, chemical resistance, magnetic properties and so forth. Need for theoretical study of thermal stresses arises because purely experimental investigation is too expensive and sometimes very difficult to perform. A theoretical method can take into account many principal effects simultaneously like mechanical, thermal, microstructural, and chemical.

Heat generated within the machining zone causes a non-uniform temperature field in the workpiece leading to unknown material expansion of the workpiece [72]. Since bulk of the workpiece material under the top surface is still cool, expansion is constrained which produces compressive stresses in the sub-surface layer of the workpiece. The value of the thermal stress depends on temperature gradient and material properties. When the thermal stress reaches material yield stress value, permanent deformation occurs in the workpiece. As the workpiece cools, tensile stresses are created and remain in the workpiece. Therefore, a thorough examination of thermal stress development helps in understanding the relationship between machining conditions and thermal stress distribution.

Both the constituent processes of EDDG (cut-off grinding and EDM) generate heat, which can cause thermal stresses in the workpiece. The study of thermal stresses in the whole workpiece domain due to EDDG consists of thermal stresses due to both diamond cut-off grinding and EDM.

In this chapter, an attempt is made to develop two independent FEM based models for the prediction of thermal stresses due to diamond cut-off grinding and EDM. Computation of thermal stresses is performed for various cut-off grinding and EDM parameters.

3.2 Thermal Stresses in Cut-off Grinding

Most of the thermal residual stress models available in literature [78-82] are limited to surface grinding for alumina wheels. Mishra and Prasad [78] applied finite element method to determine the residual stresses using the temperature field of Jaeger [35]. However, in their analysis the semi-infinite solid does not finally cool down to room temperature. Hence the use of the term residual stress is somewhat misleading. A comprehensive model for the quantitative prediction of thermal residual stresses in surface grinding is offered by Vansevenant [79]. An elastic-viscoplastic model developed by Li and Chen [80] has been used for predicting the residual stresses in surface grinding. But all these models assume that the line heat source or uniform rectangular heat source moves over the workpiece top surface. Mahdi and Zhang [81] have analyzed the thermal residual stresses induced by surface grinding with the aid of finite element method. Further, they have studied the coupled effect of thermo-plasticity and phase transformation on residual stresses [82]. The model developed by Chen et al. [83] is capable of predicting the critical temperature as a function of grinding condition after which the tensile residual stresses are generated.

In contrast to surface grinding, an analysis of thermal stresses during cut-off grinding is lacking. In this section, a numerical model is presented for the prediction of thermal stresses during diamond cut-off grinding. Finite-element codes have been developed to implement the thermal stress model for numerical computation.

3.2.1 Mathematical Modeling

The grain-workpiece interaction, which generates heat flux in cut-off grinding, is shown in Fig. 2.2. To make the analysis of thermal stress tractable a number of simplifying assumptions are required to be made as follows:

Assumptions

1. A plane strain condition exists.
2. The material of workpiece is homogeneous, isotropic and linearly elastic-perfectly-plastic.
3. The yield point and thermal expansion coefficient are independent of temperature in contrast to real life situations.
4. A moving heat flux of uniform rectangular profile is used to find the temperature distribution.
5. No external forces act on the workpiece. Stresses occur only due to thermal expansion or contraction.
6. Inertia and body force effects are neglected.
7. The workpiece is assumed to be stress-free before grinding.

Temperature model

Temperature model discussed in section 2.2. (Fig. 2.3 and 2.4) is used to find the nodal temperatures in the workpiece domain.

Thermal stress model

The extreme temperature gradients that occur during cut-off grinding (in space and time) result in extreme nonuniformities in the local thermal expansion of workpiece material (strain) which lead to high thermal stresses. The transient temperature distribution in the workpiece, obtained by solving the heat conduction equation (Eq. 2.2) along with the boundary and initial conditions (Eq. 2.3 and 2.4), is used as input for the calculation of thermal stresses.

For thermal stresses due to cut-off grinding in a rectangular domain, the basic equations [76] and boundary conditions are as follows:

Equilibrium equations

The force equilibrium at a point leads to the following equilibrium equations

$$\frac{\partial \sigma_{xx}}{\partial x} + \frac{\partial \sigma_{xz}}{\partial z} = 0 \quad (3.1)$$

$$\frac{\partial \sigma_{xz}}{\partial x} + \frac{\partial \sigma_{zz}}{\partial z} = 0 \quad (3.2)$$

Stress-strain-temperature relations

The stress-strain-temperature relation for a linearly elastic material is

$$\{\sigma\} = [D] (\{\epsilon\} - \{m\}) \quad (3.3)$$

where, the stress vector $\{\sigma\}$, the strain vector $\{\epsilon\}$, the vector $\{m\}$ and the elasticity matrix $[D]$ are given by:

$$\{\sigma\}^T = \{\sigma_{xx}, \sigma_{zz}, \sigma_{xz}\} \quad (3.4)$$

$$\{\epsilon\}^T = \{\epsilon_{xx}, \epsilon_{zz}, \epsilon_{xz}\} \quad (3.5)$$

$$\{m\} = \begin{Bmatrix} 1 \\ 1 \\ 0 \end{Bmatrix} \frac{E \alpha_t \Delta T}{(1 - 2\nu)} \quad (3.6)$$

$$[D] = \frac{E}{(1 + \nu)(1 - 2\nu)} \begin{bmatrix} 1 - \nu & \nu & 0 \\ \nu & 1 - \nu & 0 \\ 0 & 0 & \frac{1 - 2\nu}{2} \end{bmatrix} \quad (3.7)$$

Here, E is young's modulus, ν is Poisson's ratio, α_t is coefficient of thermal expansion, and ΔT is temperature rise.

Plastic zone

To find the plastic zone, where the equivalent thermal stress is more than the material yield strength, the following expression for the deviatoric stress components are used.

$$\left. \begin{aligned} S_{xx} &= \sigma_{xx} - \frac{1}{3}(\sigma_{xx} + \sigma_{yy} + \sigma_{zz}) \\ S_{yy} &= \sigma_{yy} - \frac{1}{3}(\sigma_{xx} + \sigma_{yy} + \sigma_{zz}) \\ S_{zz} &= \sigma_{zz} - \frac{1}{3}(\sigma_{xx} + \sigma_{yy} + \sigma_{zz}) \\ S_{xz} &= \sigma_{xz} \end{aligned} \right\} \quad (3.8)$$

The equivalent (or effective) stress is given by

$$\sigma_{eq} = \sqrt{\frac{3}{2}(S_{xx}^2 + S_{yy}^2 + S_{zz}^2) + 2S_{xz}^2} \quad (3.9)$$

The points in plastic zone are calculated by using the condition

$$\sigma_{eq} \geq \sigma_y \text{ (plastic zone)} \quad (3.10)$$

Strain-displacement relations

For small deformation, the strain-displacement relations are given by

$$\varepsilon_{xx} = \frac{\partial u}{\partial x}, \quad \varepsilon_{zz} = \frac{\partial w}{\partial z}, \quad \varepsilon_{xz} = \left(\frac{\partial u}{\partial z} + \frac{\partial w}{\partial x} \right) \quad (3.11)$$

Boundary conditions

The domain of the problem with boundary conditions is shown in Fig. 3.1. Due to temperature effects, no rigid-body motion is allowed, but free expansion is possible. The bottom surface is not allowed to displace either in horizontal or in vertical direction.

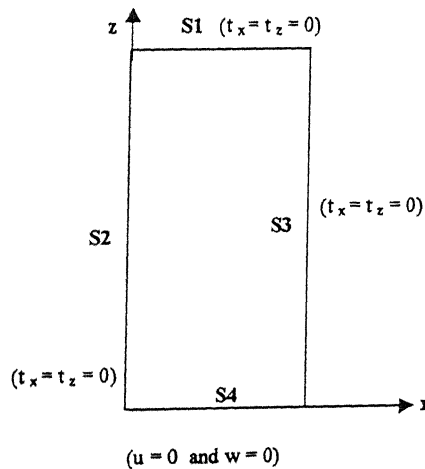


Fig. 3.1 Boundary conditions applied to workpiece domain used for finding thermal stresses in cut-off grinding

Thus,

$$u = 0 \text{ and } w = 0 \text{ at } z = 0 \quad (3.12)$$

Traction on top and side surfaces is assumed to be zero i.e.

$$t_x = t_z = 0 \quad (3.13)$$

The traction components t_x and t_z are related to the components of the stress tensor by the following relation:

$$t_i = \sigma_{ij} n_j \quad (3.14)$$

where, n_j are the components of the unit outward normal vector.

3.2.2 Finite Element Formulation

The finite element *Galerkin formulation* [73] is applied to convert the governing equations and boundary conditions to a set of algebraic equations. In this method, the displacements u and w are approximated by the some known functions. However, these approximations do not satisfy the equilibrium equations completely. The resulting error in them is made zero in an overall sense by using a set of functions W_x and W_z called weighting functions.

The resulting expression, called as the weighted residual integral, becomes

$$\int_{\Omega} \left[\left(\frac{\partial \sigma_{xx}}{\partial x} + \frac{\partial \sigma_{xz}}{\partial z} \right) W_x + \left(\frac{\partial \sigma_{xz}}{\partial x} + \frac{\partial \sigma_{zz}}{\partial z} \right) W_z \right] dx dz = 0 \quad (3.15)$$

Here, the weight functions are chosen to have the value zero on the boundary on which u and w are specified.

The use of divergence theorem leads to the following expression:

$$\int_{\Omega} \{ \nabla W \}^T \{ \sigma \} dx dz = 0 \quad (3.16)$$

Using the constitutive relation (equation 3.3-3.7), this expression becomes

$$\int_{\Omega} \{ \nabla W \}^T ([D] \{ \epsilon \} - \{ m \}) dx dz = 0 \quad (3.17)$$

In the present analysis, 2-D eight-noded isoparametric element is used for discretization of the domain. Thus, displacement is approximated as

$$\{u\} = [N^e] \{\delta\}^e \quad (3.18)$$

where,

$$[N^e] = \begin{bmatrix} N_1 & 0 & N_2 & 0 & N_3 & 0 & N_4 & 0 & N_5 & 0 & N_6 & 0 & N_7 & 0 & N_8 & 0 \\ 0 & N_1 & 0 & N_2 & 0 & N_3 & 0 & N_4 & 0 & N_5 & 0 & N_6 & 0 & N_7 & 0 & N_8 \end{bmatrix} \quad (3.19)$$

is the shape function matrix and $\{\delta\}^e$ is the nodal displacement vector given by

$$\{\delta\}^{eT} = \{u_1 \ w_1 \ u_2 \ w_2 \ u_3 \ w_3 \ u_4 \ w_4 \ u_5 \ w_5 \ u_6 \ w_6 \ u_7 \ w_7 \ u_8 \ w_8\} \quad (3.20)$$

Then the expression for strain becomes

$$\{\varepsilon\}^e = [B^e] \{\delta\}^e \quad (3.20)$$

where,

$$[B^e] = \begin{bmatrix} \frac{\partial N_1}{\partial x} & 0 & \frac{\partial N_2}{\partial x} & 0 & \frac{\partial N_3}{\partial x} & 0 & \frac{\partial N_4}{\partial x} & 0 & \frac{\partial N_5}{\partial x} & 0 & \frac{\partial N_6}{\partial x} & 0 & \frac{\partial N_7}{\partial x} & 0 & \frac{\partial N_8}{\partial x} & 0 \\ 0 & \frac{\partial N_1}{\partial z} & 0 & \frac{\partial N_2}{\partial z} & 0 & \frac{\partial N_3}{\partial z} & 0 & \frac{\partial N_4}{\partial z} & 0 & \frac{\partial N_5}{\partial z} & 0 & \frac{\partial N_6}{\partial z} & 0 & \frac{\partial N_7}{\partial z} & 0 & \frac{\partial N_8}{\partial z} \\ \frac{\partial N_1}{\partial z} & \frac{\partial N_1}{\partial x} & \frac{\partial N_2}{\partial z} & \frac{\partial N_2}{\partial x} & \frac{\partial N_3}{\partial z} & \frac{\partial N_3}{\partial x} & \frac{\partial N_4}{\partial z} & \frac{\partial N_4}{\partial x} & \frac{\partial N_5}{\partial z} & \frac{\partial N_5}{\partial x} & \frac{\partial N_6}{\partial z} & \frac{\partial N_6}{\partial x} & \frac{\partial N_7}{\partial z} & \frac{\partial N_7}{\partial x} & \frac{\partial N_8}{\partial z} & \frac{\partial N_8}{\partial x} \end{bmatrix} \quad (3.21)$$

For Galerkin method, we choose

$$\begin{Bmatrix} W_x \\ W_z \end{Bmatrix} = [N^e] \{W^e\} \quad (3.22)$$

where, $\{W^e\}$ contains the nodal values of the weight W_x and W_z . Then

$$\{\nabla W\} = [B^e] \{W^e\} \quad (3.23)$$

where, $\{W^e\}$ are the nodal weight values.

Substitution of expressions (3.18-3.23) in equation (3.17) leads to the following finite element equations

$$\sum_{e=1}^{nem} \{W^e\}^T [STK^e] \{\delta\}^e = \sum_{e=1}^{nem} \{W^e\}^T \{stf^e\} \quad (3.24)$$

where, elemental coefficient matrix for stresses $[STK^e]$ and elemental force vector for stresses $\{stf^e\}$ are given by

$$[STK^e] = \int_{\Omega^e} [B]^T [D] [B] dx dz \quad (3.25)$$

$$\{stf^e\} = \int_{\Omega^e} [B]^T \{m\} dx dz \quad (3.26)$$

Here, nem is the number of area elements and Ω^* is the domain of typical area element. The integrals in equations (3.25-3.26) are evaluated by 3×3 Gauss quadrature integration technique. While calculating $\{m\}$, the temperature at a gauss point is obtained using the same interpolation functions as used for the displacements.

The assembled finite element equations may be written as

$$[GGRINDK]\{GGRINDDU\} = \{GGRINDF\} \quad (3.27)$$

where, $[GGRINDK]$ is the global coefficient matrix, $\{GGRINDU\}$ is the global nodal displacements vector and $\{GGRINDF\}$ is the global right side vector for cut-off grinding. The final Eqs (3.27) are solved by Gauss-elimination method to find the nodal displacements after application of the displacement boundary conditions.

Evaluation of thermal stresses

As we have seen above, solution of the problem is obtained in the form of nodal displacements. From the nodal displacements, thermal stress at any point in an element is obtained by using Eq. (3.3). The equivalent stress is computed at each of the Gaussian integrating points and compared with the yield stress to identify whether yielding occurs or not (Eq. 3.10). This check is carried out for all the elements in the workpiece domain.

3.2.3 Results and Discussion

Present model has been applied to obtain the thermal stresses in HSS workpiece during cut-off grinding operation. The properties of HSS workpiece material are given in table 2.3.

Fig 3.2 shows the variation of components of thermal stresses at top surface with grinding time due to uniformly distributed rectangular heat source. The nature of σ_{xx} is compressive. The trend of σ_{xx} can be explained by analyzing the temperature and temperature gradient of a point at the centre of top surface ($x=0.003$ m) of the workpiece for varying time. The value of σ_{xx} is high for 0.1 s of grinding time because of high temperature (Fig. 3.3a) and also high temperature gradient with time from initial time to 0.1 s of grinding time (Fig. 3.3b). Further, the value of σ_{xx} decreases significantly with

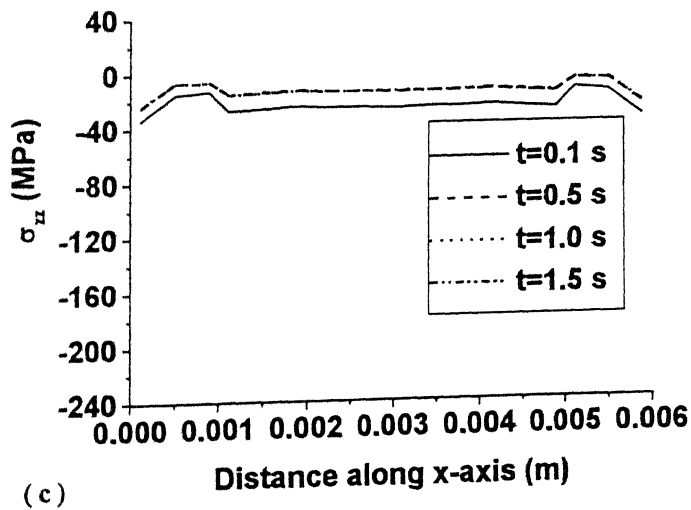
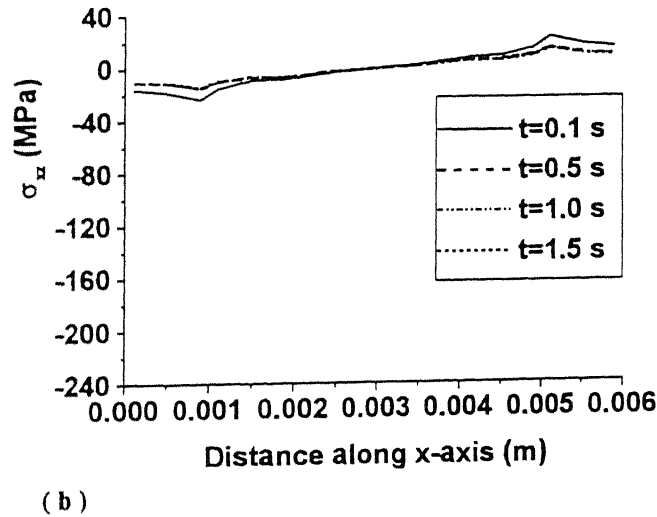
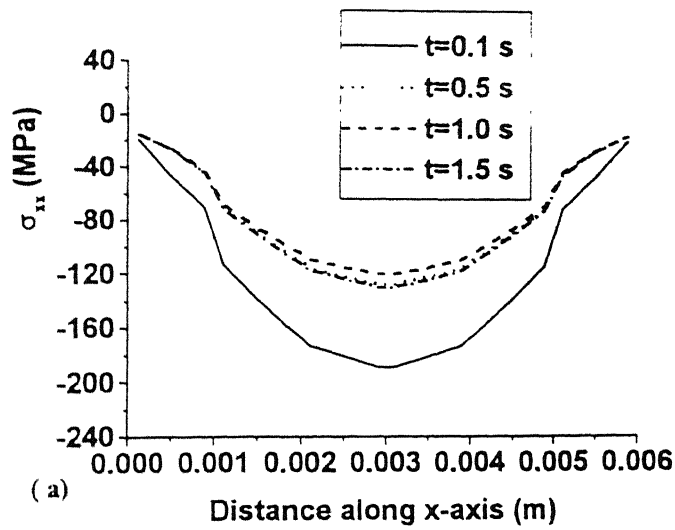


Fig. 3.2 Variation of (a) σ_{xx} (b) σ_{yy} (c) σ_{zz} with time at top surface during cut-

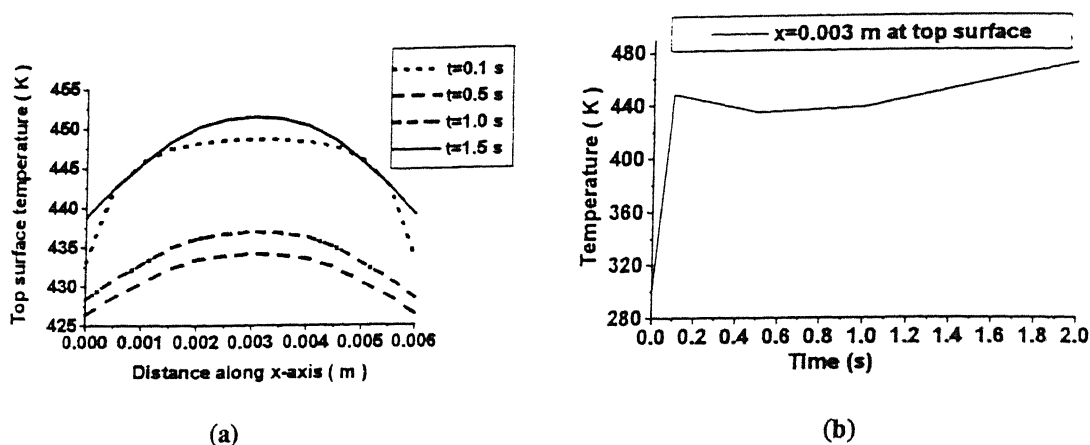
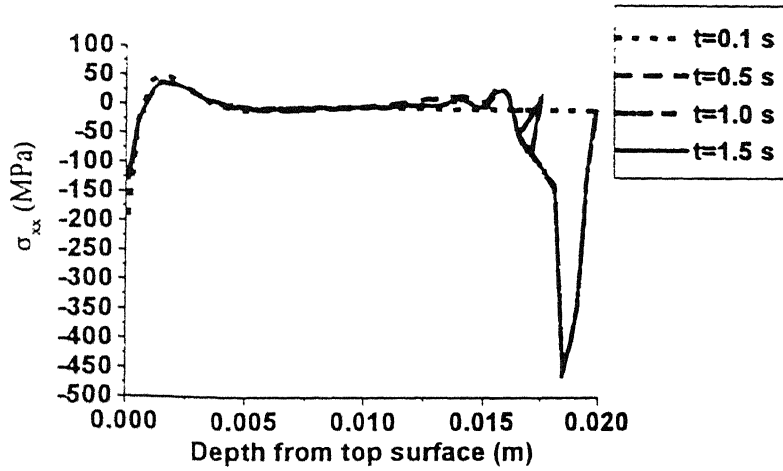


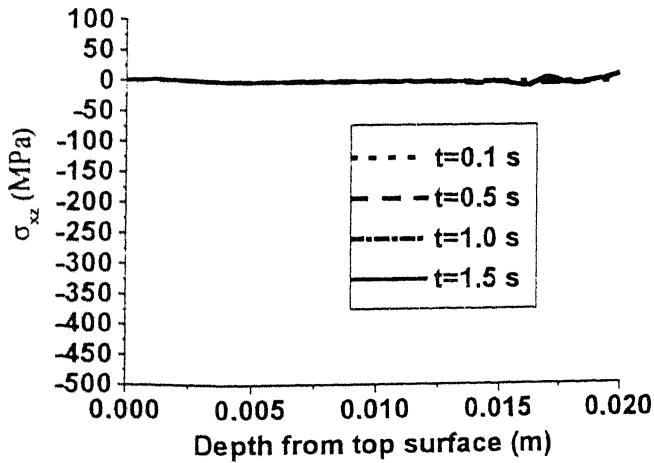
Fig. 3.3 (a) Top surface temperature variations with time (b) temperature variation of a point on top surface at $x=0.003$ m with time during cut-off grinding for $U_s = 10.55$ GPa, $R_{wg} = 0.08$ and $V_f = 10.29$ mm/s

increase in grinding time from 0.1 s to 0.5 s because of decrease in temperature gradient within this time interval (Fig. 3.3b). After 0.5 s of grinding time, temperature gradient is not changing significantly and hence the value of σ_{xx} is also not changing significantly (Fig. 3.3b and Fig. 3.2a). The peak value of σ_{xx} as 190 MPa after 0.01 s is decreased to 120 MPa after 1.5 s. The values of σ_{xz} and σ_{zx} are very small as compared to σ_{xx} (Fig. 3.2b and 3.2c).

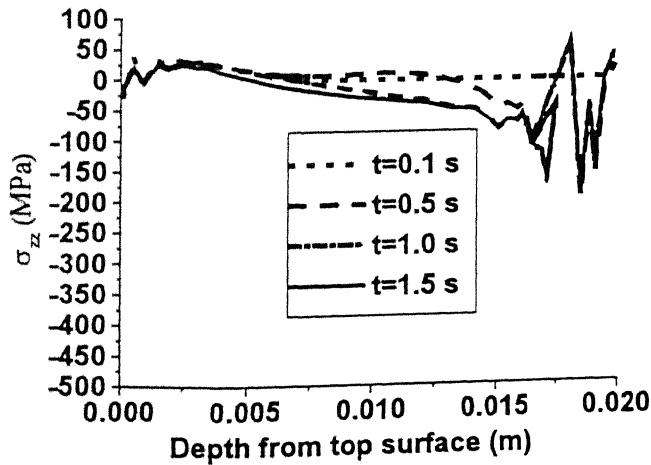
Fig. 3.4 shows the variation of thermal stresses along the depth with time. Here, the curves show that the non-uniformity in thermal stresses shifts from the top towards bottom with time of grinding. The trend of σ_{xx} (Fig. 3.4a) can be explained by analyzing the temperature and temperature gradient with time of two points, one near the top surface (depth=0.0015 m) and other near the bottom surface (depth=0.019 m) along the depth at the centre of the workpiece (Fig. 3.5a and 3.5b). The temperature gradient with time near the bottom is more between 0.1 s to 0.5 s (Fig. 3.5a and 3.5b) hence high value of σ_{xx} (Fig. 3.4a) is obtained. Further, increase in grinding time does not increase the temperature gradient significantly and hence no further change in the value of σ_{xx} is obtained. Near the top surface, temperature gradient is high till 0.1 s of grinding time but



(a)



(b)



(c)

Fig. 3.4 Variation of (a) σ_{xx} (b) σ_{yy} (c) σ_{zz} with time along depth at the centre of HSS workpiece during cut-off grinding for $V_f=10.29$ mm/s, $R_{wg}=0.08$, $U_o=10.55$ GPa

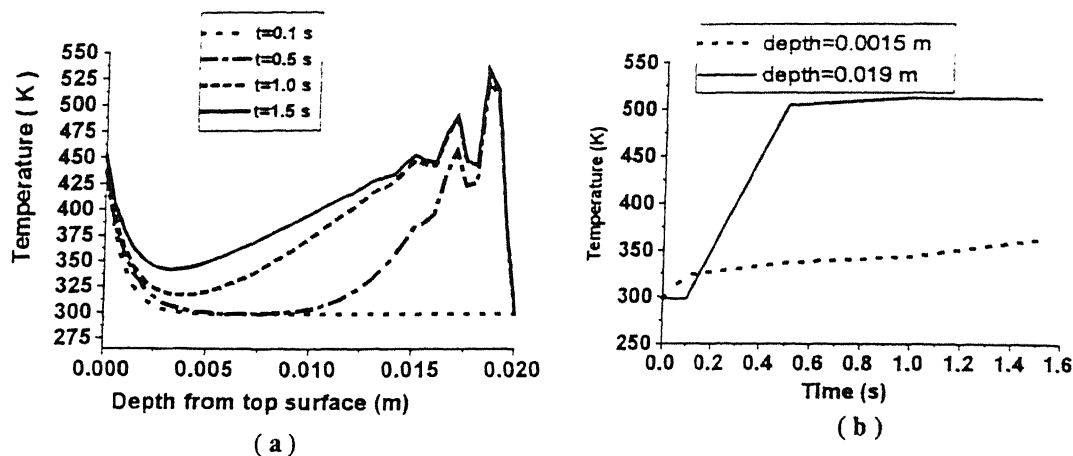


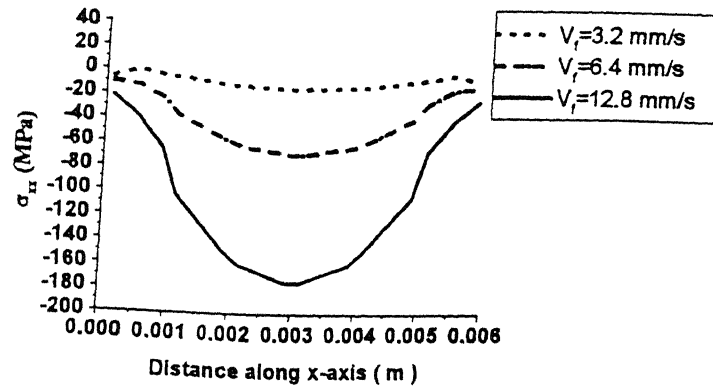
Fig. 3.5 (a) Depthwise temperature variations with time (b) temperature variation of two points at different depths with time during cut-off grinding for $x=0.003$ m, $U_o=10.55$ GPa, $R_{wg}=0.08$ and $V_f=10.29$ mm/s

its numerical value (approximately 250 MPa/s) is much less than the maximum value near the bottom surface (500 MPa/s, $\text{depth}=0.019$ m in Fig. 3.5b). The maximum values of components of thermal stresses developed either at the top surface or along the depth are less than the yield strength of workpiece material (3610 MPa).

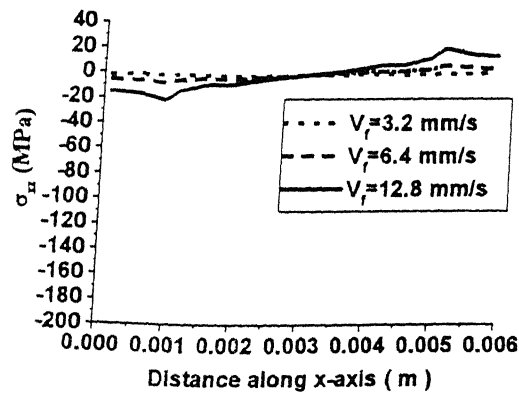
An important controllable parameter in cut-off grinding is feed given to the workpiece (Eq. 2.1) hence the effect of feed on variation of components of thermal stresses are analyzed as shown in fig 3.6-3.7.

Fig. 3.6 shows the variations of different components of thermal stresses with feed along top surface after grinding 5 mm depth of the workpiece. Here, it is observed that the nature of σ_{xx} is compressive and varying with feed. Higher values of σ_{xx} are obtained at higher feeds because of high temperature rise at top surface with higher feeds due to increase in q_{wg} (Eq. 2.1). The trends of σ_{xx} and σ_{zz} are also shown, but their quantitative values are very small (Fig. 3.6b and 3.6c) compared to σ_{xx} .

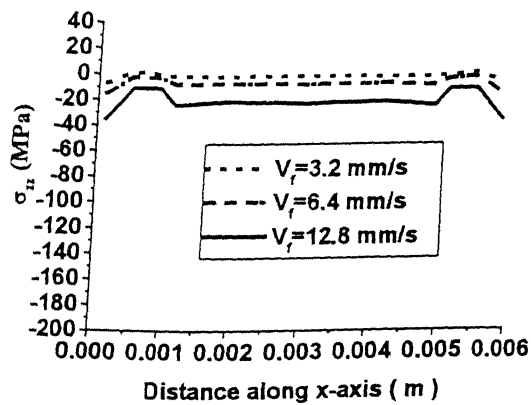
Fig. 3.7 shows the variations of different components of thermal stresses with feed along the depth at the centre of the workpiece after grinding 5 mm depth. Here, it is observed that the thermal stress component σ_{xx} varies with feed either near the top or



(a)

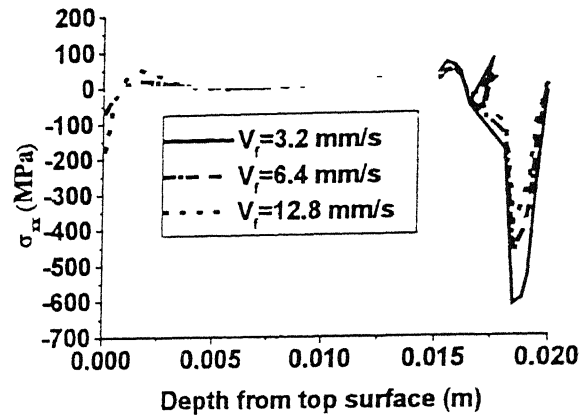


(b)

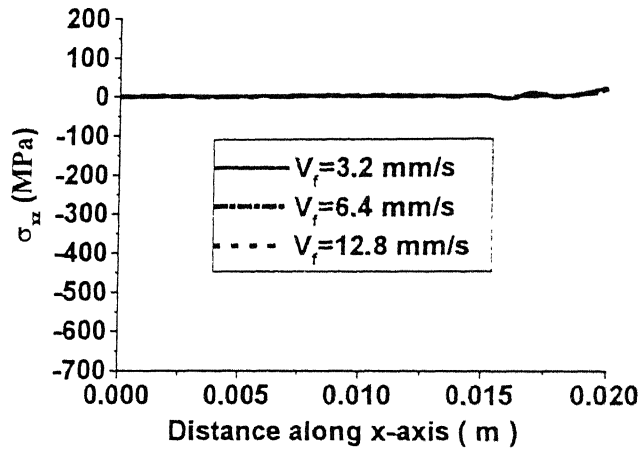


(c)

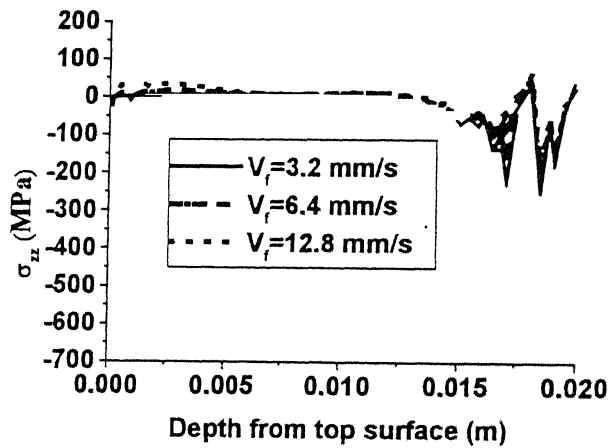
Fig. 3.6 Variation of (a) σ_{xx} (b) σ_{yy} and (c) σ_{zz} at top surface with V_r during cut-off grinding of HSS workpiece for $R_{wg}=0.08$, $U_o=10.55$ GPa, and machined depth 5 mm



(a)



(b)



(c)

Fig. 3.7 Variation of (a) σ_{xx} (b) σ_{xx} and (c) σ_{xx} along depth at $x=0.003$ m with V_f during cut-off grinding of HSS workpiece for $R_{\text{max}}=0.08$, $H=10.55$ GPa and

near the bottom surface (Fig 3.7a) Maximum increase of about 200 MPa in σ_{xx} is noted near the bottom surface, by four-fold increase in feed (3.2 mm/s to 12.8 mm/s). Almost no change of σ_{yy} and σ_{zz} are noted with this change in feed (Fig 3.7b and 3.7c).

3.3 Thermal Stresses in EDM

High temperature generated due to high-density discharge thermal energy leads to not only thermal erosion but also formation of recast layer with micro-cracks on the machined surface. The presence of multi-layered heat affected zone and brittleness of the hardened layer have been reported [84-85] to reduce the fatigue strength of electro-discharge machined components. The computation of the temperature and thermal stress fields in the workpiece, therefore, is of considerable importance as far as surface integrity is concerned.

Few available surface integrity models due to EDM are mainly based on metallurgical examinations of EDM'd surfaces using various experimental techniques such as optical metallography, scanning electron microscopy, X-ray diffraction [84, 86-88]. Lee et al. [87] have found the extent of surface damage with respect to more readily measured parameters such as pulse energy, and surface roughness. Kruth et al. [84] have studied the influence of workpiece material, electrode material and dielectric type on the composition and the metallographic phase of the white layer. However, there are very few theoretical approaches for determination of thermal stresses.

Since the thermal action of EDM process affects the surface integrity of machined component, the analysis of temperature distribution is required for prediction of thermal stresses. Thermal stresses generated due to such a non-uniform temperature distribution can be analyzed for finding thermal residual stresses in the workpiece, which have direct relationship to the quality of the machined surfaces.

In this section, a thermal stress model has been developed based on the finite element technique. Discharge current, pulse time, duty cycle, and spark radius are considered to be the main parameters affecting the thermal stresses. The principal aim of developing this model is to predict the nature of thermal stresses occurring during EDM.

3.3.1 Mathematical Modeling

In EDM, two electrodes namely workpiece and tool, are dipped in liquid dielectric (kerosene) and physically separated by a gap, called inter-electrode gap. Due to random and complex nature of EDM process, the following assumptions are made to make the problem mathematically tractable.

Assumptions

1. The domain is considered as axisymmetric.
2. The workpiece material is assumed to be homogeneous and isotropic.
3. The material properties of the workpiece are temperature independent.
4. The heat transfer to the workpiece is by conduction.
5. Inertia and body force effects are negligible during stress development
6. The workpiece material is elastic-perfectly plastic and yield stress in tension is same as that in compression.
7. The workpiece is assumed as stress-free before electro-discharge machining
8. Thermal stresses are evaluated only upto the time for which the transient temperature distribution is known.

Temperature model

Temperature model of EDM discussed in section 2.3 is used to find nodal temperature distribution within workpiece domain.

Thermal stress model

The extreme temperature gradients that occur during EDM (in space and time) result in extreme non-uniformities in the local thermal expansion of workpiece material (strain) which lead to high thermal stresses. The transient temperature distribution in the workpiece, obtained by solving the heat conduction equation (Eq. 2.45) along with the boundary and initial conditions, is used as input for the calculation of thermal stresses.

For the axisymmetric thermal stress analysis problem at hand, basic equations and boundary conditions are given below [76].

Equilibrium equations:

The force equilibrium at a point leads to the following equilibrium equations

$$\frac{\partial \sigma_{rr}}{\partial r} + \frac{\partial \sigma_{rz}}{\partial z} + \frac{\sigma_{rr} - \sigma_{\theta\theta}}{r} = 0 \quad (3.28)$$

$$\frac{\partial \sigma_{rz}}{\partial r} + \frac{\partial \sigma_{zz}}{\partial z} + \frac{\sigma_{rz}}{r} = 0 \quad (3.29)$$

where, σ_{rr} , $\sigma_{\theta\theta}$ and σ_{zz} are normal stresses and σ_{rz} is shear stress.

Strain-displacement relations:

For small deformation, the strain-displacement relations in an axisymmetric domain are given by

$$\epsilon_{rr} = \frac{\partial u}{\partial r}, \quad \epsilon_{\theta\theta} = \frac{u}{r}, \quad \epsilon_{zz} = \frac{\partial w}{\partial z}, \quad \epsilon_{rz} = \frac{\partial u}{\partial z} + \frac{\partial w}{\partial r} \quad (3.30)$$

where ϵ_{rr} , $\epsilon_{\theta\theta}$ and ϵ_{zz} are normal strains and ϵ_{rz} is shear strain. Displacements along r and z -axis are u and w , respectively.

Constitutive relations:

The stress-strain-temperature can be written as:

$$\{\sigma\} = [D]\{\epsilon\} - \{m\} \quad (3.31)$$

The stress vector $\{\sigma\}$, the strain vector $\{\epsilon\}$, the vector $\{m\}$ and the elasticity matrix $[D]$ are given by:

$$\{\sigma\}^T = \{\sigma_{rr}, \sigma_{\theta\theta}, \sigma_{zz}, \sigma_{rz}\} \quad (3.32)$$

$$\{\epsilon\}^T = \{\epsilon_{rr}, \epsilon_{\theta\theta}, \epsilon_{zz}, \epsilon_{rz}\} \quad (3.33)$$

$$\{m\} = \begin{Bmatrix} 1 \\ 1 \\ 1 \\ 0 \end{Bmatrix} \frac{E\alpha_t \Delta T}{1-2\nu} \quad (3.34)$$

$$[D] = \frac{E}{(1+\nu)(1-2\nu)} \begin{bmatrix} 1-\nu & \nu & \nu & 0 \\ \nu & 1-\nu & \nu & 0 \\ \nu & \nu & 1-\nu & 0 \\ 0 & 0 & 0 & \frac{1-2\nu}{2} \end{bmatrix} \quad (3.35)$$

Here, E is young's modulus, ν is Poisson's ratio, α is coefficient of thermal expansion, and ΔT is temperature rise.

Plastic zone:

To find the plastic zone, where the equivalent thermal stress is more than the material yield strength, the following expression for the deviatoric stress components are used

$$\begin{aligned} S_{rr} &= \sigma_{rr} - \frac{1}{3}(\sigma_{rr} + \sigma_{zz} + \sigma_{\theta\theta}) \\ S_{\theta\theta} &= \sigma_{\theta\theta} - \frac{1}{3}(\sigma_{rr} + \sigma_{zz} + \sigma_{\theta\theta}) \\ S_{zz} &= \sigma_{zz} - \frac{1}{3}(\sigma_{rr} + \sigma_{zz} + \sigma_{\theta\theta}) \\ S_{rz} &= \sigma_{rz} \end{aligned} \quad (3.36)$$

The equivalent (or effective) stress is given by

$$\sigma_{eq} = \sqrt{\frac{3}{2} (S_{rr}^2 + S_{\theta\theta}^2 + S_{zz}^2) + 2S_{rz}^2} \quad (3.37)$$

where, a point in plastic zone is identified by the following inequality:

$$\sigma_{eq} \geq \sigma_y \text{ (plastic zone)} \quad (3.38)$$

Boundary conditions:

The traction components t_r and t_z (mechanical stresses) are related to the components of the stress tensor by the following relation:

$$t_i = \sigma_{ij} n_j \quad (3.39)$$

where, n_j are the components of the unit outward normal vector.

Equations 3.28-3.29 are a set of elliptic equations in unknown displacements u and w , thus requiring boundary conditions along the boundary surface of the domain under consideration. The domain of the workpiece with boundary conditions is shown in Fig. 3.8.

Displacements along and across surface AD are assumed zero.

$$u = 0 \text{ and } w = 0 \quad \text{on AD} \quad (3.40a)$$

Since AB is an axis of symmetry, the normal component of displacement vector and shear component of traction vector are zero along the boundary. Thus,

$$u = 0, \quad t_z = 0 \quad \text{on AB} \quad (3.40b)$$

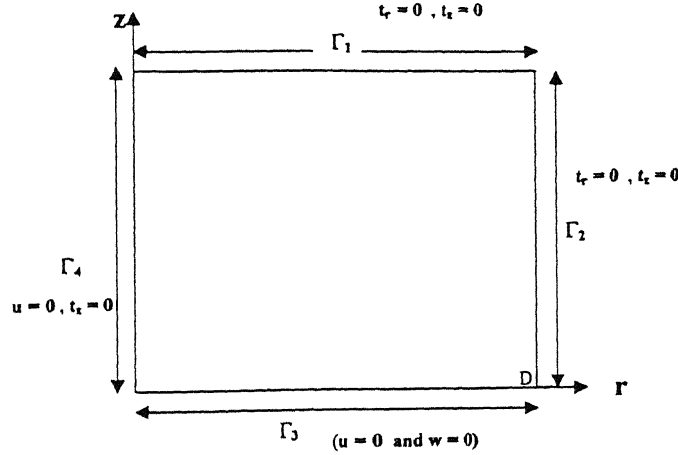


Fig. 3.8 Boundary conditions applied to workpiece domain used for finding thermal stresses in EDM

Furthermore, since BC is a free surface, both the traction components are zero on this boundary. Finally, the boundary CD is considered sufficiently far away from the heat source so as to be stress free. Thus, the boundary conditions on BC and CD are:

$$t_r = 0, \quad t_z = 0 \quad \text{on BC and CD} \quad (3.40c)$$

3.3.2 Finite Element Formulation

The finite element *Galerkin formulation* (73) is applied to convert the governing equations and boundary conditions to a set of algebraic equations. In this method, the displacements u and w are approximated by some known function. However, these approximations do not satisfy the equilibrium Eqs. (3.28-3.29). The resulting error in them is made zero in an overall sense by using a set of functions W_r and W_z , called as weighting functions.

The resulting expression called as the weighted residual integral, becomes

$$\int_{\Omega} \left[\left(\frac{\partial \sigma_{rr}}{\partial r} + \frac{\partial \sigma_{rz}}{\partial z} + \frac{\sigma_{rr} - \sigma_{\theta\theta}}{r} \right) W_r + \left(\frac{\partial \sigma_{rz}}{\partial r} + \frac{\partial \sigma_{zz}}{\partial z} + \frac{\sigma_{rz}}{r} \right) W_z \right] 2\pi r dr dz = 0 \quad (3.41)$$

Here, the weight functions are chosen to have the zero value on the boundary at which u and w are specified.

The use of divergence theorem leads to the following expression:

$$\int_{\Omega} \{\nabla W\}^T \{\sigma\} 2\pi r dr dz = 0 \quad (3.42)$$

Using the constitutive relation (3.31), we can write

$$\int_{\Omega} \{\nabla W\}^T ([D]\{\epsilon\} - \{m\}) 2\pi r dr dz = 0 \quad (3.43)$$

In the present analysis, 2-D eight noded isoparametric elements are used (Fig. 2.14). Thus, the displacement is to be approximated as

$$\{u\} = [N^e] \{\delta\}^e \quad (3.44)$$

where,

$$[N^e] = \begin{bmatrix} N_1 & 0 & N_2 & 0 & N_3 & 0 & N_4 & 0 & N_5 & 0 & N_6 & 0 & N_7 & 0 & N_8 & 0 \\ 0 & N_1 & 0 & N_2 & 0 & N_3 & 0 & N_4 & 0 & N_5 & 0 & N_6 & 0 & N_7 & 0 & N_8 \end{bmatrix} \quad (3.45)$$

is the shape function matrix and $\{\delta\}^e$ is the nodal displacement vector given by

$$\{\delta\}^e T = \{u_1 \ w_1 \ u_2 \ w_2 \ u_3 \ w_3 \ u_4 \ w_4 \ u_5 \ w_5 \ u_6 \ w_6 \ u_7 \ w_7 \ u_8 \ w_8\} \quad (3.46)$$

Then, the strain vector is given by

$$\{\epsilon\} = [B^e] \{\delta\}^e \quad (3.47)$$

where,

$$[B^e] = \begin{bmatrix} \frac{\partial N_1}{\partial r} & 0 & \frac{\partial N_2}{\partial r} & 0 & \frac{\partial N_3}{\partial r} & 0 & \frac{\partial N_4}{\partial r} & 0 & \frac{\partial N_5}{\partial r} & 0 & \frac{\partial N_6}{\partial r} & 0 & \frac{\partial N_7}{\partial r} & 0 & \frac{\partial N_8}{\partial r} & 0 \\ \frac{N_1}{r} & 0 & \frac{N_2}{r} & 0 & \frac{N_3}{r} & 0 & \frac{N_4}{r} & 0 & \frac{N_5}{r} & 0 & \frac{N_6}{r} & 0 & \frac{N_7}{r} & 0 & \frac{N_8}{r} & 0 \\ 0 & \frac{\partial N_1}{\partial z} & 0 & \frac{\partial N_2}{\partial z} & 0 & \frac{\partial N_3}{\partial z} & 0 & \frac{\partial N_4}{\partial z} & 0 & \frac{\partial N_5}{\partial z} & 0 & \frac{\partial N_6}{\partial z} & 0 & \frac{\partial N_7}{\partial z} & 0 & \frac{\partial N_8}{\partial z} \\ \frac{\partial N_1}{\partial z} & \frac{\partial N_1}{\partial r} & \frac{\partial N_2}{\partial z} & \frac{\partial N_2}{\partial r} & \frac{\partial N_3}{\partial z} & \frac{\partial N_3}{\partial r} & \frac{\partial N_4}{\partial z} & \frac{\partial N_4}{\partial r} & \frac{\partial N_5}{\partial z} & \frac{\partial N_5}{\partial r} & \frac{\partial N_6}{\partial z} & \frac{\partial N_6}{\partial r} & \frac{\partial N_7}{\partial z} & \frac{\partial N_7}{\partial r} & \frac{\partial N_8}{\partial z} & \frac{\partial N_8}{\partial r} \end{bmatrix} \quad (3.48)$$

For Galerkin method, we choose

$$\begin{Bmatrix} W_r \\ W_z \end{Bmatrix} = [N^e] \{W^e\} \quad (3.49)$$

where, $\{W^e\}$ contains the nodal values of the weight W_r and W_z . Then

$$\{\nabla W\} = [B] \{W^e\} \quad (3.50)$$

Substitution of expressions (3.44-3.50) in equation (3.43) leads to the following finite element equations

$$\sum_{e=1}^{nem} \{W^e\}^T [STK^e] \{\delta\}^e = \sum_{e=1}^{nem} \{W^e\}^T \{stf^e\} \quad (3.51)$$

where, elemental coefficient matrix for stresses $[STK^e]$ and elemental force vector for stresses $\{stf^e\}$ are given by

$$[STK^e] = \int_{\Omega^e} [B]^T [D] [B] r dr dz \quad (3.52)$$

$$\{stf^e\} = \int_{\Omega} [B]^T \{m\} r dr dz \quad (3.53)$$

Here, nem is the number of area elements and Ω^e is the domain of typical area element. The integrals in equations (3.52) and (3.53) are evaluated by 3*3 Gauss quadrature integration technique. While calculating $\{m\}$, the temperature at Gauss point is obtained using the same interpolation functions as used for the displacements.

The assembled finite element equations may be written as

$$[GEDMK] \{GEDMU\} = \{GEDMF\} \quad (3.54)$$

where, $[GEDMK]$ is the global coefficient matrix, $\{GEDMU\}$ is the global nodal displacements vector and $\{GEDMF\}$ is the global right side vector. The final equations (3.54) are solved by Gauss-elimination method to find nodal displacements after application of boundary conditions.

Evaluation of Thermal Stresses:

As we have seen above, solution of the problem is obtained in the form of nodal displacements. From the nodal displacements, thermal stresses at any point in an element are obtained by using Eq. 3.31. The equivalent stress (Eq. 3.37) is computed at each of the Gaussian integrating points and compared with the yield stress to identify whether yielding occurs or not. This check is carried out for all the elements.

3.3.3 Results and Discussion

Present model has been applied to obtain thermal stresses in EDM operation. The properties of HSS workpiece material are given in table 2.3. The typical stress

distributions in EDM are presented first. Later, a parametric study of stress distributions is presented by varying the two parameters, i.e. duty factor and current.

The thermal stress components are computed for each of the Gaussian integrating points within each element of the discretized domain (Fig. 2.14). All the Gauss points which are near the top surface of the considered domain and element size are found to be at $7\text{ }\mu\text{m}$ below the top surface of the domain. Similarly, all the Gauss points which lie near the center line of the spark are found to be $7\text{ }\mu\text{m}$ away from the center line. Hence, typical planes, which are near to the spark, are chosen to show the results of stress distributions along the radius and along the depth for parametric study (Fig. 3.9 and Fig. 3.12-3.15).

Fig 3.9(a) shows the variation of thermal stresses along the radial distance at $7\text{ }\mu\text{m}$ below the top surface. It is noticed that a compressive stress region exists near the spark center ($r = 0$). The compressive nature of the stress components can be explained as follows. A part of the workpiece material under a spark expands more significantly due to higher temperature rise and causes compressive stresses because of the restraint from the material that expands less. Radial component (σ_{rr}) is seen to be highest closely followed by tangential component ($\sigma_{\theta\theta}$). At the center, the values of each of these two components is 2750 MPa while that of σ_{zz} is only 650 MPa . The shear component (σ_{rz}) (120 MPa) is much smaller compared to the other three components, and its sign changes a little away from the center of the spark. Almost no thermal stresses are observed beyond $400\text{ }\mu\text{m}$ away from the center.

Fig 3.9(b) shows the variation of thermal stresses along the depth. It is observed that the stress fields are tensile also in almost all cases. These curves also show that the undesired tensile thermal stresses are critical near the top surface. They are varying upto $100\text{ }\mu\text{m}$ but gradually become zero beyond $400\text{ }\mu\text{m}$. The more critical component is σ_{zz} which varies from -675 MPa to $+1300\text{ MPa}$ within $100\text{ }\mu\text{m}$ of depth. This shows that σ_{zz} will cause very high thermal residual stresses near the top surface.

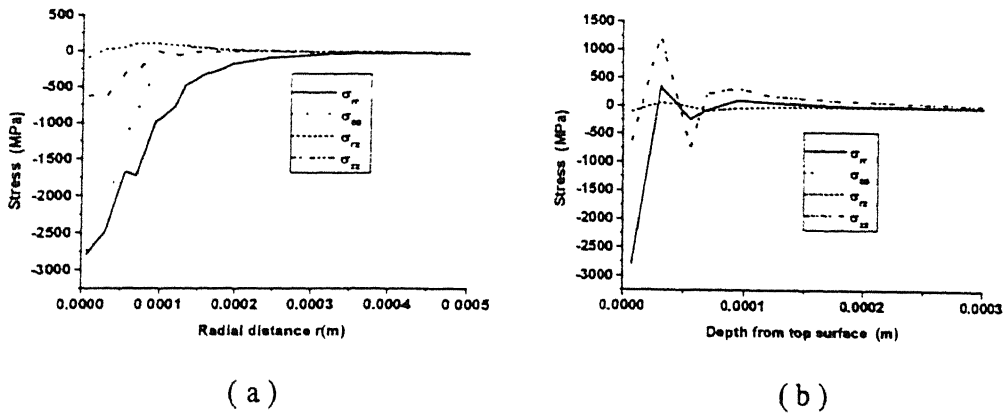


Fig. 3.9 Variation of stress components in HSS workpiece for $U_b = 40$ V, $I = 8$ A, $R_w = 0.08$, $R = 125$ μm , $t_{on} = 100$ μs , duty cycle = 50%. Results after 100 μs (a) along the radial distance at 7 μm below from the top surface, (b) along depth at $r = 7$ μm

The zone where thermal stresses exceed the yield strength (Eq. 3.37) is determined after finding equivalent stress. The contours of equivalent thermal stress are shown in Fig. 3.10. The region starting from the curve with $\sigma_{eq} > 3610$ MPa (near to 3500 MPa curve in Fig. 3.10) moving towards the center of the spark would be under plastic condition where the stress will be greater than the yield strength of the workpiece (3610 MPa). But, the region near the spark where temperature is more than the melting temperature of the workpiece material (1935 K) (Fig. 3.11) is in molten state, and it is assumed that whole of the molten material gets ejected out. Therefore, no thermal stresses are developed in this region (Fig. 3.11) where workpiece temperature > 1935 K.

Fig. 3.12 shows the effect of duty cycle on the thermal stress distribution along the radial distance. Details of on-time (t_{on}) and off-time (t_{off}) corresponding to each duty cycle is given in table 3.1. The curves clearly show that the radial and tangential stress components (σ_r and σ_θ) increase with the increase in duty cycle value (Fig. 3.12a and 3.12b). This is so because of the fact that heat supplied to the workpiece due to a spark is more with larger duty cycle and hence more temperature rise. Variation of radial stress component takes place upto 500 μm (Fig. 3.12a) where as change in σ_θ is only upto 175 μm (Fig. 3.12b). Also, it is interestingly noted that shear stresses are changing their sign

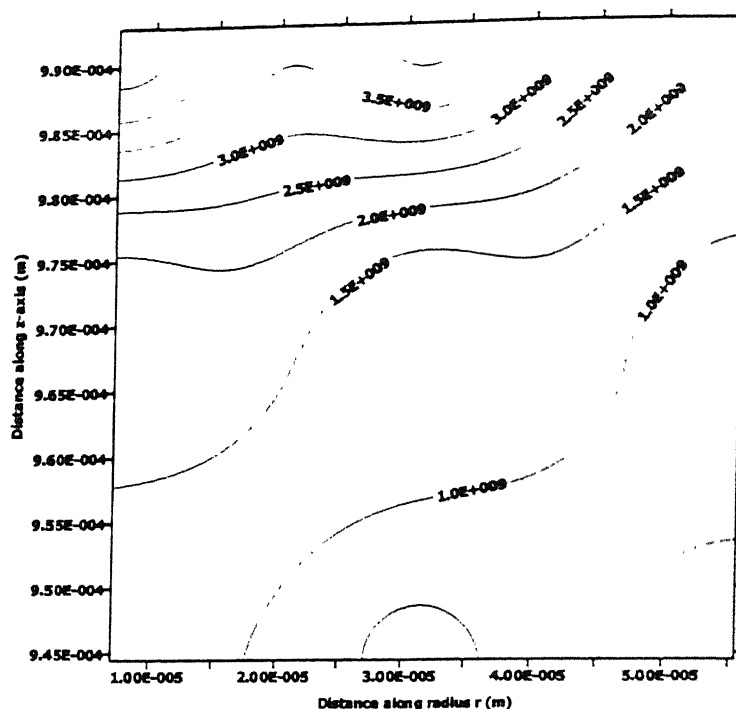


Fig. 3.10 Equivalent isostress (N/m^2) due to one spark within $R/2$ from the center (within one critical element) in HSS workpiece at $U_b = 40$ V, $I = 8$ A, $R_w = 0.08$, $R = 125$ μm , $t_{on} = 100$ μs , duty cycle = 50%

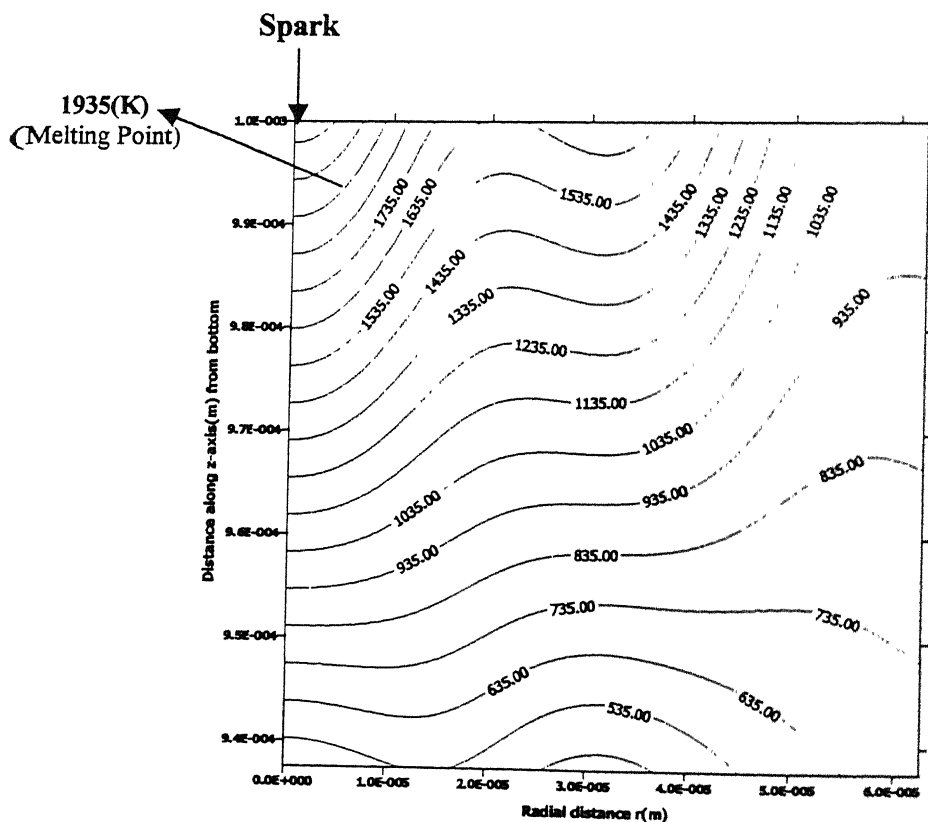


Fig. 3.11 Isotherms ($^{\circ}\text{K}$) due to one spark within $R/2$ from the centre (within one critical element) in HSS workpiece at $U_b = 40$ V, $I = 8$ A, $R_w = 0.08$, $R = 125$ μm , $t_{on} = 100$ μs , duty cycle = 50%. Results after 100 μs .

within 200 μm (Fig. 3.12c). Almost no variation of σ_{zz} is observed with duty cycle (Fig. 3.12d). Variation of stress components with duty cycle along the depth is shown in Fig. 3.13. Here, it is noted that σ_{rz} and σ_{zz} are not changing with increase in duty cycle, while other two are slightly changing.

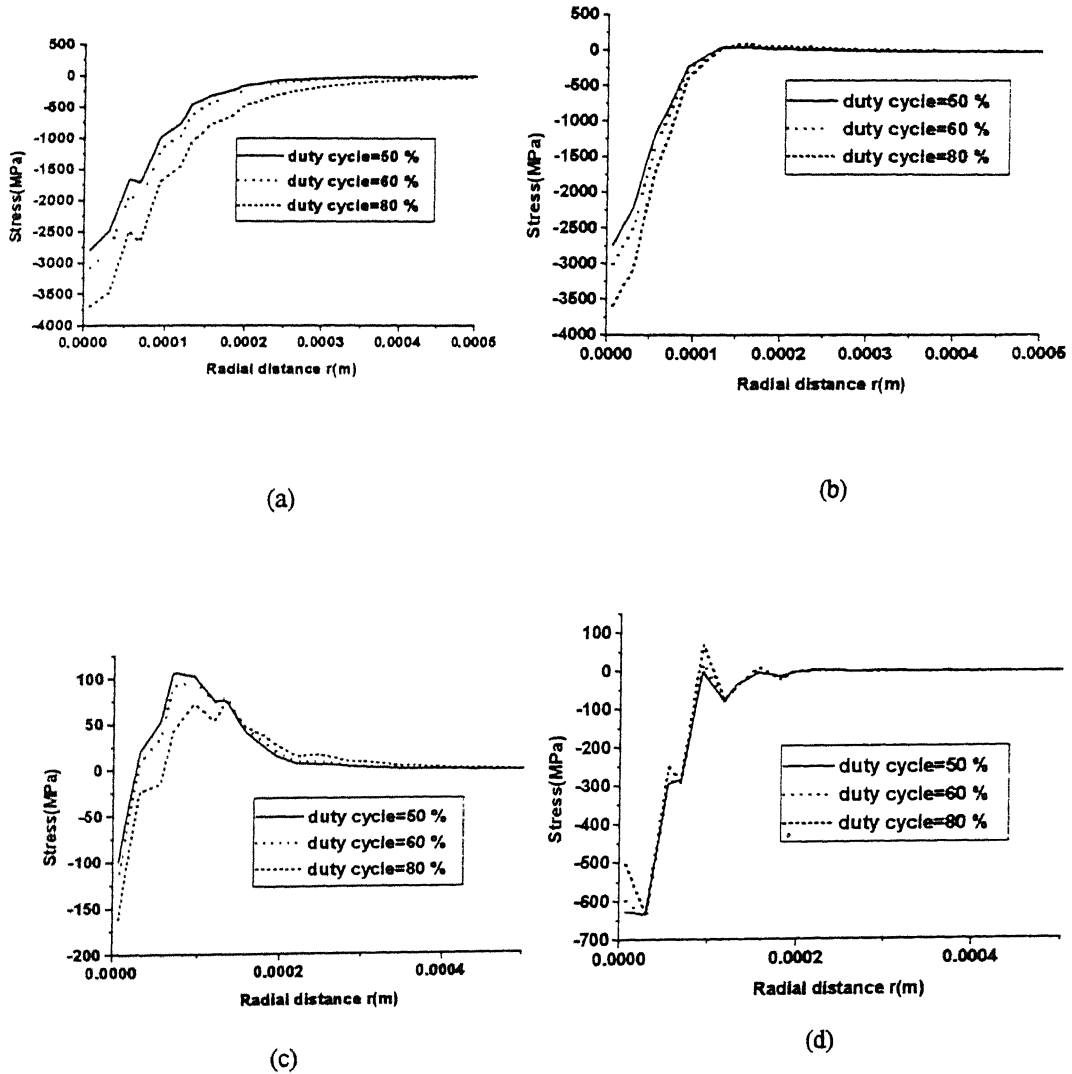
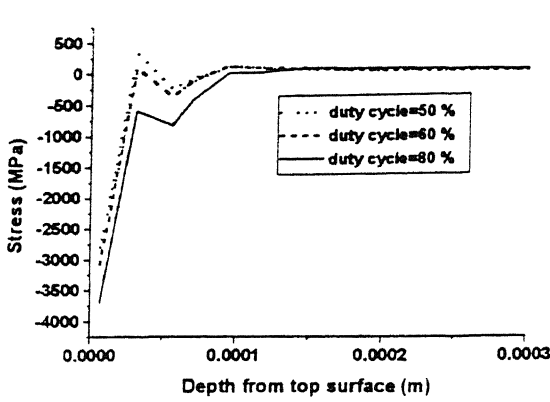


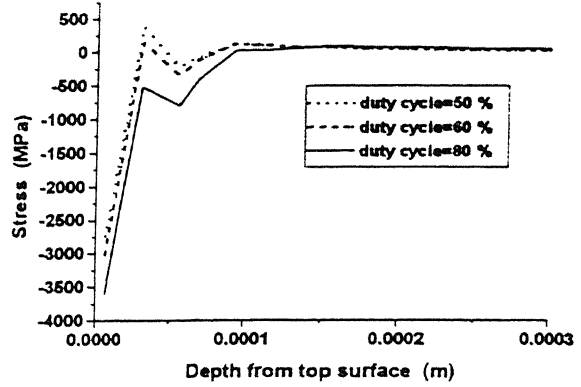
Fig. 3.12 Variation of stress components with duty cycle along depth in HSS workpiece at $r = 7 \mu\text{m}$ from the center of the spark for $U_b = 40 \text{ V}$, $I = 8 \text{ A}$, $R_w = 0.08$, $R = 125 \mu\text{m}$, $t_{\text{off}} = 100 \mu\text{s}$ (a) σ_{rr} , (b) $\sigma_{\theta\theta}$, (c) σ_{rz} , (d) σ_{zz} . Results after one on-time

Table 3.1 Details of on-time, off-time and pulse time for different duty cycle

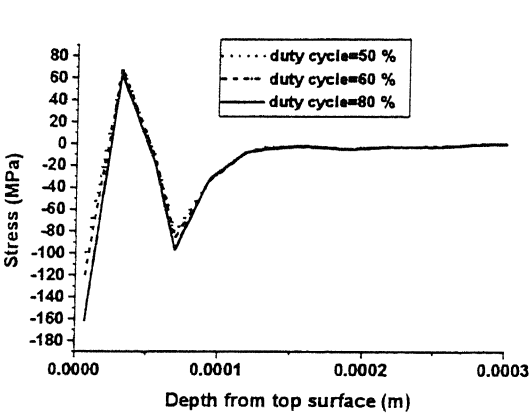
Duty Cycle ((on-time/pulse time)*100)	On-time (μs)	Off-time (μs)	Pulse time (μs)
50 %	100	100	200
60 %	150	100	250
80 %	400	100	500



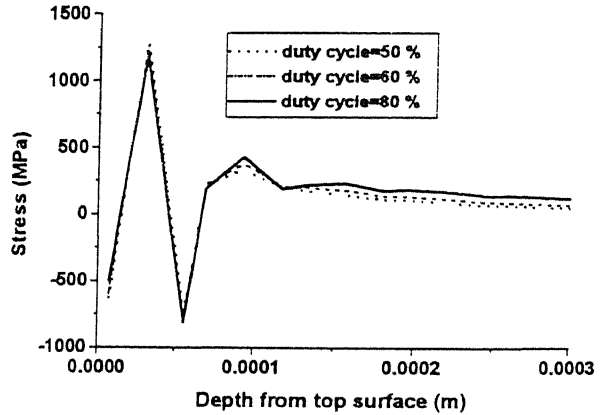
(a)



(b)



(c)



(d)

Fig. 3.13 Variation of stress components with duty cycle along depth in HSS workpiece at $r = 7 \mu\text{m}$ from the center of the spark for $U_b = 40 \text{ V}$, $I = 8 \text{ A}$, $R_w = 0.08$, $R = 125 \mu\text{m}$, $t_{\text{off}} = 100 \mu\text{s}$ (a) σ_{rr} (b) $\sigma_{\theta\theta}$ (c) σ_{rz} (d) σ_{zz} . Results after one spark on-time.

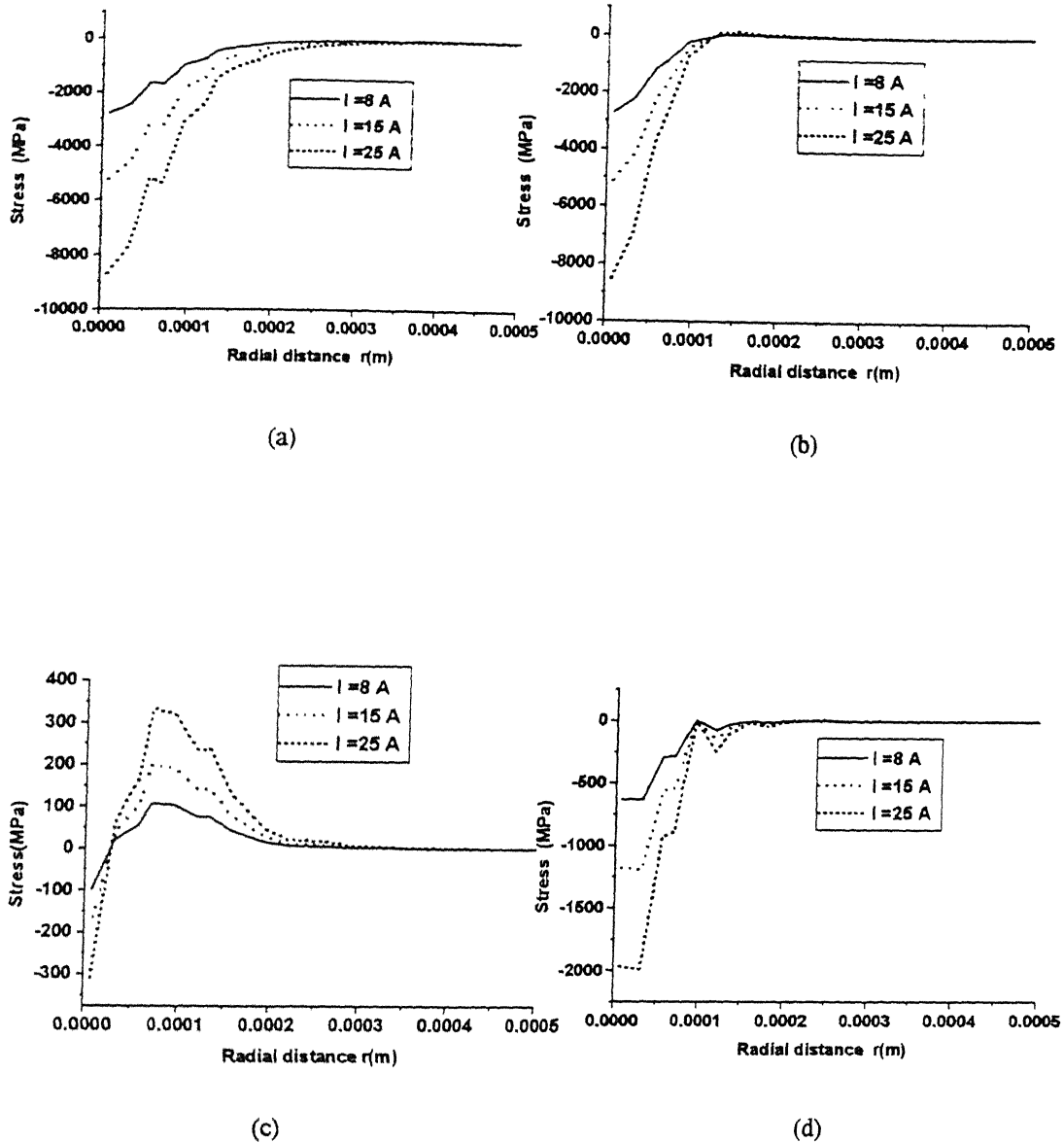


Fig. 3.14 Variation of components of thermal stresses with current along radius in HSS workpiece at $7 \mu\text{m}$ below from the top surface for $U_b = 40$ V, $I = 8$ A, $R_w = 0.08$, $R = 125 \mu\text{m}$, $t_{off} = 100 \mu\text{s}$, duty cycle = 50% (a) σ_{rr} , (b) $\sigma_{\theta\theta}$, (c) $\sigma_{\tau\tau}$, (d) σ_{zz} . Results after $100 \mu\text{s}$.

The effect of current on the thermal stress distribution along the radial distance is shown in Fig. 3.14. When the current is high, the induced radial, tangential and transverse components of thermal stresses are also high and compressive in nature (Fig. 3.14a, 3.14b, and 3.14d). In fact, the increase in temperature rise is directly proportional to the

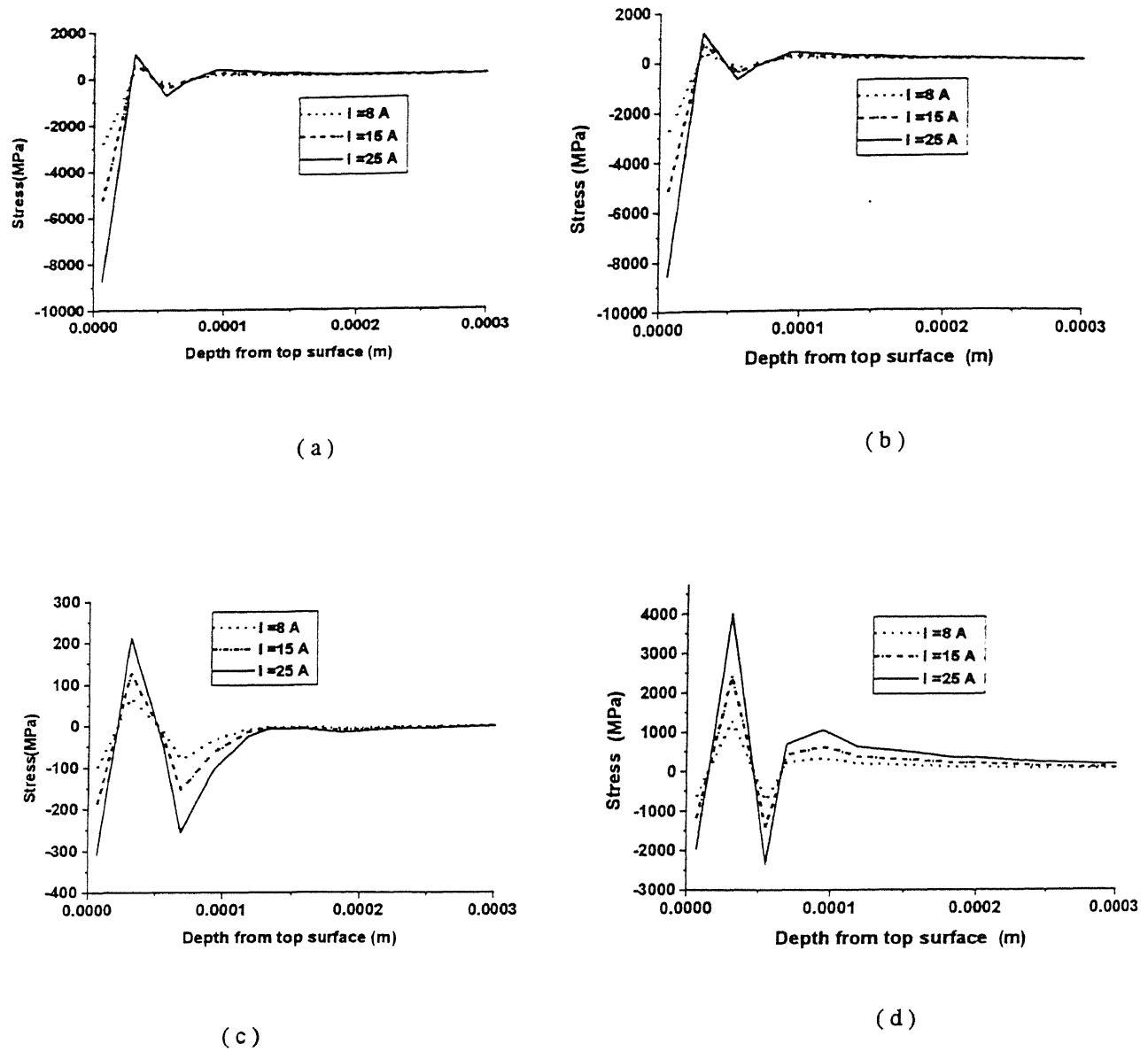


Fig. 3.15 Variation of components of thermal stresses with current along depth in HSS workpiece at $r = 7 \mu\text{m}$ for $U_b = 40$ V, $I = 8$ A, $R_w = 0.08$, $R = 125 \mu\text{m}$, $t_{on} = 100 \mu\text{s}$, duty cycle = 50% (a) σ_{rr} (b) $\sigma_{\theta\theta}$ (c) σ_{rz} (d) σ_{zz} . Results after 100 μs .

increase in current due to high heat flux value (Eq. 2.44) which leads to higher compressive thermal stresses. It is also observed from Fig. 3.14c that the range of change of variation (with change in sign) of shear component of thermal stresses at the center of the spark is approximately in the same ratio as increase in the current. The variation of

these stress components with current along depth at $r = 7 \mu\text{m}$ is shown in Fig. 3.15. Here, it is observed that the value of any stress component increases in the same proportion as increase in current. The nature of variation of stress components is not changing with change in current value.

3.4 Conclusions

Two thermal stress models-one for diamond cut-off grinding and other for EDM, which are constituent processes of EDDG, have been developed to predict thermal stress fields in HSS workpiece by developing two finite element based codes. The results obtained serve to illuminate the development of damaging thermal stresses during diamond cut-off grinding and EDM. The thermal stresses developed during diamond cut-off grinding have been found to be below the elastic limit of the HSS workpiece material under the machining conditions used. Hence, no thermal residual stresses are expected during diamond cut-off grinding. It is also observed that due to a single spark substantial compressive and normal tensile stresses are developed in a thin layer. It is also found that the thermal stresses exceed the yield strength of the workpiece, which is mostly confined to an extremely thin zone near the spark.

Chapter 4

Thermal Analysis of Electro-Discharge Diamond Surface Grinding

4.1 Introduction

If EDDG is applied in surface grinding mode where whole workpiece and a part of the grinding wheel are completely dipped in dielectric, the process can be called as Electro-discharge diamond surface grinding (EDDSG) (Fig. 4.1). Similar to thermal analysis of EDDG as discussed in chapter 2 of this thesis, thermal analysis of EDDSG consists of thermal analysis of diamond surface grinding and EDM. Knowledge of thermal analysis of EDDSG with almost zero current is indispensable for analysis of EDDG in surface grinding mode. Metal bonded diamond wheels are normally used during EDDSG, which are structurally very different than the conventional wheels [71-72, 89-90]. Hence, existing models pertaining to conventional wheels cannot be extended to diamond wheels. With this in view, a thermal model for diamond surface grinding is presented in this chapter. This model will be helpful in finding temperature distribution in the workpiece due to EDDSG.

For grinding of steels and ceramics, embedded thermocouples and infrared detection technique have been extensively used [91] to measure workpiece temperatures. Beck [92] pointed out that the error in thermocouple reading due to the presence of thermocouple itself could be as large as fifty percent of temperature rise in certain cases when the thermocouple is placed normal to the heated surface as is often the case in grinding. The same difficulty persists in infrared detection technique as far as the problem of hole drilling in the workpiece for the purpose of placing the sensor is concerned. The temperatures measured by Kato and Fujii [93] at various depths from the ground surface were found to be of satisfactory accuracy and reproducibility.

Most of the thermal models available in the literature are based on Jager's moving heat source model [35-39]. Numerical methods have also been applied to find temperature distribution in the workpiece [49,51].

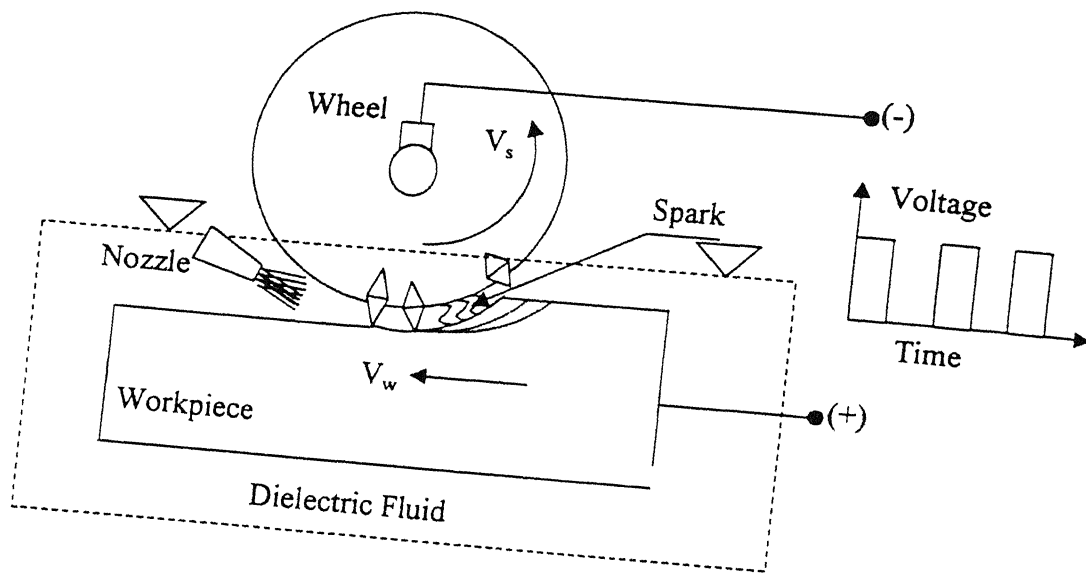


Fig. 4.1 Configuration of EDDSG

In this chapter, a FEM based thermal model is developed for simulation of temperature distribution in the workpiece during EDDSG with zero current. Particular attention has been paid to study the effects of heat flux magnitude and its distribution, table speed, diameter of grinding wheel, and depth of cut. Some of the realistic conditions such as non-uniform convection that accounts for partial cooling in the grinding zone and temperature dependent properties of workpiece are also considered.

4.2 Mathematical Modeling

In the thermal modeling of EDDSG with zero current, the physical phenomena, e.g. grain-workpiece interaction, rubbing and ploughing action of the grain are translated into mathematical form considering the process as 2-D boundary and initial value problem. The grinding zone is the region of contact length l_c and width b in the up-grinding mode (Fig. 4.1). The bottom surface of the workpiece rests on the surface of the worktable. Details of the theoretical thermal model used for the analysis of a workpiece temperature distribution, having length L and height H are shown in Fig. 4.2. Here, T_o is ambient temperature, h_c is convective heat transfer coefficient, and V_w is speed of the workpiece (table speed). S_1 , S_2 , S_3 and S_4 show the top, left, right and bottom surfaces of workpiece, respectively.

Five parameters are important for determining temperature distribution: contact length (l_c), magnitude of heat flux going to the workpiece (q_{wg}), distribution function (ϕ_g) for heat flux, energy partition (R_{wg}), and convective cooling (inside and outside the contact length) effect.

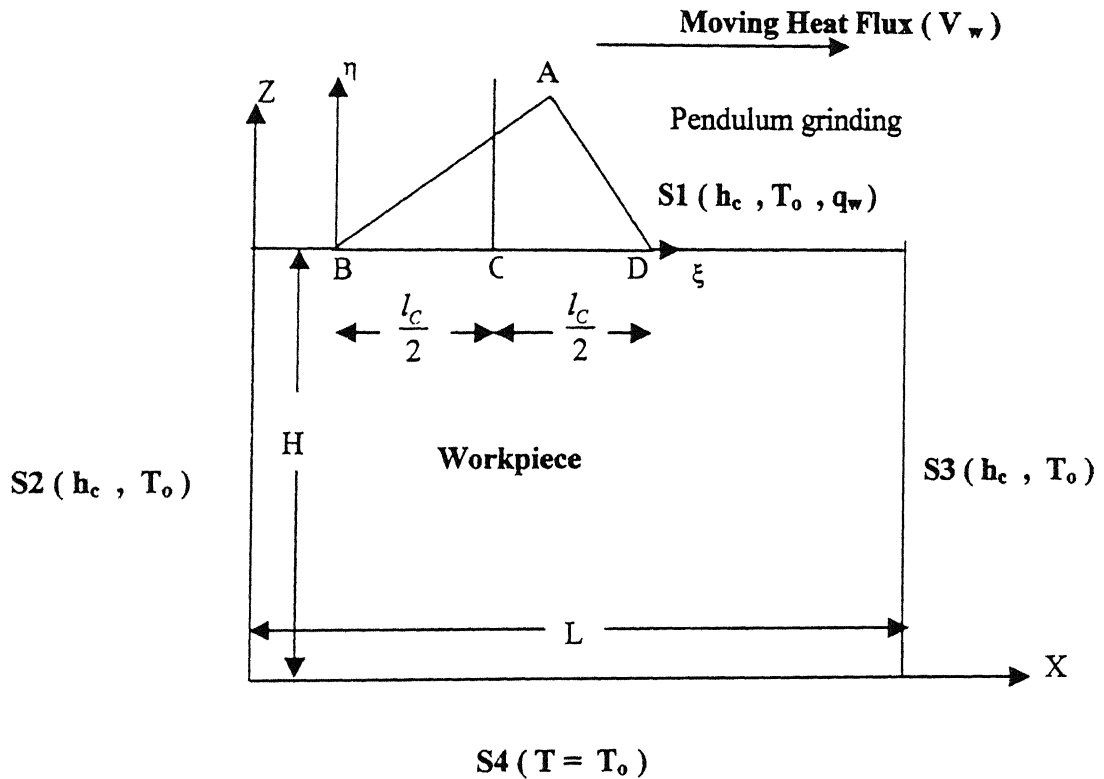


Fig. 4.2 Thermal model used for EDDSG with negligible current

Contact length:

The effective contact length between the wheel and workpiece is one of the principal factors that determine the temperature distribution, deformation distribution as well as surface integrity of the workpiece. The magnitude of the contact length determines how the heat pulse is distributed over the workpiece surface. Many efforts [94-98] have been made to study contact length using experimental, analytical and numerical approaches. Gu and Wager [95] have performed microscopic study of contact length considering local deflection of grains, grain shape, chip formation, local heat transfer, surface roughness of

workpiece and so forth. Salje and Mohlen [96] have reported a relationship between geometric and kinematic contact length. Numerical methods have been utilized [97] for more accurate calculation of effective contact length. The predicted value of the real contact length varies from one to ten times the geometrical contact length value [98]. Snoeys et al. [32] have shown that the real contact length is also dependent on depth of cut as well as speed ratio of wheel and workpiece.

The preceding studies show that at present there is no general formula that can predict the contact length applicable to all the grinding cases. Zhang et al. [94] have tabulated fourteen approximate formulae for contact length calculation. Most of them are based on experiments and their range of application is narrow. The relation between grinding conditions and the variation of contact length is complex. In the present model, geometrical contact length (l_c) is taken as equal to effective contact length for all computations, and it is given as follows

$$l_c = \sqrt{Dd} \quad (4.1)$$

The formula used for contact length by Eq. 4.1 ignores wheel-work deflection which will tend to increase wheel diameter but decrease depth of cut, sharpness of the wheel, coolant chemistry and its application methods, wheel and workpiece speeds as well as their properties.

Heat flux profile and magnitude

It is found that the spatial distribution (profile) of the heat source has a significant effect on temperature distribution in the workpiece. Usually, rectangular (uniform) heat flux distribution (Fig. 4.3) is assumed [35-38,51] for the thermal analysis of grinding but it is not supported by the temperature measurement. It is more appropriate to use a triangular heat flux distribution (Fig. 4.2) because the instantaneous material removal rate increases proportionally from the trailing to the leading edge of the grinding zone (Fig. 4.1). Rowe et al. [99] compared the measured temperature distribution in the contact zone with theoretical one for three different profiles: *rectangular heat flux distribution*, *triangular heat flux distribution*, and *square law heat flux distribution* (Fig. 4.3). They

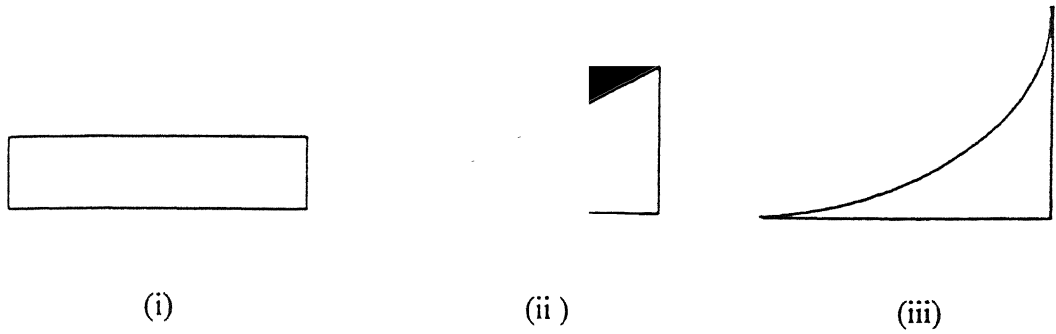


Fig. 4.3 Different heat flux profiles used for thermal model of surface grinding (i) Rectangular heat flux, (ii) Right angle triangular heat flux, (iii) Square law heat flux distribution

found that the best matching was with the square law heat flux distribution. Zhang and Mahdi [48] have shown that heat flux profile is neither rectangular nor parabolic nor square law. In fact, it can quite reasonably be approximated by a general triangular distribution with the apex located at a point between the inlet and the outlet of the contact bite (Fig. 4.2). Jen and Lavine [47] claimed that triangular heat flux results agree well with experimental results. In the present work, a general triangular heat flux profile (Fig. 4.2) is used for diamond surface grinding.

The magnitude of heat flux going to the workpiece during surface grinding is calculated by the following equation [72]

$$\left. \begin{aligned} q_{wg} &= \frac{2 R_{wg} U_0 V_w d}{l_c} \phi_g(\xi) \\ &= \frac{2 R_{wg} U_0 V_w \sqrt{d}}{\sqrt{D}} \phi_g(\xi) \end{aligned} \right\} \quad (4.2)$$

where, distribution function $\phi_g(\xi)$ for heat flux in surface grinding is given by:

$$\phi_g(\xi) = \left\{ \begin{array}{ll} 0 & \text{if } \xi < 0 \text{ or } \xi > l_c \\ \frac{\xi}{\left(\frac{l_c}{2} + \xi_a\right)} & \text{if } 0 \leq \xi \leq \left(\frac{l_c}{2} + \xi_a\right) \\ \frac{(l_c - \xi)}{\left(\frac{l_c}{2} - \xi_a\right)} & \text{if } \left(\frac{l_c}{2} + \xi_a\right) \leq \xi \leq l_c \end{array} \right\} \quad (4.3)$$

Here, R_{wg} is energy partition due to grinding, V_w is table speed, ξ_a is the distance of heat flux peak (A) from its centre (C) (Fig. 4.2), and U_o is specific grinding energy.

Energy partitioning:

Selection of energy partition (R_{wg}), which is defined as the ratio of energy carried by the workpiece to the total grinding energy, is of special importance in determining the thermal load on the workpiece. The value of this fraction is a controlling parameter in determination of the workpiece temperature rise and helps in understanding various thermal phenomena occurring within the grinding zone.

Several researchers [99-111] have done extensive work to find the value of R_{wg} experimentally as well as theoretically during surface grinding. Ramanath and Shaw [100] studied the heat partition between an abrasive grain and the workpiece to obtain R_{wg} from the ratio of the geometric mean thermal properties ($GMTP = \sqrt{k\rho c}$) of the workpiece and the abrasive. The value of R_{wg} so obtained is 0.7 for aluminium oxide wheel and 0.51 for CBN wheel during pendulum and creep feed grinding of steel. Shaw [101] explained that the outstanding performance of CBN is not due to its high value of thermal conductivity alone but is really due to its relatively high value of GMTP, which in turn gives a low value of R_{wg} .

Rowe et al. [102] determined energy partition by considering the grinding wheel (aluminium oxide) and workpiece (steel) as two sliders and assumed equal average temperature in the grinding contact zone. They have also shown that R_{wg} varies with table speed if table speed is more than 100 mm/s but the variation of R_{wg} with depth of cut is negligibly small for grinding of steel with CBN wheel. A substantially lower value of R_{wg}

was found for grinding with CBN and diamond wheels as compared to alumina and silicon carbide grinding wheel with steel workpiece [103-105] because more grinding energy is carried away by the superabrasive grinding wheel due to its superior thermal properties.

Kohli et al. [106] used the 'trial and error' method to obtain the value of R_{wg} so that the values predicted by their model match with the experimental data on subsurface temperature during pendulum surface grinding of steel with aluminium oxide wheel. The value of R_{wg} so obtained has a very narrow variation (0.6-0.7). Guo and Malkin [107] obtained the distribution of R_{wg} (earlier it was assumed constant) along the grinding zone under pendulum and creep-feed grinding by assuming the temperature on the workpiece surface equal to that on the composite surface at every point of the grinding zone.

Energy partitions of 4 to 8.5 % for hardened bearing steel and 3 to 6 % for nodular cast iron are reported [108,109] under fine surface grinding with CBN wheel by using a temperature matching and inverse heat transfer method. These results indicate that vitrified bond CBN wheel may benefit from both high thermal conductivity of abrasive grain and cooling by grinding fluid due to *porous structure* of vitrified wheel. Cooling is improved because of the porous structure of the vitrified wheel enhances fluid flow.

Kato and Fujii [110] estimated energy partition R_{wg} to the workpiece in surface grinding by measuring temperatures at various depths from the ground surface of the work-piece using PVD (physical vapor deposition) film method and top surface temperature by extrapolation. They reported that the value of the R_{wg} varies significantly from 0.3 to 0.8, depending on the combination of the workpiece material and the wheel material. For grinding of carbon steel, this was approximately 0.25 with the diamond wheel, 0.75 with the aluminum oxide wheel, and 0.45 with the silicon carbide and CBN wheels but independent of grinding parameters such as table speed (V_w) and depth of cut. For grinding with aluminum oxide wheels, the value of R_{wg} is about 0.5-0.6 for stainless steel and brass, and 0.7-0.8 for cast iron and carbon steel. Ju et al. [111] have found that R_{wg} varies within contact length but this variation is negligibly small for fine grinding of steel with CBN wheel. Most of the suggested values are valid either for resin bonded or

vitrified bonded wheels. But information concerning the value of R_{wg} for grinding HSS with metal bonded diamond wheel is nonexistent in the literature.

In the present work, the value of R_{wg} is chosen as 0.25 for computational purpose in diamond surface grinding which is close to the experimentally measured value in the reference [110].

Specific energy:

A fundamental parameter derived from the power and grinding conditions is specific grinding energy, which is defined as the energy required to remove unit volume of material. It is obtained from the ratio of grinding power to material removal rate. The total specific grinding energy is considered to consist of chip formation, plowing, and sliding components. It is reported [71,72] that specific grinding energy is nearly identical for a diverse range of steels (low carbon steel to high speed tool steel) despite vast differences in workpiece hardness.

Most of the temperature predictions available in literature are based on measured grinding forces from which specific grinding energy is determined for a particular grinding wheel, workpiece, and grinding conditions. It has been found that the specific grinding energy varies with depth of cut, table speed, work material, wheel material, and wheel conditions. It is very difficult to account variable specific energy purely from theory until unless nature of variation of U_0 with each of these parameters is known in advance. It is also reported in literature [71,72,110] that the specific grinding energy lies between 60–85 GPa during grinding of HSS with CBN grinding wheel.

In the present work, the value of U_0 is chosen 55 GPa for fine diamond surface grinding which is close to the experimentally measured value in the reference [110] for surface grinding of steel with diamond wheel.

Material thermal properties:

In general, the material thermal properties such as specific heat capacity and thermal conductivity are temperature dependent. Most of the thermal models for grinding, available in literature, have assumed thermal properties independent of temperature. It is also reported that the values of thermal properties do not change significantly with temperature and, hence, the average values can also be used. Using data of temperature dependent thermal conductivity and specific heat of HSS workpiece

[112]. the best-fit curves are obtained to find the nature of variation in polynomial equation form, which are used in the numerical calculations [Fig. 4.4]. These polynomial equations are given below:

$$C = 286.97 + 0.578T - 0.00115T^2 + 1.522T^3 - 5.595 \times 10^{-10} T^4$$

$$k = -39.296 + 0.596T - 0.00228T^2 + 4.616T^3 - 5.06T^4 + 2.824 \times 10^{-12} T^5 - 6.244 \times 10^{-16} T^6$$

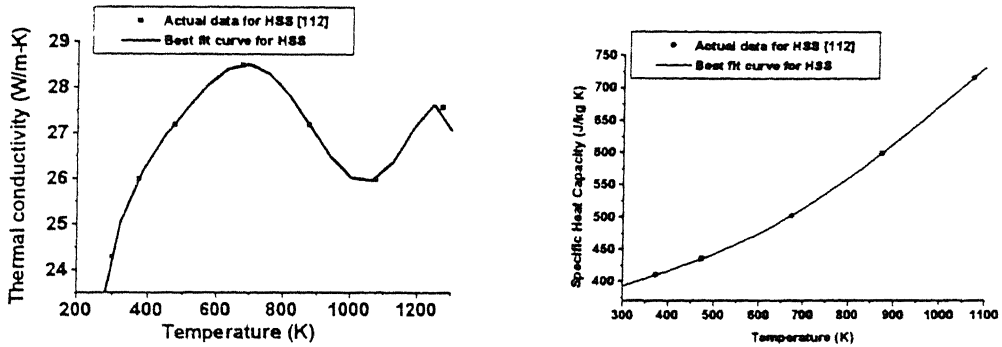


Fig. 4.4 Variation of (a) thermal conductivity, (b) specific heat with temperature

Dielectrics:

The effect of surface cooling by grinding fluid was analyzed by Des Ruisseaux and Zerkele [38]. Cooling is not very effective for reducing local high temperature rise if extreme care is not taken for its application. It is critically important that the coolant is forced into the contact zone. Porous grinding wheels, such as electro-plated or vitrified bonded superabrasive wheels are very effective in reducing temperature in the contact zone.

In the present work, dielectric acts as a coolant also. Generally, h_c is a function of temperature, wheel speed and method of coolant application. No data is available in literature showing the nature of variation of h_c with each of these parameters for grinding of HSS workpiece with diamond wheel. In this work, the value of convective heat transfer coefficient inside the contact zone is considered as only 60 % ($0.6 h_c$) of the outside value which is found after different computational experiments [Fig 4.8].

4.3 Finite Element Formulation

In the proposed model, the energy balance in the workpiece governs the heat transfer equations. The equations used for modeling and simulation include governing equations, boundary conditions, and initial conditions.

Heat diffusion equation with temperature independent material properties is used to find temperature field due to grinding operation

$$\rho C_p \frac{\partial T}{\partial t} = \frac{\partial}{\partial x} \left(k \frac{\partial T}{\partial x} \right) + \frac{\partial}{\partial z} \left(k \frac{\partial T}{\partial z} \right) \quad (4.4)$$

Here, T is temperature, ρ is density, k is thermal conductivity, and C_p is specific heat of workpiece material.

Energy transferred to the workpiece as heat input serves as **thermal boundary condition** on the top surface $S1$ (Fig. 4.2). The bottom of the workpiece is assumed to be sufficiently remote from the top surface so as to remain at its initial temperature throughout the grinding operation. Heat loss to the coolant on the surfaces $S1$, $S2$, and $S3$ is modeled using convective boundary condition. Thus, the boundary conditions are:

$$\left. \begin{aligned} q &= -k \nabla T \cdot \hat{n} = -q_w + h_c T \quad \text{on } S1, S2, S3 \\ \text{where,} \\ q_w &= q_{wg} + h_c T_0 \quad \text{on } S1 \\ q_w &= h_c T_0 \quad \text{on } S2, S3 \\ T &= T_0 \quad \text{on } S4 \end{aligned} \right\} \quad \text{when } t > 0, \quad (4.5)$$

The initial temperature can be taken as temperature of the dielectric in which the workpiece is completely dipped). Thus,

$$T = T_i = T_0 \quad \text{at } t=0 \quad (4.6)$$

Galerkin Formulation

The Galerkin weighted residual method [73] is used to convert the governing differential equation (Eq. 4.4) into algebraic equations by using appropriate weighting functions. When the residue is made orthogonal to the weight function, the following integral equation is obtained.

$$\int_{\Omega} \left\{ \rho C_s \frac{\partial T}{\partial t} - \left[\frac{\partial}{\partial x} \left(k \frac{\partial T}{\partial x} \right) + \frac{\partial}{\partial z} \left(k \frac{\partial T}{\partial z} \right) \right] \right\} W dx dz = 0 \quad (4.7)$$

In the vector notation, this can be written as

$$\int_{\Omega} \rho C_s \frac{\partial T}{\partial t} W dx dz - \int_{\Omega} [\nabla \cdot (k \nabla T)] W dx dz = 0 \quad (4.8)$$

The second term can be expanded using a vector identity. Thus,

$$\int_{\Omega} \rho C_s \frac{\partial T}{\partial t} W dx dz - \int_{\Omega} [\nabla \cdot (W k \nabla T)] dx dz + \int_{\Omega} \nabla W \cdot k \nabla T dx dz = 0 \quad (4.9)$$

The second term of the expression (4.9) is modified using the divergence theorem, which gives rise to certain boundary terms. Thus, the expression becomes:

$$I_1 + I_2 + I_3 = 0 \quad (4.10)$$

where,

$$I_1 = \int_{\Omega} \rho C_s \frac{\partial T}{\partial t} W dx dz \quad (4.11)$$

$$I_2 = \int_{\Omega} \nabla W \cdot k \nabla T dx dz = 0 \quad (4.12)$$

$$I_3 = - \int_{\Gamma} W q_{ws} d\Gamma + \int_{\Gamma} h_c W T d\Gamma = 0 \quad (4.13)$$

Finite element approximation

To obtain the finite element equation from expression (4.10), the domain is discretized into *nem* number of elements (Fig. 4.5). Further, over a typical element, the temperature is approximated using the unknown nodal values T_i^e and the known interpolation (or shape) functions N_i^e . In the present work, 8-noded isoparametric quadrilateral elements are used. Thus,

$$T(x, z, t) = \{N^e\}^T \{T^e\} \quad (4.14)$$

where,

$$\{N^e\}^T = \{N_1^e \quad N_2^e \quad N_3^e \quad \dots \dots \dots N_8^e\} \quad (4.15)$$

and

$$\{T^e\}^T = \{T_1^e \quad T_2^e \quad T_3^e \quad \dots \dots \dots T_8^e\} \quad (4.16)$$

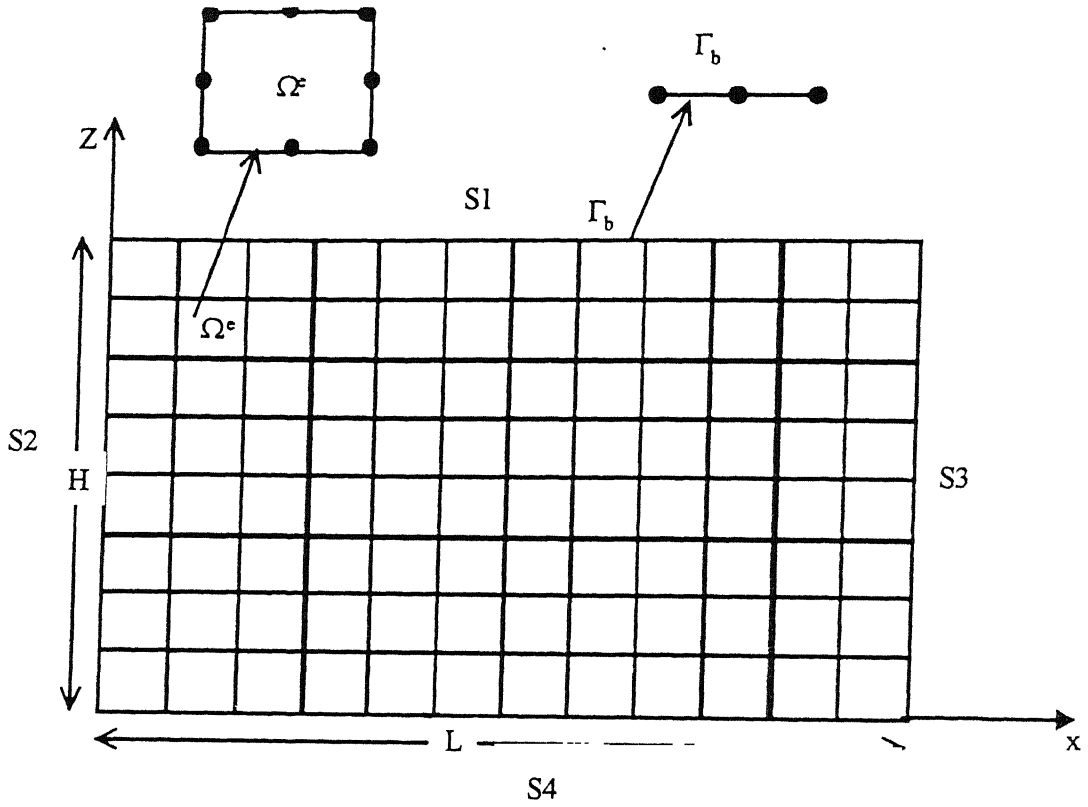


Fig. 4.5 The finite element mesh of the workpiece used in EDDSG

In Galerkin's method, the weighting functions are also expressed using the same shape functions. Therefore,

$$W(x, z) = \{N^e\}^T \{W^e\} \quad (4.17)$$

where, the vector $\{W^e\}$ contains the nodal values of W which are known but arbitrary.

Now,

$$\{\nabla T\} = [B^e] \{T^e\} \quad (4.18)$$

$$\{\nabla W\} = [B^e] \{W^e\} \quad (4.19)$$

where,

$$[B^e] = \begin{bmatrix} \frac{\partial N_1^e}{\partial x} & \frac{\partial N_2^e}{\partial x} & \frac{\partial N_3^e}{\partial x} & \frac{\partial N_4^e}{\partial x} & \frac{\partial N_5^e}{\partial x} & \frac{\partial N_6^e}{\partial x} & \frac{\partial N_7^e}{\partial x} & \frac{\partial N_8^e}{\partial x} \\ \frac{\partial N_1^e}{\partial z} & \frac{\partial N_2^e}{\partial z} & \frac{\partial N_3^e}{\partial z} & \frac{\partial N_4^e}{\partial z} & \frac{\partial N_5^e}{\partial z} & \frac{\partial N_6^e}{\partial z} & \frac{\partial N_7^e}{\partial z} & \frac{\partial N_8^e}{\partial z} \end{bmatrix} \quad (4.20)$$

Further,

$$\frac{\partial T}{\partial t} = \{N^e\}^T \left\{ \dot{T}^e \right\} \quad (4.21)$$

where, $\left\{ \dot{T}^e \right\}$ contains the time derivative of the nodal value of T.

In the present work, the geometry is also approximated by the same shape functions. Thus,

$$x = \{N^e\} \{x^e\}; \quad z = \{N^e\} \{z^e\} \quad (4.22)$$

where, the vectors $\{x^e\}$ and $\{z^e\}$ contain the nodal values of x and z coordinates, respectively.

To express the boundary terms in terms of the nodal quantities, approximation over the boundary is needed. Note that, as the domain is divided into *nem* number of elements, the boundary automatically gets divided into *nbe* number of elements. Now, the approximation for W, T and q_w over a typical boundary element can be written as:

$$W = \{N^b\}^T \{W^b\} = \begin{bmatrix} N_1^b & N_2^b & N_3^b \end{bmatrix} \begin{Bmatrix} W_1^b \\ W_2^b \\ W_3^b \end{Bmatrix} \quad (4.23)$$

$$T = \{N^b\}^T \{T^b\} = \{N_1^b \quad N_2^b \quad N_3^b\} \begin{Bmatrix} T_1^b \\ T_2^b \\ T_3^b \end{Bmatrix} \quad (4.24)$$

$$q_w = \{N^b\}^T \{q_w^b\} = \{N_1^b \quad N_2^b \quad N_3^b\} \begin{Bmatrix} q_{w1}^b \\ q_{w2}^b \\ q_{w3}^b \end{Bmatrix} \quad (4.25)$$

Note that the vector $\{N^b\}$ contains 1-D quadratic shape functions, which have a boundary approximation consistent with the 2-D approximation over the domain.

Finite element equations

Substitution of the approximation for temperature and the expression for weight functions (equations 4.14-4.25) in integral (4.10) leads to

$$\sum_{e=1}^{nem} \{W^e\}^T [C^e] \{\dot{T}^e\} + \sum_{e=1}^{nem} \{W^e\}^T [K^e] \{T^e\} - \sum_{b=1}^{nb} \{W^b\}^T \{f^b\} + \sum_{b=1}^{nb} \{W^b\}^T [K^b] \{T^b\} = 0 \quad (4.26)$$

where, the elemental capacitance matrix $[C^e]$, the elemental conductivity matrix $[K^e]$, the boundary conductivity matrix $[K^b]$, and boundary heat flux vector $\{f^b\}$ are given by

$$\left. \begin{aligned} [C^e] &= \int_{\Omega^e} \rho c \{N^e\} \{N^e\}^T dx dz \\ [K^e] &= \int_{\Omega^e} k [B^e]^T [B^e] dx dz \\ [K^b] &= \int_{\Gamma_b} h_c \{N^b\} \{N^b\}^T d\Gamma \\ \{f^b\} &= \int_{\Gamma_b} \{N^b\} \{N^b\}^T \{q_w^b\} d\Gamma \end{aligned} \right\} \quad (4.27)$$

Here, Ω^e is the domain of typical area element and Γ_b is the domain of typical boundary element (Fig. 4.5). The integrals in the expression (4.27) are computed using Gaussian quadrature with 3 points in each direction. The expression (4.26) when expressed in terms of global quantities takes the form

$$\{W\}^T [C] \left\{ \dot{T} \right\} + \{W\}^T [K] \{T\} = \{W\}^T \{F\} \quad (4.28)$$

where, $[C]$ is the global capacitance matrix, $[K]$ is the global conductivity matrix, $\{F\}$ is the global heat flux vector, $\{T\}$ is global temperature vector, and $\left\{ \dot{T} \right\}$ is the time derivative of $\{T\}$.

Since the nodal value of weight functions are arbitrary

$$[C] \left\{ \dot{T} \right\} + [K] \{T\} = \{F\} \quad (4.29)$$

Equation (4.29) represents a set of ordinary differential equations in the variable $\{T\}$. These equations are solved after finite difference method (FDM as discussed in section (2.2.2). In diamond surface grinding, Δt is selected as time required to move forward exactly by one element length of the grinding domain in the direction of flux motion.

4.4 Results and Discussion

In order to assess accuracy and efficiency of the present finite element formulation, an example involving two different shapes of moving heat sources over the top surface of the workpiece are simulated and results are compared with the known theoretical results of Li and Chen [80] for conventional surface grinding. Table 4.1 gives the data related to thermal properties of grinding wheel and workpiece, and process parameters used in theoretical calculations of Li and Chen [80]. Due to limitation of computing resources, the domain size is chosen as one-fourth of the domain in reference [80]. Convergence study revealed that the mesh of 480 elements and 1577 nodes is adequate for this problem. Since no information is available about the actual shape of the heat flux, the results reported by the authors in this paper are obtained assuming two commonly used shapes: rectangular (uniform) and general triangular. The heat flux is distributed over 8 elements and moved forward exactly by one element after every step.

A comparison of variation of surface temperature along the top surface with the results of reference [80] is shown in Fig. 4.6. The trend of the results matches well, but

there is discrepancy between the values. This could be due to the difference in domain size and shape of the heat flux used in these two problems.

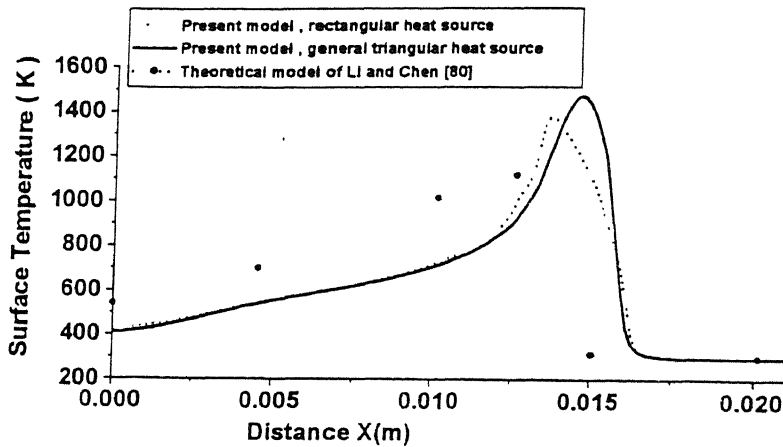


Fig. 4.6 Variation of top surface temperature during surface grinding computed with heat source of different shapes and the results of Li and Chen [80]

Table 4.1: Data related to thermal properties of grinding wheel and workpiece, and process parameters used by Li and Chen [80]

Workpiece	SAE1038 Steel
	(21 mm * 2.8 mm)
Wheel	Al ₂ O ₃
ρ_w (kg/m ³)	7880
c_w (J/kg K)	502
k (W/mK)	50.2
h_c (W/m ² K)	3000.0 (Water)
V_w (mm/s)	70.0
V_s (m/s)	30.0
D (mm)	126
d (mm)	0.0625
U_o (J/m ³)	$68950 * 10^6$
R_{wg}	0.70
l_c (mm)	2.8
time (t) second	0.2

Temperature distribution in the workpiece

In this section, various results showing the effects of various process parameters on top surface temperature distribution in EDDSG with zero current are given. First, computational experiments are conducted to include the effect of temperature dependent properties of the workpiece on top surface temperature distribution in the workpiece but hardly any change in top surface temperature is observed (Fig.4.7). This shows that temperature generated for the set of conditions used is not sufficient to change the material properties significantly. Hence, for the prescribed machining conditions it is more reasonable to predict temperature based on average value of thermal properties. Process parameters used for the present calculation are given in Table 4.2.

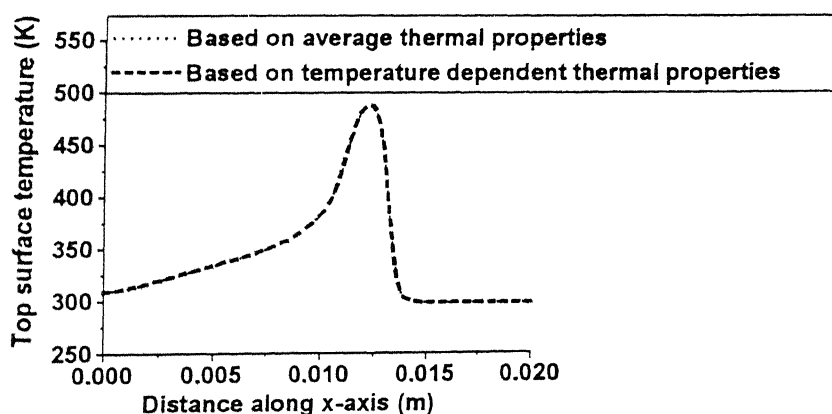


Fig. 4.7 Effect of material thermal properties on top surface temperature at $V_w = 50$ mm/sec and $d=0.04$ mm after 0.224 s

Table 4.2: Process parameters used in the present model

Workpiece	HSS (21 mm * 2.8 mm)
Grinding Wheel	Metal bonded diamond wheel
h_c (W/m ² K)	10000.0 (Kerosene)
U_o (J/m ³)	55000×10^6
R_{wg}	0.25

Figure 4.8 shows temperature distribution at the workpiece top surface for different values of convective heat transfer coefficient inside the contact length. For simplicity, we first assume that inside convective heat transfer coefficient $h_i = f h_c$, where $f \leq 1$ is a positive constant number (effective cooling factor). It is found that the critical value for HSS is 0.6. Above this value, there is no change in top surface temperature. It may differ from material to material. The effect is found to be insignificant because maximum temperature difference of 20-25 K is noted at the location where temperature peaks lie.

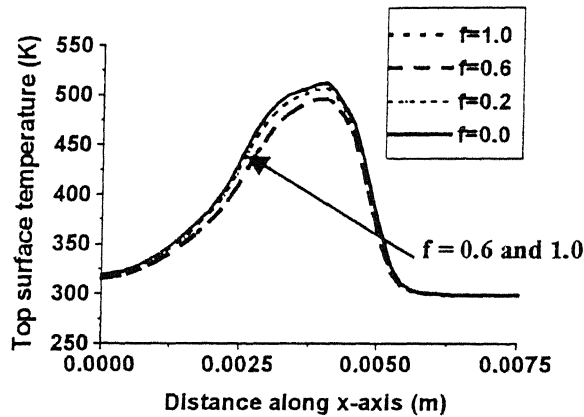


Fig. 4.8 Effect of cooling on top surface temperature at $V_w = 50$ mm/sec and $d=0.04$ mm after 0.224 s

Figure 4.9a shows the top surface temperature distribution along the x-axis for different times. Here, Δt is selected as time required to move forward exactly by one element length of the grinding domain in the direction of flux motion. In Fig 4.9a the time interval for one element length movement is 0.007 s. After doing computational experiments it has been found that the peak temperature becomes constant after 0.056 s (after 8 element length movement of the heat source). It is also noted that the temperature gradient within the contact zone also becomes almost constant. The variation of temperature with time at a point ($x=10.5$ mm) on top surface of the workpiece is shown in Fig 4.9b. This shows the transient nature of variation of temperature over the workpiece top surface.

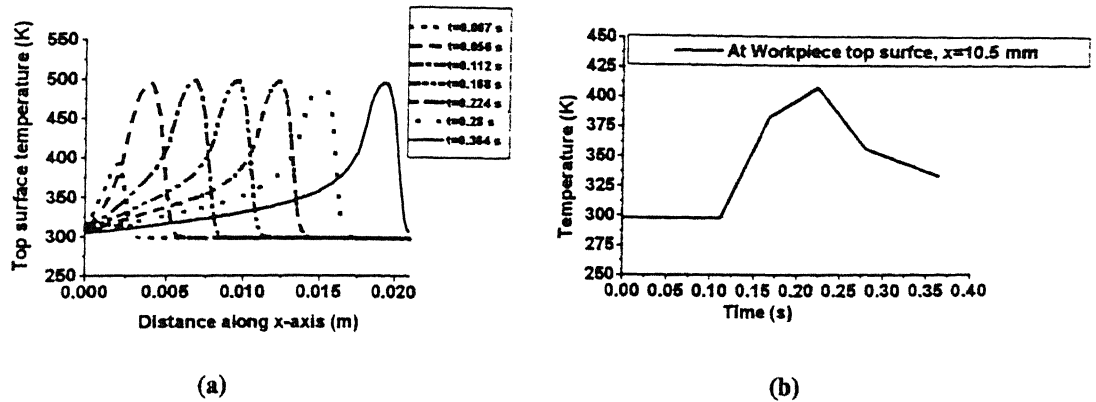


Fig. 4.9 Variation of temperature with time (a) at top surface (b) at a point on top surface ($x = 10.5$ mm) after different time for $V_w = 50$ mm/sec and $d=0.04$ mm

Figure 4.10 shows temperature distribution at the workpiece top surface for different depths of cut after grinding time $t = 0.224$ s when the table speed is constant. It is observed that the temperature at top surface is higher for larger depth of cut. From Eq. 4.2 it can be seen that an increase in 'd' leads to higher heat flux at the contact zone which is the cause of increase in temperature at larger depth of cut. Here, it is observed that the temperature gradients which are the main cause of thermally induced residual stresses are increasing from 10.0 K/m to 85.0 K/m when d is increased from 0.01 mm to 0.09 mm, respectively (between $x=0.005$ m to $x=0.01$ m).

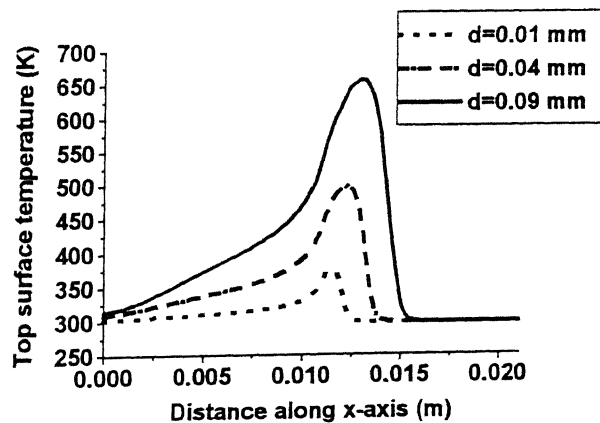


Fig. 4.10 Top surface temperature variation along x-axis for different depth of cut (d) at $V_w = 50$ mm/sec after $t = 0.224$ s

Figure 4.11 shows the effect of heat flux speed (table speed) for constant contact length. Here rise in surface temperature is noted when the length of heat source travel ($V_w t$) with different table speed is same (11.2 mm). The results show that the peak temperature of the top surface under the heat source increases with increase in table speed. This can be explained as follows. Equation (4.2) shows that the heat flux is proportional to the heat source speed. Hence by increasing table speed the heat flux will increase and hence the peak temperature will be more. The curves show that the temperature increases from 425 K to 600 K when the table speed is increased from 25 mm/s to 100 mm/s.

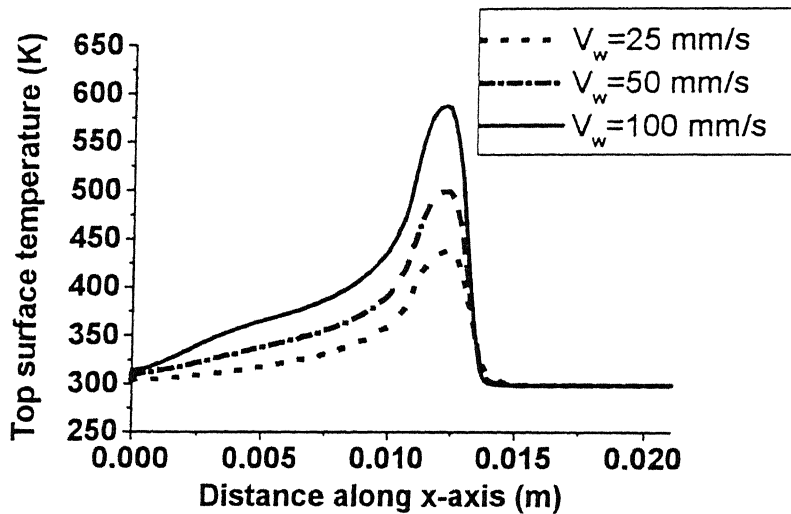


Fig. 4.11 Top surface temperature variation along x-axis for different table speed at $d = 0.04$ mm after table travel of 11.2 mm.

Figure 4.12 shows the variation of top surface temperature for different diameter wheel (D) at a constant depth of cut. It is observed that the peak temperature is lower for higher diameter wheel. This trend can be explained as follows. With increase in grinding wheel diameter, the contact length increases which promotes more heat convection and decreases the amount of heat flux q_{wg} (Eq. 4.2).

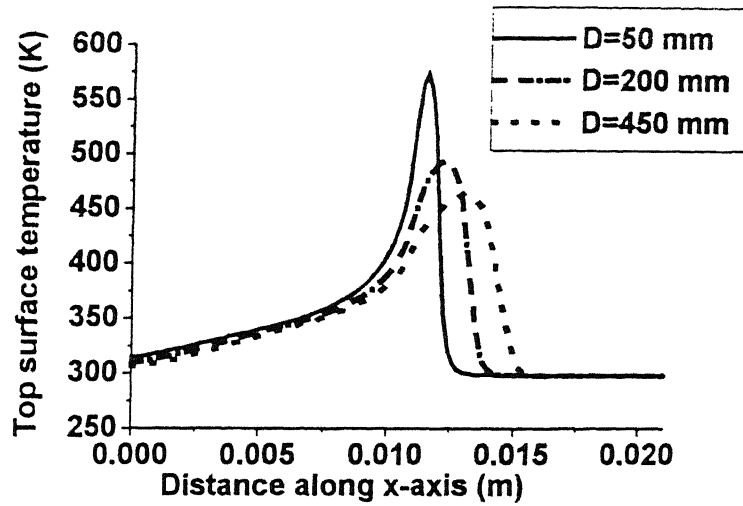


Fig. 4.12 Top surface temperature variation along x-axis for different diameter wheel at $V_w = 50$ mm/sec and $d=0.04$ mm after $t = 0.224$ s.

4.5 Conclusions

A FEM based numerical model has been developed to provide a theoretical determination of temperature distributions in HSS workpiece during EDDSG with zero current. This would help in predicting preliminary results, regarding temperature distribution in the workpiece, before going for actual costly and time-consuming experimental procedure for the measurement of workpiece temperature during actual EDDSG. It is found that the consideration of temperature dependent properties of the workpiece and non-uniform cooling consideration is not significant. Top surface temperature increases with increase in depth of cut and table speed. Bigger wheel is found to reduce the temperature rise at the workpiece top surface.

Chapter 5

Conclusions and Future Work

5.1 Conclusions

The present thesis work comprises finite element analysis of EDDG process for finding temperature distribution in the workpiece only. Temperature distribution in the workpiece due to EDDG has been obtained by thermal analysis of diamond cut-off grinding and EDM. Thermal stresses have also been obtained for each constituent process of EDDG such as diamond cut-off grinding and EDM. EDDSG has been analyzed for temperature distribution in the workpiece when current is switched off. Numerical experiments have been conducted to study the influence of process parameters on the process performance. On the basis of these computational investigations, following conclusions can be drawn:

❖ Thermal Analysis of EDDG

- 3-D temperature distribution in the workpiece during EDDG can be obtained by superposing results of the 2-D thermal analyses of diamond cut-off grinding and axisymmetric thermal analysis of EDM.
- Temperature fields of 2-D thermal analysis of cut-off grinding and axisymmetric thermal analysis of EDM compare favorably well with the experimental/theoretical results available in the literature.
- The thermal model for diamond cut-off grinding predicts the temperature distribution in the workpiece fairly accurately including the effects of feed, convective heat transfer coefficients of dielectrics and thermal properties of diamond grinding wheel if accurate values of specific energy and energy partition for the process conditions are available.
- The thermal analysis of EDM predicts the temperature distribution in the workpiece fairly accurately including the effects of on-/off-time, phase change, duty cycle if accurate values of the energy partition and spark radius for the process conditions are known.

- A sharp increase in temperature is observed around spark locations after superposition of grinding and EDM temperature distributions at the top surface of the workpiece.
- Temperature gradients due to EDDG are found to be very high in a thin surface layer adjacent to spark locations. This shows that temperature-softening effects are limited to a thin layer around the spark flux.
- Effects of feed and current on temperature distribution during EDDG are significant but no change is observed by varying duty cycle.

❖ Thermal Stress Analysis of EDDG

- Two thermal stress models developed, one for cut-off grinding and other for EDM, are capable to determine the thermal stresses due to each constituent process of EDDG.
- The thermal stresses developed during cut-off grinding have been found to be below elastic limit of the HSS workpiece material for the conditions used. Hence, no thermal residual stresses are found during diamond cut-off grinding under the machining conditions used during the reported work.
- The thermal effect of spark is limited to a localized area around the spark at the top surface of the workpiece. Hence, thermal stresses have been found in the plastic range within a small thickness around the crater created by the spark.

❖ Thermal Analysis of Electro-Discharge Diamond Surface Grinding

- A FEM based numerical model developed for simulation of temperature distribution in the workpiece during EDDSG with negligible current (case of diamond surface grinding in which workpiece is dipped in dielectric) would reduce the need for costly and time-consuming experimental procedure for the measurement of workpiece temperature during grinding.
- The results presented would be useful for prediction of temperature distribution in the workpiece in combined process of diamond surface grinding and EDM called as EDDSG.
- The effect of cooling on temperature rise in the workpiece is found to be less significant during diamond surface grinding.

5.2 Scope for Future Work

In the present study, an attempt has been made to determine 3-D temperature distribution in the workpiece during a new hybrid machining process called Electro discharge diamond grinding (EDDG). In this thesis, thermal aspects relating to temperature distribution and thermal stresses have been studied for deep understanding about EDDG process. Some of the issues, which can be examined in future, are summarized as follows:

1. A comprehensive 3-D thermal model is needed to find temperature distribution in the workpiece during EDDG in cut-off grinding mode considering random generation of sparks at the top surface.
2. A fast response temperature-measuring instrument and a suitable dynamometer need to be employed to measure temperature and cutting forces respectively. The temperature dependent specific energy can be estimated using measured cutting forces and then actual strength of heat flux supplied to the workpiece can be determined. Again, energy partition to the workpiece during EDDG can be obtained by temperature-matching methodology using measured temperatures at various depths.
3. An integrated theoretical approach could be tried for thermal analysis of EDDG process where the effect of combined phenomenon of abrasion and EDM on temperature distribution in the wheel and workpiece can be treated together. First, the energy partitions into wheel, workpiece, and dielectric are to be found and then using these data, temperature distribution in the wheel and workpiece can be determined.
4. The feasibility of EDDSG could be explored experimentally to generate flat workpiece surfaces.
5. In addition to temperatures, a rigorous theoretical analysis, as well as experimental measurement of residual stresses produced in the workpiece are completely lacking. Hence, a surface integrity model needs to be developed which can predict transient temperature field, residual stresses and thermal damage in the workpiece.
6. Because of the complexity of EDDG process, the optimization of process parameters as well as optimal control of the process will be of considerable interest.

References

1. Konig W., Cronjager L., Spur G., Tonshoff H.K., Vigneau M. and Zdeblick W.J., Machining of new materials, *CIRP Annals*, 39(2)(1990) 673-681.
2. Yang X. and Liu C.R., Machining of titanium and its alloys, *Machining Science and Technology*, 3(1)(1999) 107-139.
3. Konig W. and Dauw D.F., EDM-Future steps towards the machining of ceramics, *CIRP Annals*, 37(2)(1988) 623-631.
4. Klocke F., EDM of special materials, *Proc. 12th International Symposium for Electromachining (ISEM-12)*, Tagung, Anchan, 425-522(1998).
5. Muller F. and Monaghan J., Non-conventional machining of particle reinforced metal matrix composite, *Int. J. Mach. Tools Manufact.*, 40 (2000) 1351-1366.
6. Jain V.K., *Advanced machining processes*, Allied publisher, Bombay, 2001.
7. Pandey P.C., *Modern machining methods*, Tata McGraw Hill, New Delhi.
8. Koshy P., Jain V.K. and Lal G.K., Experimental investigations into electrical discharge machining with a rotating disk electrode, *Precision Engineering*, 15(1) (1993) 6-15.
9. Kozak J. and Kazimierz E.O., Selected problems of abrasive hybrid machining, *J. Materials Processing Technology*, 109(2001) 360-366.
10. McGeough J.A., Khayry A.B.M. and Monro W., Theoretical and experimental investigation of relative effects of spark erosion and electro-chemical dissolution in electro-chemical arc machining, *CIRP Annals*, 32(1)(1983) 113-118.
11. Jain V.K., Rao P.S., Choudhury S.K., and Rajurkar K.P., Experimental investigations into travelling wire electrochemical spark machining (TW-ECSM) of composites, *Trans. ASME, Journal of Engineering for industry*, 113(1) (1991) 75-84.
12. Gautam N. and Jain V.K., Experimental investigation into ECSM process using various tool kinematics, *Int. J. Mach. Tools Manufact.*, 38(1) (1998) 115-273.
13. Jain V.K. and Chak S.K., Electrochemical spark trepanning of Alumina and quartz, *Machining Science and Technology*, 4(2) (2000) 277-290.
14. Koshimizu S. and Inasaki I., Hybrid machining of hard and brittle materials, *J. Mech. Work. Technology*, 17(1988) 333-341.

15. Zhixin J., Zhang J. and Xing A., Study of a new kind of combined machining technology of ultrasonic machining and electrical discharge machining," *Int. J. Mach. Tools Manufact.*, 37(2) (1997) 193-199.
16. Kitgawa T. and Maekawa K., Plasma hot machining for new engineering materials," *Wear*, 139(1990) 251.
17. Chrysosolouris G., Anifantis N. and Karagiannis S., Laser assisted machining: An overview, *Trans. ASME, Journal of Manufacturing Science and Engineering*, 119(1997) 766-769.
18. van Luttervelt C.A., Childs T.H.C., Jawahir I.S. and Klocke F., Present situation and future trends in modeling of machining operations, *CIRP Annals*, 42(2)(1998) 587-626.
19. Tonshoff H.K., Peters J., Inasaki I. and Paul T., Modeling and simulation of grinding processes, , *CIRP Annals*, 41(2)(1992) 677-688.
20. McGeough J.A. and Rasmussen. H., A macroscopic model of electro-discharge machining, (1982) 333-339.
21. Ehmann K.F., Kapoor S.G., DeVor R.E. and Lazoglu I., Machining processes modeling: A review, *Trans. ASME, Journal of Manufacturing Science and Engineering*, 119(1997) 655-663.
22. Liao T.W. and Chen L.J., A neural network approach for grinding process: Modeling and optimization, *Int. J. Mach. Tools Manufact.*, 34(7)(1994) 919-937.
23. Grodzinskii E.Ya., Grinding with electrical activation of the wheel surface, *Mach. Tooling*, 50(12) (1979) 10-13.
24. Vitlin V.B., Model of the electro-contact-abrasive cutting process, *Sov. Eng. Res.* 1 (5) (1981) 88-91.
25. Grodzinskii E.Ya. and Zubotaya L.S., Electrochemical and electrical discharge abrasive machining, *Sov. Eng. Res.* 2 (3) (1982) 90-92.
26. Sakova R.B., Electrical discharge surface grinding: The process and the equipment, *Sov. Eng. Res.* 55 (8) (1984) 67-68.
27. Aoyama T. and Inasaki I., Hybrid machining- Combination of electrical discharge machining and grinding, *Proc. of the 14th North American Manufacturing research Conf.*, SME (1986), 654-661.

28. Rajurkar K.P., Wei B., Kozak J. and Nooka S.R., Abrasive electro-discharge grinding of advanced materials," *Proc. of the 11th International Symposium of Electro-machining (ISEM-11)* (1995) 863-869.
29. Koshy P. Jain V.K. and Lal G.K., Mechanism of material removal in electrical discharge diamond grinding," *Int. J. Mach. Tools Manufact.*, 36[10] (1996) 1173-1185.
30. Koshy P. Jain V.K. and Lal G.K., Grinding of cemented carbide with electrical spark assistance, *J. of Materials Processing Technology*, 72(1997) 61-68.
31. Choudhary S.K., Jain V.K. and Gupta M., Electrical discharge diamond grinding of high-speed steel, *Machining Science and Technology*, 3(1) (1999) 91-105.
32. Snoeys R. Maris M. and Peters J., Thermally induced damage in grinding, *CIRP Annals*, 2(2)(1978) 571-581.
33. Malkin S., Grinding of Metals: Theory and Application, *J. of Applied Metal Working*, 3(2) (1984) 95-109.
34. Zhang L., Suto T., Noguchi H. and Waida T., An overview of applied mechanics in grinding, *Manufacturing Review*, 5(4)(1992) 261-273.
35. Jaeger J.C., Moving sources of heat and temperature at sliding contact, *Proc. Roy. Soc. New South Wales*, 76 (1942) 203-224.
36. Outwater J.O., and Shaw M.C., Surface temperature in grinding, *Trans. ASME, Journal of Engineering for Industry*, 74 (1952) 73-86.
37. Hahn R.S., The relation between grinding conditions and thermal damage in the workpiece, *Trans., ASME, Journal of Engineering for Industry*, 78 (1956) 807-812.
38. DesRuisseaux N.R. and Zerkle R.D., Temperature in semi-infinite and cylindrical bodies subjected to moving heat sources and surface cooling, *Trans. ASME, Journal of heat transfer*, 92 (1970) 456-464.
39. DesRuisseaux N.R., and Zerkle R.D., Thermal analysis of the grinding process, *Trans., ASME, Journal of Engineering for Industry*, 92 (1970) 428-434.
40. Malkin S., Thermal aspects of grinding Part2: Surface temperature and workpiece burn, *Trans., ASME, Journal of Engineering for Industry*, 96 (1974) 1184-1191.
41. Peters J. and Vansevenant E., Thermal model covering pendulum grinding and creep feed grinding, *CIRP Annals*, 32(1)(1983) 491-494.

42. Kopalinsky E.M., A new approach to calculating the workpiece temperature distributions in grinding, *Wear*, 94(1984) 295-322.
43. Lavine A.S., A simple model for convective cooling during the grinding process, *Trans., ASME, Journal of Engineering for Industry*, 110(1988) 1-6.
44. Lavine A.S., and Jen T.C., Thermal aspects of grinding heat transfer to workpiece, wheel, and fluid, *Trans., ASME, Journal of Heat Transfer*, 113 (1991) 296-303.
45. Guo C., and Malkin S., Theoretical and experimental investigation of burn-out in creep-feed grinding, *CIRP Annals*, 34(1)(1994) 283.
46. Zheng H.W. and Gao H., A general thermal model for grinding with slotted or segmented wheel, *CIRP Annals*, 43(1)(1994) 287-290.
47. Jen T.C., and Lavine A.S., A variable heat flux model of heat transfer in grinding: Model development, *Trans., ASME, Journal of Heat Transfer*, 117 (1995) 473-478.
48. Zhang L., and Mahdi M., Applied mechanics in grinding-IV. The mechanism of grinding induced phase transformation, *Int. J. Mach. Tools Manufact.* 35, 10 (1995) 1397-1409.
49. Guo C., and Malkin S., Analysis of Transient Temperatures in Grinding, *Trans. ASME, Journal of Engineering for Industry*, 117(1995) 571-577.
50. Zhang Y. and Faghri A., An integral approximate solution of heat transfer in the grinding process, *Int. J. Heat Mass Transfer*, 39(13) (1996) 2653-2662.
51. Biermann D., and Schneider M., Modeling and simulation of work-piece temperature in grinding by finite element method, *Machining Science and Technology*, 1(2) (1997) 173-183.
52. Demetriou M.D. and Lavine A.S., Thermal aspect of grinding: The case of upgrinding, *Trans., ASME, Journal of Manufacturing Science and Engineering*, 122(2000) 605-611.
53. Eshghy S., Thermal aspects of the abrasive cut-off operation. Part 1-Theoretical analysis, *Trans., ASME, Journal of Engineering for Industry*, (1967) 356-360.
54. Korolev V.V., Temperature distribution calculations during abrasive machining, *Machines and Tooling*, 42(2)(1971) 47-50.
55. Snoeys R. and Van Dyck F., Investigations of EDM operations by means of thermo-mathematical models, *CIRP Annals*, 20(1)(1994) 35.

56. Van Dijck F.S. and Dutre W.L., Heat conduction model for the calculation of the volume of molten metal in electric discharges, *Appl. Phys.*, 7(1974) 499-910.
57. Toren M., Zvirin Y. and Winograd Y., Melting and evaporation phenomena during electrical erosion, *Trans., ASME, Journal of heat transfer*, (1967) 576-581.
58. Marty C.C., Investigation of surface temperature in electro-discharge machining, *Trans., ASME, Journal of Engineering for Industry*, (1977) 682-684.
59. Erden A. and Kaftanoglu B., Heat transfer modeling of electric discharge machining, *Proc. 21st MTDR Conference, Swansea*, (1980) 351-358.
60. Erden A. and Kaftanoglu B., Thermo-mathematical modelling and optimization of energy pulse forms in electric discharge machining (EDM), *Int. J. Mach. Tool Des. Res.*, 21(1) (1981) 11-22.
61. Dharmadhikari S.W. and Sharma C.S., Determination of material removal in EDM using a multiple heat source model, *Proc. 9th AIMTDR Conference, IIT Kanpur*, (1980) 316-320.
62. Jilani S.T. and Pandey P.C., Analysis and modelling of EDM parameters, *Precision Engineering*, 4 (4) (1982) 215-221.
63. Pandey P.C. and Jilani S.T., Plasma channel growth and the resolidified layer in EDM, *Precision Engineering*, 8 (2) (1986) 104-110.
64. Pandit S.M. and Rajurkar K.P., A stochastic approach to thermal modeling applied to electro-discharge machining, *Trans., ASME, Journal of Heat Transfer*, 105(1983) 555-562.
65. DiBitonto D.D., Eubank P.T., Patel M.R. and Barrufet A., Theoretical models of the electrical discharge machining process-I: A simple cathode erosion model, *J. of Applied Physics*, 66(9)(1989) 4095-4103.
66. Patel M.R., Barrufet M.A., Eubank P.T. and DiBitonto D.D., Theoretical models of the electrical discharge machining process-II: The anode erosion model, *J. of Applied Physics*, 66(9)(1989) 4104-4111.
67. Eubank P.T., Patel M.R., Barrufet M.A. and Bozkurt B., Theoretical models of the electrical discharge machining process-III: The variable mass, cylindrical plasma model, *J. of Applied Physics*, 73(11)(1993) 7900-7909.

68. Madhu P., Jain V.K., Sundarajan T. and Rajurkar K.P., Finite element analysis of EDM process, *Processing of Advanced Materials*, 1(1991) 161-173.
69. Bhattacharya R., Jain V.K. and Ghoshdastidar P.S., Numerical simulation of thermal erosion in EDM Process, *IE (I), Journal-PR*, 77(1996) 13-19.
70. Shankar P., *Analysis of Spark Discharge in EDM Process*, M.Tech. Thesis, Indian Institute of Technology, Kanpur (1993).
71. Shaw M.C., *Principles of Abrasive Processing*, Clarendon Press, Oxford (1996)
72. Malkin S., *Grinding Technology: Theory and Applications of Machining with Abrasives*, Ellis Howard Limited, Chichester and John Wiley & Sons, New York (1989)
73. Reddy J.N., *An Introduction to the Finite Element Method*, 2nd Edition, McGraw-Hill, Inc., New Delhi(1993)
74. Erden A., Effect of Materials on the Mechanism of Electric Discharge Machining (EDM), *Trans. ASME, Journal of Engineering Materials and Technology*, 108(1983) 247-251.
75. Snoyes R. and Van Dijck F., Plasma Channel Diameter Growth Affects Stock Removal, *CIRP Annals*, 21(1) (1972) 39-40.
76. Boley B.A. and Weiner J.H. *Theory of thermal stresses*, John Wiley and Sons, New York (1960).
77. Machinability data centre, *Machining data handbook*, 3rd Ed., volume two, Cincinnati, Ohio (1980)
78. Mishra A. and Prasad T., Residual stresses due to a moving heat source, *International Journal of Mechanical Science*, 27(9) (1985) 571-581.
79. Vancevenant E., An improved mathematical model to predict residual stresses in surface plunge grinding, *Annals of CIRP*, 36(1) (1987) 413-416.
80. Li Y.Y., and Chen Y., Simulation of surface grinding, *ASME Journal of Engineering Materials and Technology*, 111 (1989) 46-53.
81. Mahdi M. and Zhang L., Applied mechanics in grinding-V. Thermal residual stresses, *Int. J. Mach. Tools Manufact*, 37(5) (1997) 619-633.

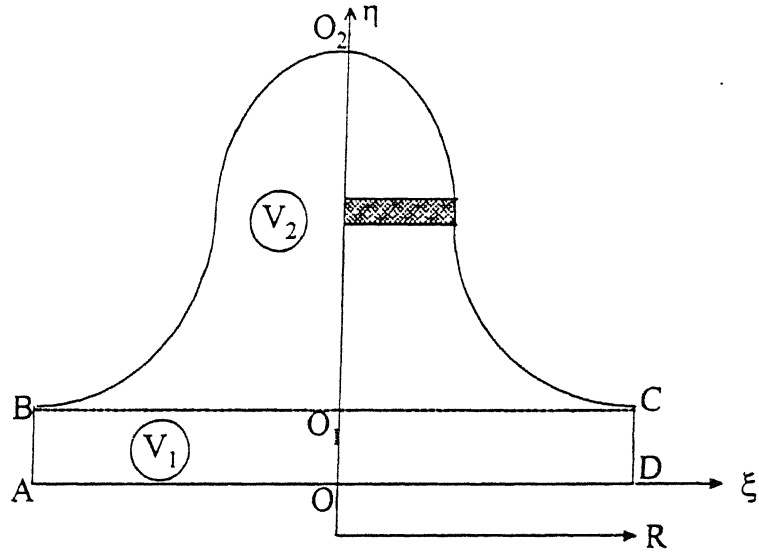
82. Mahdi M. and Zhang L., Applied mechanics in grinding-VI. Residual stresses and surface hardening by coupled thermo-plasticity and phase transformation, *Int. J. Mach. Tools Manufact.*, 38 (1998) 1289-1304.
83. Chen X., Rowe W.B., and McCormack D.F., Analysis of the transitional temperature for tensile residual stress in grinding, *Journal of materials processing technology*, 107 (2000) 216-221.
84. Kruth J. P., Stevens L., Frogen L., and Laywers B., Study of the white layer of a surface machined by die-sinking electro-discharge machining, *Annals of CIRP* 44(1) (1995) 169-172.
85. Field M. and Khales J. F., Review of surface integrity of machined component, *Annals of CIRP* 25(2) (1976) 569-573.
86. Roethel F., Kosec L. and Garbajs V., Contribution to the microanalysis of the spark eroded surfaces, *Annals of CIRP* 25(1975) 135-140.
87. Lee L. C., Lim L. C., Narayanan V. and Venkatesh V-V., Quantification of surface damage of tool steels after EDM, *Int. J. Mach. Tools Manufact.* 28(4) (1988) 359-372.
88. Rajurkar K.P., and Pandit S.M., Quantification expressions for some aspects of surface integrity of electro-discharge machined components, *Trans. ASME, Journal of Engineering for Industry*, 106(1984) 171-177.
89. Metzger J.L., *Superabrasive grinding*, Butterworth, London (1986).
90. Koshy P., Jain V.K., and Lal G.K., A model for the topography of diamond grinding wheels, *Wear*, 169 (1993) 237-242.
91. Ueda T., Hosokawa A., and Yamamoto A., Measurement of Grinding Temperature Using Infrared Radiation Pyrometer with Optical Fibre, *ASME Journal of Engineering for Industry*, 108 (1986) 247-251.
92. Beck J.V., Thermocouple Temperature Disturbances in Low Conductivity Materials, *ASME Journal of Heat Transfer*, 84(1962) 124-132.
93. Kato T., and Fujii H., Temperature Measurement of Workpiece in Surface Grinding by PVD Film Method, *ASME Journal of Manufacturing Science and Engineering*, 119 (1997) 689-694.

94. Zhang L.C., Suto T., Noguchi H., and Waida T., Applied Mechanics in Grinding Part III: A New Formula for Contact Length Prediction and a Comparison of Available Models, *Int. J. Mach. Tools Manufact.*, 33 (1993) 2, 87-597.
95. Gu D.Y. and Wager J.G., New Evidence on Contact Zone in Grinding, *CIRP Annals*, 37(1) (1988) 335.
96. Salje E. and Mohlen H., Fundamental Dependencies upon Contact Length and Results in Grinding, *CIRP Annals*, 35(1) (1986) 249-253.
97. Konig W. and Steffens A., Numerical Method to describe the kinematics of grinding, *CIRP Annals*, 31(1) (1982) 201-204.
98. Zhang L.C., Suto T., Noguchi H., and Waida, T., Applied Mechanics in Grinding Part II: modeling of elastic modulus of wheels and interface forces, *Int. J. Mach. Tools Manufact.*, 33(2) (1993) 245-255.
99. Rowe W.B., Black S.C.E., Mills B., Qi H.S., and Morgan M.N., Experimental Investigation of Heat Transfer in Grinding, *CIRP Annals*, 44(1) (1995) 329. -332.
100. Ramanath S. and Shaw M.C., Abrasive Grain Temperature at the Beginning of a Cut in Fine Grinding, *ASME Journal of Engineering for Industry*, 110 (1988) 15-18.
101. Shaw M.C., A Simplified Approach to Workpiece Temperature in Fine Grinding, *CIRP Annals*, 39(1) (1990) 345-347.
102. Rowe W.B., Pettite J.A., Boyle A., and Moruzzi J.L., Avoidance of Thermal Damage in Grinding and Predictions of the Damage Threshold, *CIRP Annals*, 37(1) (1988) 327-330.
103. Rowe W.B., Morgan M.N., and Allanson D.A., An Advance in the Modeling of Thermal Effects in the Grinding Process, *CIRP Annals*, 40(1) (1991) 339-342.
104. Rowe G.W., Morgan M.N., Black S.C.E and Mills B., A simplified approach to control of thermal damage in grinding, *CIRP*, vol. 45, No. 1, (1996) 299-302.
105. Rowe W.B., Analysis of grinding temperatures by energy partitioning. *Proc. Instn Mech Engrs*, Vol. 210, (1996) 579-588.
106. Kohli S., Guo C., and Malkin S., Energy Partition to the Workpiece for Grinding with Aluminum Oxide and CBN Abrasive Wheels, *ASME Journal of Engineering for Industry*, 117 (1995) 160-168.

107. Guo C., and Malkin S., Analysis of Energy Partition in Grinding, ASME Journal of Engineering for Industry, 117 (1995) 55-61.
108. Guo C., Wu Y., Varghese V., and Malkin S., Temperatures and Energy Partition for Grinding with Vitrified CBN Wheels, CIRP Annals, 48 (1) (1999) 247-250.
109. Varghese V., Guo C., Malkin S., and Xiao G., Energy Partition for grinding of Nodular Cast Iron with Vitrified CBN wheels, Machining Science and Technology, 4(2) (2000) 197-208.
110. Kato T., and Fujii H., Energy Partition in Conventional Surface Grinding, ASME Journal of Manufacturing Science and Engineering, 121(1999) 393-398.
111. Ju Y., Farris T.N., and Chandrasekar S., Theoretical Analysis of Heat Partition and Temperatures in Grinding," ASME Journal of Tribology, 120(1998) 789-794.
112. Smithells C.J., *Metals reference book*, Butterworth, 6th Edition, 1983.

Appendix A

Derivation for heat flux due to Gaussian distributed spark heat source



Considering the effect of spark upto 6- σ limit i.e.

$$6\sigma = 2R \quad \text{or} \quad \sigma = R/3$$

The heat flux $q_{ws}(r)$ at a radius (r) can be calculated if maximum intensity q_o at the axis of a spark and its radius (R) is known.

$$q_{ws}(r) = q_o \exp \left\{ -4.5 \left(\frac{r}{R} \right)^2 \right\} \quad \text{A1.1}$$

At $\xi=0$, $\eta=q_o$ and at $\xi=R$, $\eta=q_o e^{-4.5}$

Now from equation A1.1

$$\ln \frac{\eta}{q_o} = -4.5 \frac{\xi^2}{R^2} \quad \text{or} \quad \xi^2 = -\frac{R^2}{4.5} \ln \frac{\eta}{q_o} \quad \text{A1.2}$$

If it is assumed that total power of each pulse is to be used only by one spark then

Total volume of the of the spark is given by:

$$V = f_w U_b I = V_1 + V_2 \quad A1.3$$

Where

$$\text{Volume after rotating } O O_1 C D \text{ about } O O_2 (V_1) = \pi R^2 q_o e^{-4.5} = 0.011\pi R^2 q_o \quad A1.4$$

$$\begin{aligned} \text{Volume after rotating } O_1 O_2 C \text{ about } O_1 O_2 (V_2) &= \pi \int_{q_o e^{-4.5}}^{q_o} \xi^2 d\eta \\ &= \pi \int_{q_o e^{-4.5}}^{q_o} \left(-\frac{R^2}{4.5} \ln \frac{\eta}{q_o} \right) d\eta \\ &= 0.2086\pi R^2 q_o \end{aligned} \quad A1.5$$

Putting A1.4 and A1.5 in A1.3

$$f_w U_b I = 0.011\pi R^2 q_o + 0.2086\pi R^2 q_o \quad A1.6$$

OR

$$q_o = \frac{4.45 R_{ws} U_b I}{\pi R^2} \quad A1.7$$

Putting the value of q_o from equation A1.7 into equation A1.1

$$q_{ws}(r) = \frac{4.45 R_{ws} U_b I}{\pi R^2} \exp \left\{ -4.5 \left(\frac{r}{R} \right)^2 \right\} \quad A1.8$$

Where U_b is breakdown (discharge) voltage and I is current

Publications from the Present Work

- Yadava V. and Jain V.K., Abrasive Electro Discharge Grinding, *Proceedings of the 18th All India Manufacturing Technology Design and Research Conference*, I.I.T. Kharagpur, (1998) 357-362.
- Yadava V., Jain V.K., and Dixit P.M., Temperature distribution during electro-discharge abrasive grinding, *Machining Science and Technology*, 6(1) (2002) 97-127.
- Yadava V., Jain V.K., and Dixit P.M., Thermal Stresses due to Electrical Discharge Machining (EDM), *Int. J. Mach. Tools Manufact.*, 42 (8) (2002) 877-888.
- Yadava V., Jain V.K., and Dixit P.M., Thermal Stresses in Electro-Discharge Diamond Grinding, *Machining Science and Technology* (communicated).
- Yadava V., Jain V.K., and Dixit P.M., Thermal Analysis of Electro-Discharge Abrasive Surface Grinding, *Journal of Materials Processing Technology* (communicated).
- Yadava V., Jain V.K., and Dixit P.M., Parametric study of temperature distribution in electro-discharge diamond grinding, *Int. J. Mach. Tools Manufact.* (to be published).